Università degli Studi di Torino
Scuola di Dottorato in Scienza ed Alta Tecnologia

Large-scale environment of low luminosity radio loud AGNs

Nuria Álvarez Crespo

Università degli Studi di Torino
Scuola di Dottorato in Scienza ed Alta Tecnologia

Dipartimento di Fisica, Via Pietro Giuria 1, Torino,

Large-scale environment of low luminosity radio loud AGNs

Nuria Álvarez Crespo

Tutor: Francesco Massaro

Siempre le pedía a mi padre que me comprara un pájaro y él siempre me decía que lo que en realidad deseaba era la jaula. - El pájaro es la excusa - añadía.

Juan José Millás

Acknowledgements

To my supervisor Prof. Massaro for guiding me and for giving me many opportunities to travel and to learn. I would like to thank my thesis committee: Dr. Paolillo, Dr. Risaliti and Dr. Mignone for their insightful comments and questions. I am also grateful to the University of Turin for funding the PhD research and giving me the opportunity to perform my research. To the great people that I met in Boston and to that conversations in the coffee room. To all the new friends made during this experience and in particular to my fellow doctoral students, for all the conversations, coffee and travels together. To the old ones for caring and never forgetting about me, even in the distance. To my family, my sister Inés, my parents Ramón and María Elena and my grandfather Alberto for all their support and encouragement. To the love of my life Juan for making me happy every day. You gave me strength and courage in the difficult times, and fun and joy in the easy ones.

Abstract

Context: Active Galactic Nuclei (AGNs) are astrophysical sources located at the center of some galaxies, powered by accretion of matter into a supermassive black hole. About 10 % of these sources show jets, i.e., highly collimated outflows of ultrarelativistic particles that appear to originate at the central source, that extend for tens up to hundreds of kiloparsecs from the regions surrounding the black holes at their centres. The radio loud AGN Unification Model associates intrinsic low-luminosity radio galaxies (Fanaroff Riley type I, FR Is) with BL Lacs, being the former class the misaligned parent population of the latter since BL Lacs are considered to be FR Is but seen through their jets. BL Lacs are very strong γ-ray emitters, being the most numerous extragalactic sources at such high energies.
Aims: According to the Unification Model, FR Is and BL Lacs must reside in similar environments. An extensive study of the FR Is large-scale environments has been performed by several authors throughout the years, and it is widely accepted that these objects tend to lie in galaxy groups or in moderately rich clusters. However, such systematic study of the clustering of galaxies around BL Lacs has not been performed yet, since only a handful of studies were devoted to this subject and to only a few objects, sometimes showing contradictory results. Here I present a compartive study of the environment of FR Is and BL Lacs. In addition, to improve statistics in the BL Lac study, it is important to find methods to discover new BL Lacs and measure their redshifts. Out of 3,033 sources in the latest release of the *Fermi* catalog $\sim$ 30% remain still unidentified, and since BL Lacs dominate the extragalactic γ-ray sky ($\sim$ 30% of the associated sources), many of the unassociated sources could be BL Lacs. Moreover, about a 28% of the sources associated with a low energy counterpart show multifrequency behaviour similar to that of BL Lacs, but lack of spectroscopic information to confirm their classification, these are called Blazars of Uncertain type.
Methods: The sample of FR Is was taken from a well defined sample in the FRICAT, while BL Lacs were selected from the Roma-BZCAT and sources classified as BL Lacs and BL Lacs with galactic spectra were studied separately. I selected those inside the footprint of the Sloan Digital Sky Survey (SDSS), and downloaded all the sources classified as galaxies inside a 2 Mpc radius from the FR I/BL Lac, and an analogous analysis was applied for both populations. A positional and redshift cross-match was performed with a catalog of galaxy clusters/groups in the SDSS, I measured the number of sources with a difference in their spectroscopic redshift from that of the central FR I/BL Lac $\Delta z < 0.005$ inside that radius, and called them *"cosmological neighbours"*. I also applied clustering algorithms to the photometric sources classified as galaxies in that 2 Mpc radius. Additionally, here I summarized results of the last 3 years of a spectroscopic campaign that started on 2012 to look for BL Lacs among Unidentified Gamma-ray Sources and Blazars of Uncertain Type in the latest release of the *Fermi* catalog.
Results: About 70% of the FR Is were found in groups/clusters of galaxies but only $\sim$ 12% of the BL Lacs were found inside that same environment, strongly suggesting that both populations lie in different large-scale environments. Besides, $\sim$ 30% of the so-called "BL Lacs of galactic type" were found in galaxy rich environments, so there is a difference between the environments of these classes. In the optical spectroscopic campaign, a number of 188 spectra were analyzed, combining observations using 6 different telescopes with new data from optical surveys and literature, leading to the discovery of 132 new BL Lacs, proving the high efficiency of our selection strategy.
Conclusions: Contrarily to what stated by the Unification Model, FR Is and BL Lacs reside in different environments, since most FR Is were found in groups/clusters of galaxies while BL Lacs do not tend to lie in galaxy rich large-scale environments. However, BL Lacs showing galactic spectrum lie in richer environments than BL Lacs but still not as rich as FR Is. Finally, about 70% of the sources observed during the last three years of our optical spectroscopic campaign were BL Lacs.

Contents

List of Figures

List of Tables

Acronyms

1FGL ..... First Fermi γ-ray LAT point source catalog

2dFGRS ..... Two-degree Field Galaxy Redshift Survey

2FGL ..... Second Fermi γ-ray LAT point source catalog

3C ..... Third Cambridge Catalogue

3CR ..... Revised Third Cambridge Catalogue

3FGL ..... Third Fermi γ-ray LAT point source catalog

6dFGS ..... Six-degree-Field Galaxy Survey

ACS ..... Advanced Camera for Surveys

AGN ..... Active Galactic Nuclei

AGU ..... Active Galaxy of Uncertain type

BCG ..... Brightest Cluster Galaxy

BCU ..... Blazar Candidate of Uncertain type

BLR ..... Broad Line Region

BLRG ..... Broad Line Radio Galaxy

BZB ..... BL Lac, nomenclature from the BZCAT

BZG ..... BL Lac of Galactic type, nomenclature from the 5th edition of the BZCAT

BZQ ..... Flat Spectrum Radio Quasar, nomenclature from the BZCAT

BZU ..... Blazar of Uncertain type, nomenclature from the BZCAT

CCD ..... Charge Coupled Device

DBSCAN ..... Density Based Spatial Clustering of Applications with Noise

DR ..... Data Release

EC ..... External Compton

ECGMM ..... Error Corrected Gaussian Mixture Model

ETG ..... Early Type Galaxy

EW ..... Equivalent Width

FIRST ..... Faint Images of the Radio Sky at Twenty-cm

FoF ..... Friends-of-friends algorithm

FRI ..... Fanaroff-Riley type I radio galaxy

FRII ..... Fanaroff-Riley type II radio galaxy

FSRQ ..... Flat Spectrum Radio Quasar

FWHM ..... Full Width at Half Maximum

GB6 ..... Green Bank 6-cm Radio Source Catalog

GMBCG ..... Gaussian Mixture Brightest Cluster Galaxy

HBL ..... High-energy peaked BL Lac

HERG ..... High-Excitation Galaxy

HST ..... Hubble Space Telescope

IBL ..... Intermediate-energy peaked BL Lac

IRAF ..... Image Reduction and Analysis Facility

IC ..... Inverse Compton

ICM ..... Intra-Cluster Medium

IGM ..... Intergalactic Medium

IR ..... Infrared

KDE ..... Kernel Density Estimator

KPNO ..... Kitt Peak National Observatory

KS ..... Kolmogorov-Smirnov

LAT ..... Large Area Telescope

LBL ..... Low-energy peaked BL Lac

LERG ..... Low-Excitation Galaxy

LINER ..... Low-Ionization Nuclear Emission-line Region

LIRG ..... Luminous IR Galaxy

LTE ..... Local Thermodynamical Equilibrium

MST ..... Minimum Spanning Tree

NAT ..... Narrow Angle Tail radio galaxy

NOT ..... Nordic Optical Telescope

NLR ..... Narrow Line Region

NLRG ..... Narrow Line Radio Galaxy

NVSS ..... National Radio Astronomy Observatory Very Large Array Sky Survey

OAN ..... Observatorio Astronómico Nacional

OPTICS ..... Ordering Points To Identify the Clustering Structure

OVV ..... Optically Violently Variable

pc ..... Parsec

PMN ..... Parkes-MIT-NRAO Surveys

PSF ..... Point Spread Function

QSO/QSR ..... Quasar

RBL ..... Radio selected BL Lac

RG ..... Radio Galaxy

Roma-BZCAT Roma-multifrequency blazar catalog

SED ..... Spectral Energy Distribution

SDSS ..... Sloan Digital Sky Survey

SMBH ..... Supermassive Black Hole

S/N ..... Signal to Noise ratio

SOAR ..... Southern Astrophysical Research Telescope

SUMSS ..... Sydney University Molonglo Sky Survey Source Catalog

SZ ..... Sunyaev-Zel'dovich

TNG ..... Telescopio Nazionale Galileo

UGS ..... Unassociated Gamma-ray Sources

ULIRG ..... Ultraluminous IR galaxy

UV ..... Ultraviolet

VLA ..... Very Large Array

VLBI ..... Very Long Baseline Interferometry

WAT ..... Wide Angle Tail radio galaxy

WBS ..... Wise Blazar Strip

WHT ..... William Herschel Telescope

WIBRaLS ..... Wise Blazar-Like Radio Loud Sources catalog

WISE ..... Wide-field Infrared Survey Explorer

XBL ..... X-ray selected BL Lac

CHAPTER 1

Radio loud active galaxies

1.1 Active Galactic Nuclei

An Active Galactic Nucleus (AGN) is a bright, compact region at the center of an active galaxy. Such an excess is observed at all wavelengths (L_{bol} up to 10^{48} erg s^{-1}) and the electromagnetic spectrum of an AGN has features indicating that the emission is not produced by stars or by gas. An AGN can vary in luminosity on short timescales (hours or days), which means that the emitting source must be very compact in size. The current interpretation of the AGN emission is the result of accretion of matter on a supermassive black hole (SMBH), with masses between 10^6 and 10^9 M$_\odot$ at the center of its host galaxy. The accretion occurs via a disk that loses angular momentum due to viscosity and turbulent processes, emitting strong radiation in the ultraviolet (UV) and in the soft X-rays and extending up to distances of 10^{-2}, 10^{-3} pc (Krolik, 2000). In addition, a corona of hot electrons forms above the accretion disc scatters photons up to hard X-rays. Further away from the disk, in the so-called "Broad Line Region" (BLR) about 0.1 - 1 pc from the SMBH, there are clouds of gas orbiting very fast, of the order of 10^3 km s^{-1} and producing strong and broad optical and UV emission lines. Continuing outwards, at $\sim 10^2$ - 10^3 pc, a molecular torus of colder gas and dust exists. It is optically thick and if viewed edge on it blocks the radiation from the accretion disc and from the BLR. Beyond the torus, there are clouds of gas but moving at speeds of the order of 100 km s^{-1}, producing narrow optical emission lines in the so-called "Narrow Line Region" (NLR). Some AGNs may have also pairs of jets, fast and highly collimated outflows of ultrarelativistic particles that emerge from the poles of the AGN. An schematic representation of an AGN is shown in Fig. 1.1.

The observed characteristics of an AGN depend on several properties such as the mass of the central black hole, the rate of gas accretion onto the black hole, the orientation of the accretion disk with respect to the observer, the degree of obscuration of the nucleus by dust and the presence or absence of jets. The so-called Unification Model accounts for the different observed features observed in AGNs in terms of their orientation.

AGNs can be classified in two families, whether they show a jet or not (Urry & Padovani, 1995):

1. **Radio Loud:** Roughly between 15% and 20% of AGNs have jets and are radio loud, meaning

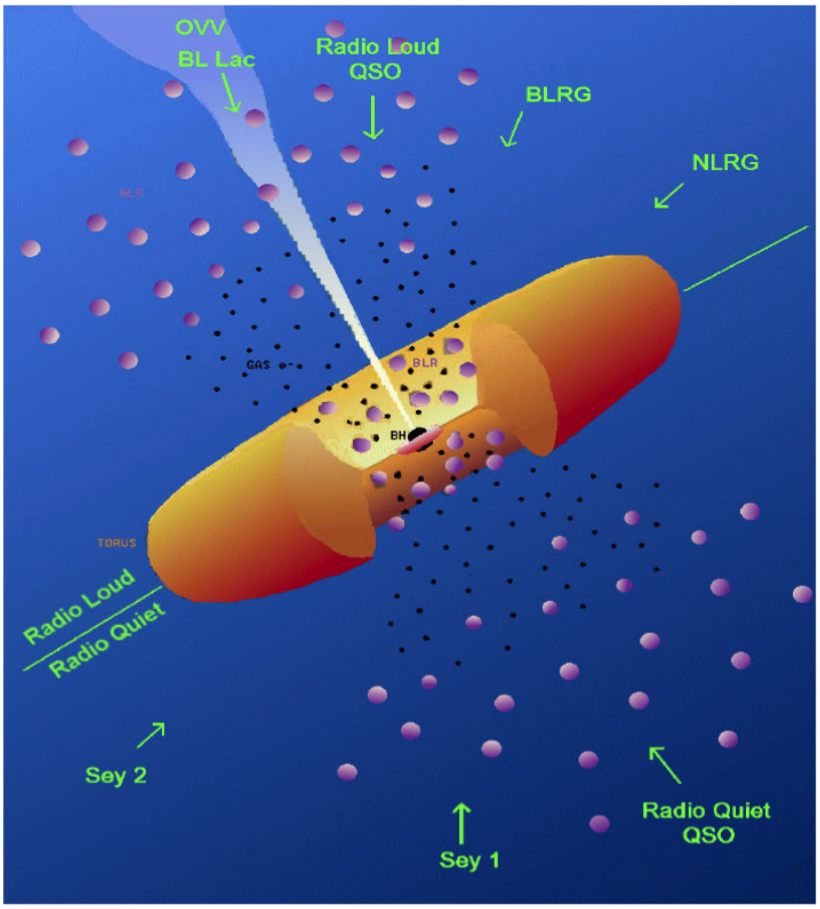

Figure 1.1: AGN paradigm: a SMBH provides the central power source, surrounded by an accretion disk ($\sim 10^{-3}$ - 10^{-2} pc) funnelling matter onto it. The BLR clouds at ~ 0.1 - 1 pc are pictured before the obscuring dusty torus ($\sim 10^{2}$ - 10^{3} pc). Farther out from the torus there is the NLR clouds, at ~ 10 - 100 pc. In the top part of the image a radio loud AGN is depicted by the representation of a relativistic jet, while the lower half represents a radio-quiet AGN without a jet (Urry & Padovani, 1995).

their ratio of radio (5 GHz) to optical (B-band) flux is $F_5/F_B \geq 10$ (Kellermann et al., 1989). Depending on their orientation they can be separated into 3 classes:

- **Type 1: Broad Line Radio Galaxies (BLRGs).** They are seen from an angle for which the BLR is visible, so they are characterized by a bright continuum and broad emission lines in their optical spectra, featuring H and He lines with velocities up to 25,000 km s^{-1}. Some include narrow emission features as well.
- **Type 2: Narrow Line Radio Galaxies (NLRGs).** The emission from the central region is absorbed by the dusty torus, so these sources feature a weak continua and weak emission lines in their optical spectra, coming from the NLR with velocities of the order of 100 km s^{-1}. These lines are forbidden transitions of O, N, S, and Fe, as well as the Balmer lines of H.
- **Type 0: Blazars.** Rare sources since their relativistic jets are seen from a small angle with respect to the line of sight ($\lesssim$ 15 - 20 deg). Their emission is therefore dominated by the radiation coming from relativistic particles accelerated in its jet.

2. **Radio Quiet:** A large fraction of AGNs do not show jets or when they do these are thousands of times weaker relatively than the rest of the AGN emission. These sources are not detected (or very weak) on the radio band. In this case, the number of morphological subclassifications is broader than for the radio loud objects:

   - **Type 1:**

     Seyfert 1 galaxies. The optical emission is the same as for the radio loud counterpart, while their nuclear luminosity is weaker, therefore their host galaxy can often be resolved.

     QSOs. Higher luminosity radio-quiet quasars, they are typically observed at greater distances than Seyfert 1s, and their nuclear emission usually dominates the host galaxy.

   - **Type 2: Seyfert 2 galaxies.** They share the same optical properties of their radio loud homologous with weak continua and narrow emission lines.
   - **LINERS.** These systems show in their spectra line emission from weakly ionized or neutral atoms, such as O, O^+, N^+ and S^+.

1.2 Radio galaxies

Radio galaxies (RGs) are very luminous objects, with total radio luminosities ranging from 10^{41} up to 10^{46} erg s^{-1}. They are very energetic sources over the entire electromagnetic spectrum and the observed structure in the radio band is determined by the interaction between twin jets and the external medium.

RGs display a wide range of structures in radio maps at different frequencies. The most common large-scale structures are called lobes: these are double roughly ellipsoidal formations placed on either side of the active nucleus. A significant number of low-luminosity sources exhibit structures usually known as plumes, which are much more elongated and not confined. Long thin jets extend away from the compact central core toward the outer radio lobes, in form of a collimated flow of relativistic accelerated particles. Often the jets end up at very bright and compact structures at the termination of the jet flow called hot spots. Generally, hot spots and jets appear to have flatter spectra than the more extended diffuse components, apparently reflecting their younger ages and correspondingly lower synchrotron radiation losses.

1.2.1 Discovery and historical overview

After the discovery that the radio source Cygnus A was associated with a faint distant galaxy (Baade & Minkowski, 1954), radio astronomy became very important for observational cosmology. Other radio sources were identified with galaxies during the 50's, with measured redshifts up to $z \sim 0.45$ (Minkowski, 1960). However, progress was slow in this field due to the poor accuracy of the radio source positions. The Third Cambridge Catalogue (3C, Edge et al., 1959) was a radio survey that led to further progress in the discovery of new radio sources, as well as identifying the visible counterparts associated with the radio emission. Later on, Hy Spinrad devoted a considerable amount of his time to measuring the redshifts of faint RGs up to $z \sim 0.1$ using long photographic exposures with the James Lick Telescope (Spinrad, 1976; Spinrad et al., 1977). The fact that radio sources interact with their optical hosts was still unknown, and RGs were not believed to play an important role in the general scheme of galaxy evolution. However, a revolution in the field of the optical astronomy happened during the end of the 80's and beginning of the 90's with the replacement of photographic

techniques by charged-coupled devices (CCDs). This new technology led to the surprising discovery that radio sources and optical host galaxies are aligned so there must be considerable interaction between the radio sources and their host galaxies (see e.g. Roettgering et al., 1995; McCarthy et al., 1996). At that time it grew popularity the idea that the viewing angle of sight could play a role in determining observed properties that could explained the different observed types of active galaxies.

1.2.2 Observational properties and theoretical interpretation

Radio emission in RGs originates from the interaction of the jet magnetic fields and relativistic electrons, producing synchrotron radiation. These two jets of material extend outwards for tens to hundreds of kpc from the opposed regions surrounding the SMBH at the center of the RG. Jets have been seen to be relativistic on parsec scales (see e.g. Giovannini et al., 2001), however in low power RGs they slow down to sub-relativistic velocities over distances of $\sim$ 1 - 10 kpc (Laing et al., 1999). The radio-frequency spectra and polarization properties of RGs are characteristic of synchrotron radiation originating from relativistic electrons having a power law distribution. However, synchrotron radiation is not confined to radio wavelengths: if the jet and hotspots can accelerate particles to high enough energies, features that are detected in the radio wavelengths may also be detected in the IR, optical, UV and even X-rays.

Some of the RGs show bright optical emission/absorption lines, so it is relatively easy to determine their redshift. Broad lines are sometimes accompanied by an excess in the optical/UV called the Big Blue Bump that is usually interpreted as thermal radiation from an accretion disk.

1.2.3 Radio galaxy classification

Fanaroff & Riley (1974) distinguished RGs between two different morphological types (see Fig. 1.2), depending on the relative positions of regions of high and low surface brightness in the radio band. These authors divided their sample of 57 RGs from the 3CR catalogue using the ratio R_{FR}, that is the distance between the regions of highest surface brightness on opposite sides of the central galaxy or quasar, divided by the total extent of the source up to the lowest brightness contour in the map. Sources with $R_{FR} < 0.5$ were classified as Fanaroff-Riley type I (FR I) and sources with $R_{FR} > 0.5$ as Fanaroff-Riley type II (FR II).

- **FR I. Fanaroff-Riley tipe I:** They are characterized by lower radio luminosity than the other subtype, and show symmetric radio jets whose intensity falls away from the nucleus, $R_{RF} < 0.5$. The jets in FR Is may initially be launched relativistically but appear to decelerate on sub-kiloparsec scales, likely through interaction with the environment (Laing & Bridle, 2008). FR I host galaxies are generally brighter than FR IIs and they often show cD-like morphology (central dominant object of clusters, large ellipticals with a faint halo (Zirbel, 1996)). The emission from the jets is highly polarized with an average polarization over the jets $\sim$ 30%, and the projected magnetic field is perpendicular to the jet axis (Kharb et al., 2005). As the galaxy moves through the cluster, the gas can sweep back and distort the radio structure through ram pressure leading to many disturbed and atypical radio structures.

- **FR II. Fanaroff-Riley tipe II:** These sources show highly collimated jets leading to well-defined lobes with prominent hot spots and bright outer edges, $R_{RF} > 0.5$. Their emission is dominated by the large and diffuse radio lobes, and the smooth nature of their jets is thought to be indicative of highly supersonic flows. At the same radio luminosity, their optical emission lines are one order of magnitude stronger than those of FR Is, but FR IIs have higher radio

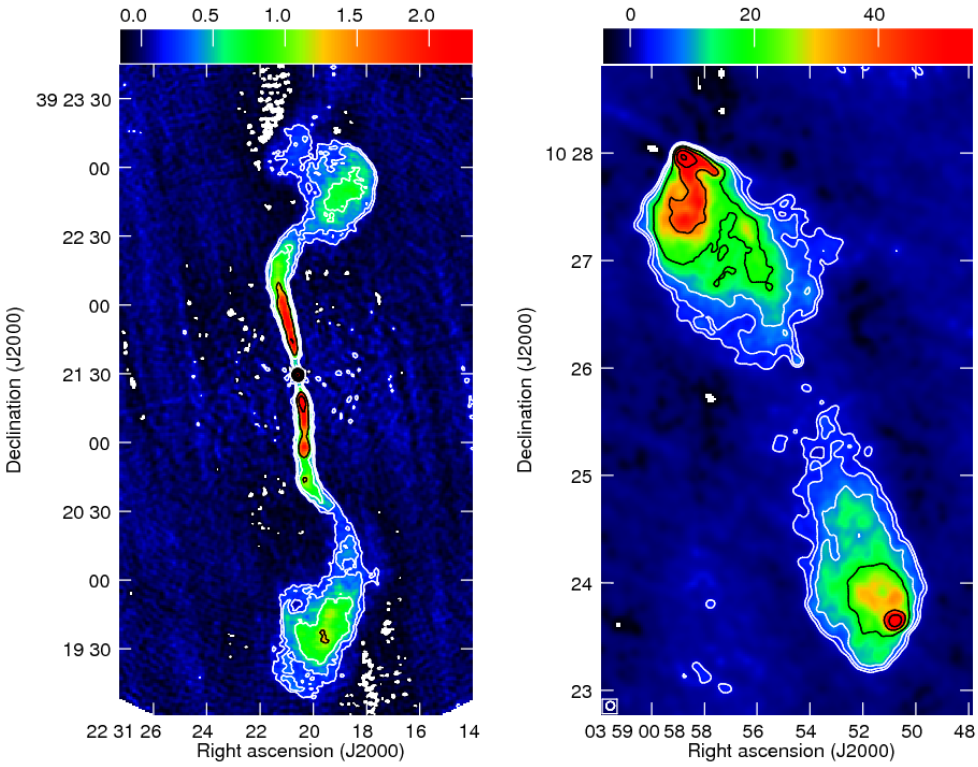

Figure 1.2: VLBI radio images showing two archetypical radiogalaxies. *Left:* FR I galaxy 3C 449. The brightest radio emission is close to the radio core, $R_{FR} < 0.5$. *Right:* FR II galaxy 3C 98. The brightest radio emission is at the termination points of the jets, in the hot spots, $R_{FR} > 0.5$.

powers on average than FR Is, with the division between the two types occurring at a radio power $L_{178MHz} \sim 2 \cdot 10^{25}$ W Hz^{-1}. Regarding their host galaxy, FR IIs are typically associated with N-galaxies (point-like nuclei and a steep brightness profile) or disturbed ellipticals, and avoid cD.

Both classes follow a separate linear $L_r - L_o$ correlation in the two-dimensional optical-radio luminosity plane, implying the FR I/FR II break depends on optical as well as radio luminosity, (see Fig. 1.3, Owen & Ledlow, 1994).

Recently the class FR0 was suggested by Baldi et al. (2015, 2018), they are RGs having similar low radio luminosity ($L_{1.4GHz} < 10^{32}$ erg s^{-1} Hz^{-1}), jet-dominated compact morphologies and [O III] line luminosities to those of FR Is, but lacking prominent extended radio emission, being a factor ~ 30 more core-dominated.

In addition it is possible to subclassify RGs according to their morphology, referring to the opening angle between the two opposite jets emanating from the nucleus of the optical galaxy (see Fig. 1.4). One of them is wide-angle tail (WAT) RGs. They form a class of RGs whose radio jets have been bent into a wide C shape, being the general interpretation of this bend that the jets are being swept back by ram pressure resulting from the high velocity motion of the associated active elliptical galaxy through its surrounding intra-cluster medium (ICM) (Begelman et al., 1979). The other class is named head-tail or narrow angle tail (NAT) RGs, in which all the radio emission lies in a tail on one side of the galaxy, and the galaxy itself forms the head of the tail. Their morphology

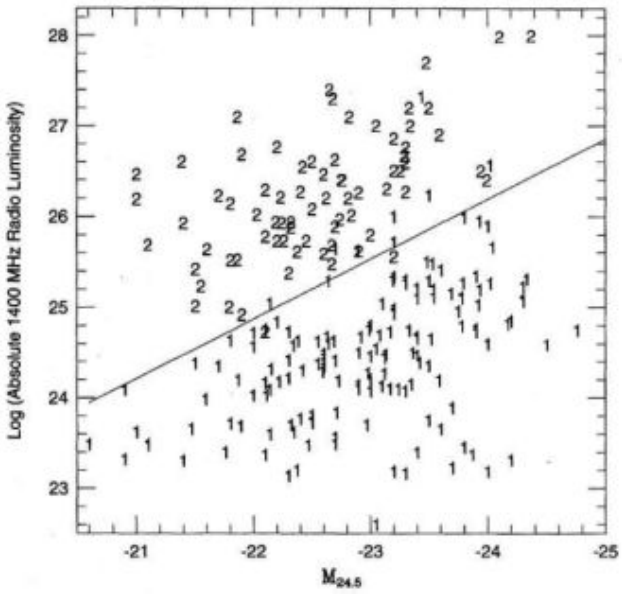

Figure 1.3: A plot of 1.4 GHz monochromatic luminosity against absolute R-band magnitude for a sample of powerful radio sources in galaxy clusters, with FR I and FR II class objects marked with the numbers 1 and 2 respectively (Ledlow & Owen, 1996).

suggest that these sources interact significantly with their external environment. The distinction between these two classes refers to the opening angle between the two opposite jets. However, it strongly depends on the angular resolution and on the distance to the RG.

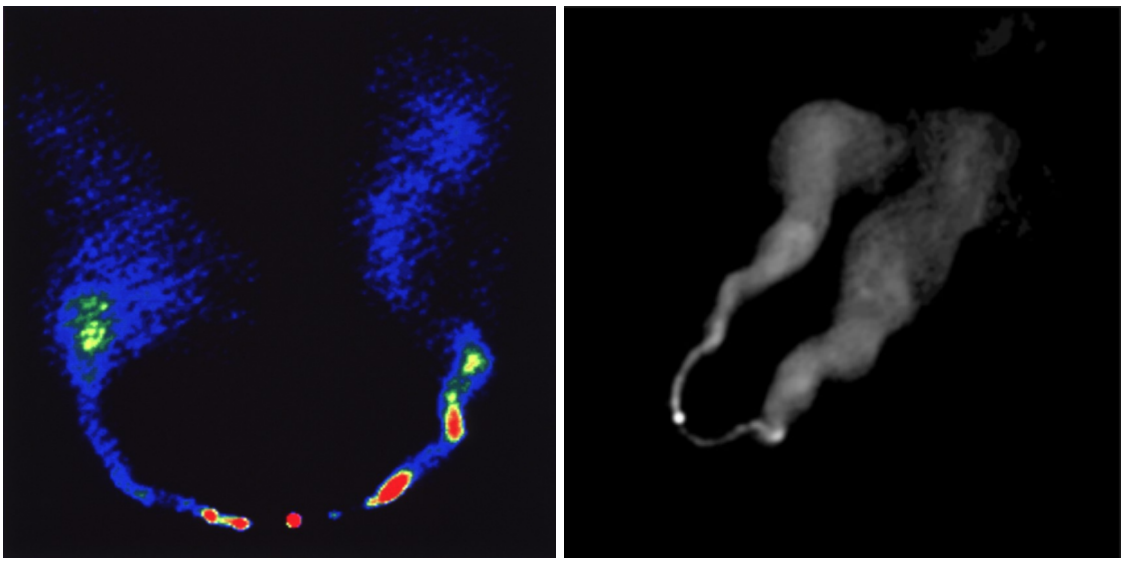

Figure 1.4: *Left:* Very Large Array (VLA) image of a prototype WAT galaxy NGC1265 (O'Dea & Owen, 1986). The high velocity motion of the associated elliptical galaxy through its surrounding ICM produces ram pressure on the jets and cause them to bend. *Right:* radio emission of 3C 129, a head-tail or NAT RG.

Another classification of RGs can be made regarding the characteristics of their optical spectra:

Low-excitation Radio Galaxies and High-excitation Radio Galaxies (LERGs and HERGs respectively, see Laing et al., 1994). Unlike the morphological distinction, the difference between these two types is not simply related to orientation effect, but would reflect the accretion rate onto the black hole (see Buttiglione et al., 2009, and references therein). While all FR Is for which a reliable classification can be established are LERGs, both LERGs and HERGs are found among the FR IIs (e.g., Buttiglione et al., 2010).

- **LERGs. Low-excitation Radio Galaxies:** For this subclassification lines such as [OIII] ($\lambda_{[OIII]} = 5007$ Å) are very weak in comparison with the hydrogen lines, ratios for [OII] ($\lambda_{[OII]} = 3727$ Å) and [OIII] are [OII]/[OIII] > 1 and equivalent widths (EWs) of [OIII] $<$ 3 Å. They are characterized by low accretion efficiency, less than $\sim 1\%$ of the Eddington luminosity, being the Eddington luminosity the maximum luminosity of a source of mass M that is powered by spherical accretion. At low accretion rate, a radiatively inefficient advection dominated accretion flow can form. There is a lack of UV continuum that leads to a dearth of strong emission lines. It is possible to find LERGs among both FR Is and FR IIs and they are usually hosted by red passive galaxies. The fuelling mechanisms for LERGs are still uncertain since they do not show the characteristic optical and X-ray features of radiatively efficient accretion seen in radiative AGNs, and probably they are fuelled by a hot, radiatively inefficient flow or advection dominated accretion flow (Baldi & Capetti, 2008).

- **HERGs. High-excitation Radio Galaxies:** Defined as galaxies with flux ratio of the emission lines [OIII] ($\lambda_{[OIII]} = 5007$ Å) and Hα ($\lambda_{H\alpha} = 6564.61$ Å) of [OIII]/H$\alpha > 0.2$ and EWs of [OIII] > 3 Å. The optical spectrum composed by strong emitting lines reflects the presence of a radiatively efficient accretion disk surrounding the central SMBH, to form such disk HERGs typically have high accretion rates, between 1% and 10% of their Eddington luminosity. The UV radiation field from the disk ionizes surrounding gas, leading to the presence of high-excitation emission lines. HERGs are only found among FR IIs. Their host galaxies typically show lower stellar mass than LERGs, with lower black hole masses, bluer colors and less pronounced 4000 Å breaks, indicating younger stellar populations (Olguín-Iglesias et al., 2016). These results suggest that the RGs belonging to the two spectroscopic classes correspond to different manifestation of the radio loud AGN phenomenon, where HERGs are thought to be fuelled by cold gas coming from galaxy mergers and interaction, that is channeled to the galaxy center making it available for star formation (Best & Heckman, 2012).

1.3 Blazars

The extreme characteristics of blazars that are described in the following sections are explained by the Unification Scenario, in which blazars are RGs with jets pointing at our line of sight rather than in the plane of the sky. Because of their special orientation, blazars constitute the rarest class of AGN and therefore offer a direct probe of the energy production in the center of AGNs.

1.3.1 Discovery and historical overview

BL Lacertae is an object first discovered by Cuno Hoffmeister in 1929 (Hoffmeister, 1929) and it was classified as an irregular variable star for many years. Almost 40 years later a bright radio source, VRO 42.22.01 was found to share its location with BL Lacertae (Schmitt, 1968). BL Lacertae was one of the only two known non-cepheid extragalactic variable stars at the time, and when the optical spectrum was acquired it was found featureless, laking any emission or absorption lines. Few years

later four more objects similar to BL Lacertae were identified by Strittmatter et al. (1972). These authors found the characteristics of BL Lac objects to be very similar to those of QSOs, both showing extragalactic compact non-thermal emission and rapid variations in intensity and polarization, being the only difference that BL Lacs did not have spectral lines.

Later on, Oke & Gunn (1974) discovered that BL Lacertae was located in a normal giant elliptical galaxy at z = 0.07 with a luminosity of $L_{bol} = 10^{46}$ erg s^{-1}. The properties violent variability, compact radio emission, flat radio spectrum, strong continuum emission and high polarization were common to BL Lacs, some QSOs and RGs. In a banquet speech at the Pittsburgh meeting on BL Lacs (1978), Ed Spiegel suggested the name "blazar" for this class of objects, a combination of BL Lac and quasar. This name became official with the review paper by Angel & Stockman (1980), where they also gave the first list of BL Lacs, containing 57 sources.

Blandford & Rees explained at the same Pittsburgh Conference the unusual properties of blazars in terms of non-thermal emission from particles moving down a jet with a velocity very close to the speed of light, observed at a small angle with respect to the line of sight.

1.3.2 Blazar classification

BL Lacs

BL Lacs are those blazars showing featureless optical spectrum or optical emission/absorption lines with EW smaller than 5Å (Stickel et al., 1991). Their lack of any emission/absorption features makes the redshift determination challenging (as in left panel of Fig. 1.5). At IR-optical wavelengths these sources show a power law spectra defined as $S_\nu \propto \nu^{-\alpha}$, with indices in the range $\alpha_\nu \sim 0.5 - 1.5$.

Padovani & Giommi (1995) classified BL Lacs using the peak energy of the synchrotron emission in the SED, according to whether the ratio α_{rx} between 5 GHz and 1 keV is greater or smaller than 0.75:

- **HBL, High-energy peaked BL Lacs:** $\alpha_{rx} < 0.75$. Their mean extended radio power is more than an order of magnitude lower than for their low-energy counterpart, low-energy peaked BL Lacs (LBLs). Furthermore their radio cores appear relatively unbeamed, as if they were intrinsically less luminous or relatively "off-axis" in the radio band. On average, this class have lower polarization, less variability, they are less core-dominated and their bolometric luminosities are smaller than LBLs. In the spectral energy distribution (SED), their first peak of the synchrotron emission is in the soft X-rays ($\nu_{synch} \geq 10^{15}$ Hz), and the second peak correspondent to Compton emission peaks in the γ-rays, sometimes even at TeV energies. They were previously known as X-ray selected BL Lacs (XBLs) because most of them have been found on X-ray surveys (see e.g. Perlman & Stocke, 1993; Jannuzi et al., 1994).

- **LBL, Low-energy peaked BL Lacs:** $\alpha_{rx} > 0.75$. The peak of the synchrotron component is typically at IR/optical wavelengths at $\nu_{synch\ peak} \leqslant 10^{14}$ Hz, while the Compton emission peaks at γ-rays, typically at GeV energies. BL Lacs of this class are more polarized, more variable and more luminous than HBLs. They were previously known as Radio selected BL Lacs (RBLs) because this class has been found on radio surveys.

- **IBL/ISP, Intermediate-energy peaked BL Lacs** They have intermediate characteristics between the two other classes previously defined, $10^{14} \leqslant \nu_{synch\ peak} \leqslant 10^{15}$ Hz (Bade et al., 1998).

Flat Spectrum Radio Quasars

These sources were previously known as Optically Violently Variables (OVV, see e.g. Bregman et al., 1988). Their optical spectrum show quasar-like broad emission lines as seen in the right panel of Fig. 1.5, with EWs larger than 5 Å (Stickel et al., 1991) and they also show a flat radio spectrum ($F_\nu \propto \nu^{-\alpha}$ with $\alpha < 0.5$). The most commonly observed lines are those of Lyα ($\lambda = 1216$ Å), CIV ($\lambda = 1549$ Å), CIII ($\lambda = 1909$ Å), MgII ($\lambda = 2798$ Å), [OIII] ($\lambda = 4363$, 4959, 5007 Å), and the Hydrogen Balmer series. This luminous broad emission lines are often accompanied by prominent UV-optical continuum emission (blue bump) of thermal origin.

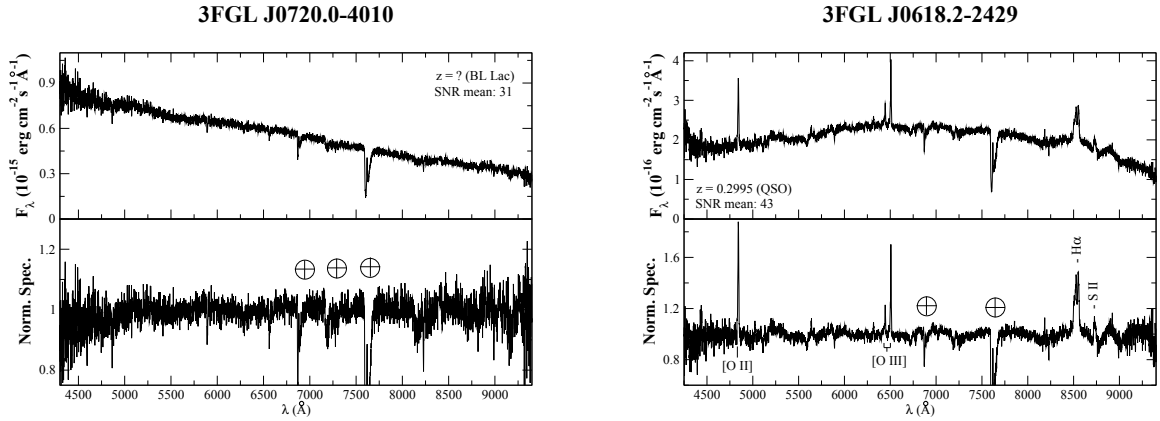

Figure 1.5: *Left:* Featureless optical spectrum of the BL Lac WISE J071939.18-401147.4, associated with the γ-ray source 3FGL J0720.0-4010. Non-thermal emission spectrum, the lack of any emission/absorption features does not allow to measure the redshift. *Right:* The optical spectrum of WISE J061822.65-242637.7, a FSRQ associated with 3FGL J0618.2-2429. It is possible to distinguish the emission lines [O II], the doublet [O III], Hα and [S II]. Both spectra reported in Álvarez Crespo et al. (2016c).

FSRQs are in general more luminous and distributed to much higher redshift than BL Lacs, with their redshift distribution peaking roughly at z $\sim$ 1.2 - 1.4 while BL Lacs are much closer with a peak on their redshift distribution at z $\sim$ 0.3, as in Fig. 1.6. There are very few BL Lacs known at redshift larger than 1, being the most distant one 3FGL J1450+5200, found at $z > 2.470$ (Paiano et al., 2017), while the most distant FSRQ is 5BZQ J1556+3517 at z = 6.802 (Massaro et al., 2015a).

1.3.3 Observational properties and theoretical interpretation

Blazars are radio loud AGNs characterized by non-thermal emission over the entire electromagnetic spectrum, extending from radio up to γ-rays. All their properties are explained by their particular orientation since one of their jets is almost aligned with respect to our line of sight:

- **Relativistic beaming.** It was originally suggested by Blandford & Rees (1978) to explain most of the properties of blazars, such as apparent superluminal motions and rapid variability. This effect is expressed using the relativistic Doppler factor δ, more details about its calculation are reported in the Appendix 1. This factor strongly depends on the angle to the line of sight. For blazars the relativistic Doppler factor has a typical value of $\delta \sim 10$ - 20 (see e.g. Liodakis et al., 2017).

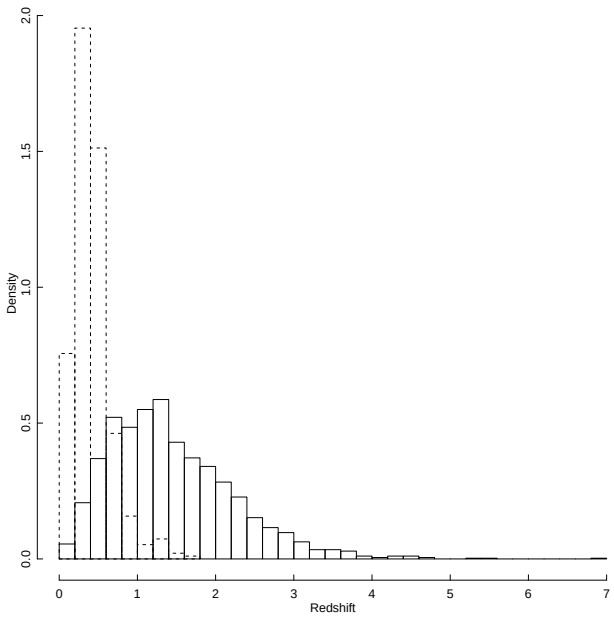

Figure 1.6: The redshift distributions of BL Lac objects including candidate sources (dashed histogram) and of FSRQs (solid line histogram) reported in the 5-th edition of the Roma-BZCAT.

The apparent luminosity is increased since the radiation emitted by relativistically moving particles is beamed towards the direction of motion. At very small angles with respect to the line of sight, the effect becomes quite large and the observed luminosity may be hundreds and even thousands of times higher than the intrinsic luminosity of a source. This scenario is also responsible of cases in which even though jets always come in pairs, only one is visible since the surface brightness of the jet that is approaching to the observer is enhanced, while the receding jet appears fainter (see e.g. Leon et al., 2016).

Relativistic beaming is also responsible of strong and fast variability in every emission band blazars have been studied, as explained in Appendix 1. Fluxes can vary by several magnitudes on times scales from months to years, while microvariability changes of 0.1 mag on time scales as short as hours has been confirmed in some blazars (see e.g. Miller et al., 1989).

- **Apparent superluminal motions.** This effect is observed in a large number of QSOs and BL Lacs, in particular in radio wavebands (see e.g., Ghisellini et al., 1993). The term superluminal motion describes the proper motion of a source structure that, when converted to an apparent speed v_a, gives $v_a > c$. This occurs for emitting regions moving at relativistic speeds at small angles to the line of sight (as shown in the Appendix 1).

- **Spectral Energy Distribution.** The spectral energy distribution (SED) of blazars is characterized by two humps, one at lower energies peaking between the far-IR and soft X-rays, and a second one peaking in the γ-rays in the MeV - GeV range. For BL Lacs the low energy component of the SED is due to synchrotron emission from relativistic particles, while the high energy hump is interpreted as inverse Compton (IC) scattering. The details related to the physics of these emission processes are reported in the Appendix 2. A larger frequency of the first hump corresponds to a larger frequency of the second hump and viceversa (see left panel Fig. 1.7), which has led to understand the SED of BL Lacs in a synchrotron self-Compton scenario, were the inverse Compton scattering at high energies is caused by the same popula-

tion of electrons than emit synchrotron in the lower component (Ghisellini & Maraschi, 1989). For FSRQs, their SEDs are dominated by the inverse Compton component, with most of their luminosity emitted in γ-rays. In this case it is though that the highly relativistic electrons interact with photon sources external to the jet, like photons coming from the accretion disk surrounding the black hole in the center of the active galaxy, from the broad line regions or the dusty torus. This is the External Compton scenario (EC, see e.g. Dermer & Schlickeiser, 1993; Sikora et al., 1994; Arbeiter et al., 2002).

Fossati et al. (1998) proposed the so-called "blazar sequence", which connects the observed bolometric luminosity to the shape of the SED of blazars (see right panel of Fig. 1.7). The main result of this study is that the shape of the SED changes in a coherent way with the bolometric luminosity L_{bol}. According to this sequence, the synchrotron peak occurs at different frequency for different bolometric luminosity, with most luminous sources peaking at lower frequencies. At the same time the luminosity ratio between the the Compton and the synchrotron humps increases with bolometric luminosity. These results were interpreted by Ghisellini et al. (1998) as due to the different amount of radiative cooling suffered by the emitting electrons in different sources, under the assumption of a common heating mechanism. On the other hand, Giommi et al. (2012) using Monte Carlo simulations proposed that the existence of a strong anti-correlation between bolometric luminosity and the frequency of the synchrotron peak is likely a selection effect, resulting from comparing shallow radio surveys with shallow X-ray surveys.

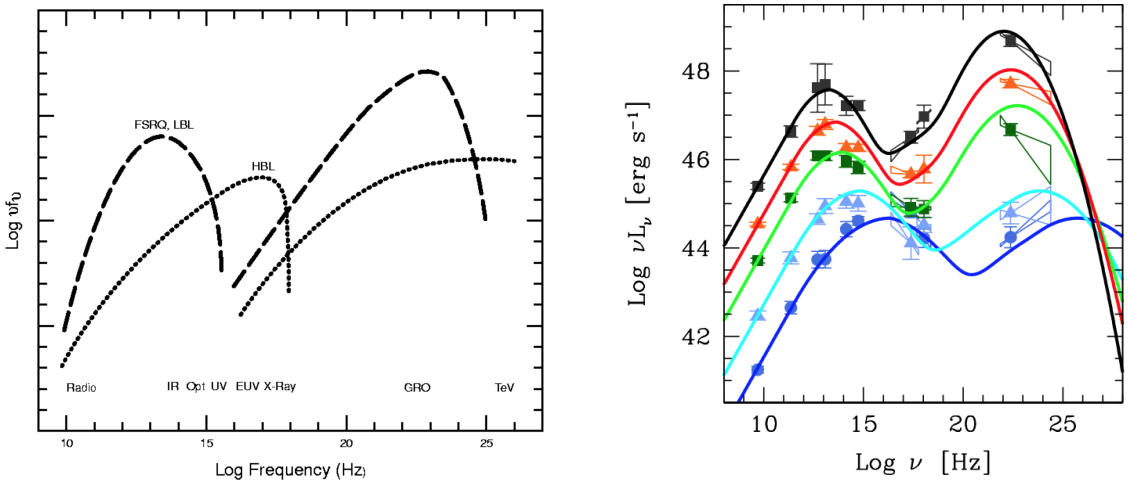

Figure 1.7: *Left:* a schematic representation of the SED of a typical LBL/FSRQ (dashed line) and a HBL (dotted line). The first hump of the LBL/FSRQ peaks in the far-IR, while for the HBL that first bump peaks in the soft X-rays. For the three cases the second bump falls in the γ-rays, but a LBL/FSRQ peaks at lower energies (MeV - GeV) than a HBL. *Right:* blazar sequence of a sample of 126 blazars belonging to flux limited radio and X-ray samples (Fossati et al., 1998).

- **High lineal polarization.** Relativistic effects should result in significant polarization of the accretion disk continuum. These sources have a polarization up to a a few percent (≤ 3 - 4%), as opposed to less than $\sim 1\%$ for most AGNs, sometimes with jet regions having an extreme polarization fraction, up to 50% (Lister & Homan, 2005).

- **Compact radio emission and flat radio spectrum.** Blazars are usually characterized for having bright compact and often unresolved cores up to 10^{31} erg s^{-1} Hz^{-1}, and a weaker extended jet often also unresolved because it is seen transversely, as in Fig. 1.8. The core

spectrum follows a power-law with flat shapes ($F_\nu \propto \nu^{-\alpha}$ with $\alpha < 0.5$) mostly produced by synchrotron radiation, often partially self-absorbed at the GHz frequencies (see e.g. Willott et al., 2001; Falomo et al., 2014).

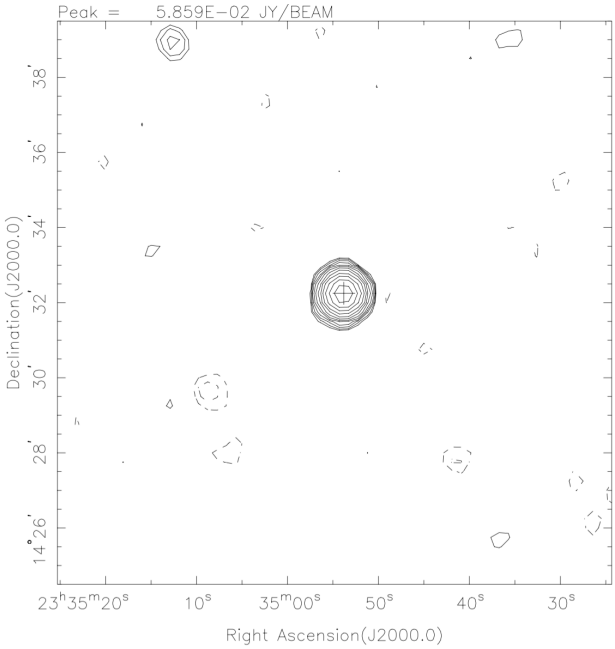

Figure 1.8: 15'×15' NVSS radio image at 1.4 GHz from the BL Lac 5BZB J2334+1432 at unknown redshift showing compact radio emission.

- **Peculiar IR colors.** Blazars have been found to occupy a different region in the IR color-color space with respect to other extragalactic sources. Massaro et al. (2011) represented all the population of extragalactic sources in a [3.4]-[4.6]-[12] μm color-color diagram using data collected with the Wide-field IR Survey Explorer (WISE) survey (Wright et al., 2010), discovering that blazars lie in a narrow region called Wise Blazar Strip (WBS). This is due to the fact that blazars are dominated by non-thermal emission, while other extragalactic classes of galaxies emit thermal radiation at IR frequencies. Moreover the two main classes of blazars, BL Lacs and FSRQs (BZBs and BZQs respectively according to the nomenclature in the 5-th edition of the Roma-BZCAT (Massaro et al., 2015a)) are themselves separated in the WBS, with BZQs redder and lying closer to the normal QSOs and Seyfert galaxies (see Fig. 1.9).

  Later on, D'Abrusco et al. (2013) extended this analysis to the 3-dimensional color-color plot for the γ-ray emitting blazars, a subsample from the previous case, finding they lie on a cylinder so-called *locus*. Using this discovery, D'Abrusco et al. (2014) assembled the Wise Blazar-Like Radio Loud Sources catalog (WIBRaLS), an all-sky catalog of radio loud candidate γ-ray emitting blazars with WISE mid-IR colors similar to those of confirmed γ-ray blazars. The catalog was built using WISE sources detected in all four WISE filters, [3.4], [4.6], [12], and [22] μm, with colors compatible with the *locus*, the three-dimensional color space of the confirmed γ-ray emitting blazars. This catalog has been a successful resource to identify blazars among unidentified high-energy sources.

- **Gamma-ray emission.** Many of the observations conducted in the MeV - GeV range from space observatories detected large numbers of blazars, with their integrated luminosities in the

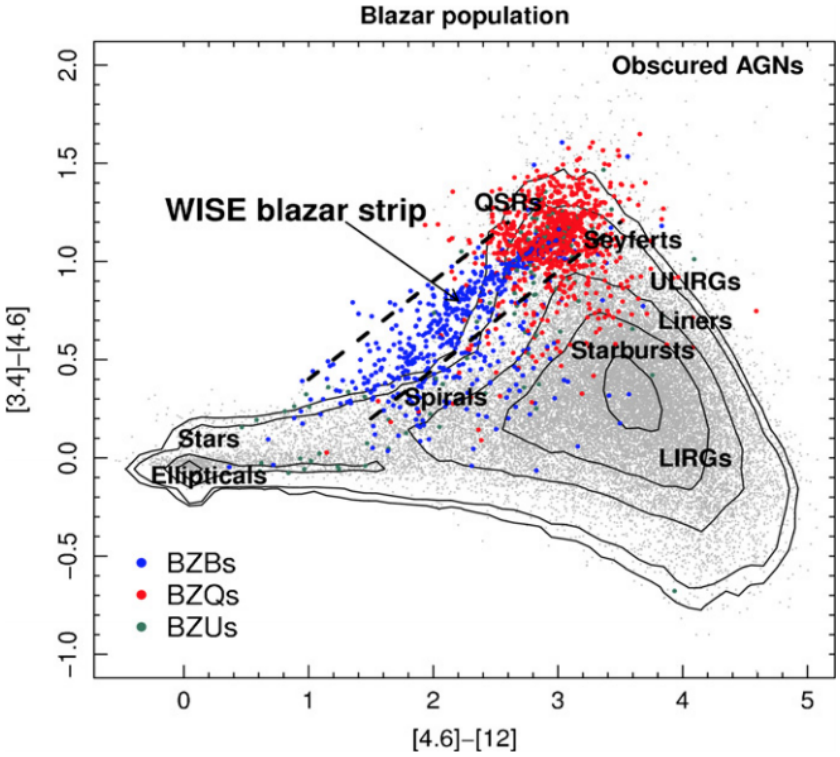

Figure 1.9: [3.4]-[4.6]-[12] μm color-color diagram of WISE thermal sources and blazars. There are 1,365 blazars associated with a WISE source within a region of radius 2.4". The two blazar classes, BL Lacs (BZBs blue filled circles) and FSRQs (BZQs red filled circles) are shown together with the blazars of uncertain type (BZUs, green filled circles). The background grey dots correspond to the other WISE thermal sources, where QSRs, ULRIGs, and LIRGs indicate the quasars, the ultraluminous IR galaxies, and the luminous IR galaxies, respectively. The WBS is highlighted within the two black dashed lines.

range 0.1 - 10 GeV reaching up to 10^{48} erg s^{-1}. Blazars are the largest known population of γ-ray sources. In fact 61% of the sources associated in the the Third Fermi γ-ray LAT point source catalog (3FGL, Acero et al., 2015) are blazars, and 32% show multifrequency properties similar to those of blazars but they lack of spectroscopic confirmation. In addition, photons from blazars were detected from the ground atmospheric Cherenkov radiation telescopes. The γ-ray emission dominates the spectral energy distribution of blazars, especially during flaring states, and is highly variable (down to sub-hour time-scales Aharonian et al., 2009).

1.4 Unification Scenario for radio loud AGNs

In the Unification Model it is possible to link RGs and blazars. At high luminosities, FR II RGs are considered as the parent population of FSRQ. Similarly, for the low luminosity radio loud objects, FR I RGs are believed to be the misaligned parent population of BL Lacs (Urry et al., 1991). This associations are based on the existence of strong high excitation lines in both FSRQs and FR IIs and the absence of strong emission lines in both BL Lacs and FR Is, thus the nuclear structure of high and low power objects may differ in some crucial aspects.

There is evidence for the unifying picture for radio loud AGNs. In the 80's, it was noted that the extended radio emission of BL Lacs was comparable to that of FR Is (Browne, 1983; Antonucci & Ulvestad, 1985). FSRQs are hosted in bright massive ellipticals, which are similar in magnitude and morphology to FR IIs host. The same result holds for BL Lac host galaxies, which appears to be similar to those of FR Is (see e.g. Ulrich, 1989; Scarpa et al., 2000). Urry et al. (1991) studied this unification scheme by comparing the FR I luminosity function with that of BL Lacs, including the estimates of the beaming parameters from VLBI observations. Through a direct comparison of predicted and observed luminosity functions, these authors showed that available radio samples of FR I RGs and BL Lac objects are fully consistent with the beaming hypothesis, supporting the Unification Scenario. From the extended radio properties it can be derived that the radio structure of blazars is compatible with being aligned RGs (Padovani & Urry, 1992). As already stated, one of the facts that supports the Unification Scenario is that while only weak line emissions are detected in both for FR Is and BL Lacs, FSRQs and FR IIs show strong high excitation lines (see e.g. Hes et al., 1993; Laing et al., 1994). In addition, the superluminal motions of optical components observed with the Hubble Space Telescope (HST) in M87, with an apparent speed in the range 4-6c, are in agreement with those for BL Lacs (Biretta et al., 1999). For two different low-power RGs, Centaurus A and NGC 6251, the nuclear SED from the radio to the γ-ray band has been determined and in both cases the emission can be understood in terms of a misaligned BL Lac, thus supporting the unification scenario (Chiaberge et al., 2001, 2003).

However, there are still open issues for this Unification Model for which further investigation is needed. It is not yet clear whether the narrow-line luminosities of BL Lacs, when observed, are consistent with those of FR Is (Stickel et al., 1993). Since low power objects lack strong emission lines, obscuration of a BLR by a dusty torus like in the high power case does not need to be invoked. It has been proposed that the FR Is and BL Lacs intrinsically lack a BLR, possibly because of a weaker ionizing continuum (Chiaberge, 2004). The parameters governing the physical division into low-power and high-power objects are still unknown. One unsolved issue for the unification is the role played by LERGs, because they show an FR II radio morphology but their optical spectral properties are those of FR Is. It is not yet evident that BL Lacs and FR Is share the same type of environment (see e.g. Gendre et al., 2013). The environment of FR Is has been extensively studied finding they are predominantly found in low density clusters (as further discussed in Chapter 2), while for BL Lacs the picture is not that clear.

CHAPTER 2

Environments

2.1 Groups and clusters of galaxies

The history of galaxy clusters started about 200 years ago, when the French astronomer Charles Messier published its famous "Catalogue des Nébuleuses et des Amas d'Étoiles" ("Catalogue of Nebulae and Star Clusters"), to define the positions of nebulae to do not misidentify them with new comets (Messier, 1781). Many astronomers of the XIX and early XX century took photographic observations of nebulae to establish whether they were external to our galaxy or not (Keeler, 1900; Rosse & Parsons, 1880). The answer came in the early 20's, when Edwin Hubble discovered cepheids in M31 and definitely corroborated their extragalactic nature. Several years later in 1933 Zwicky, by comparing the masses of galaxy clusters measured using the virial theorem and those from rotation curves, noticed that the mass was underestimated, establishing the need for dark matter (Zwicky, 1933).

A great advance in the systematic study of the properties of clusters occurred in the 50's when Abell visually inspected the Palomar Sky Survey plates and compiled an extensive catalog of 2,712 clusters of galaxies and identified them with a well-defined set of selection criteria (Abell, 1958). This catalog has been a very important resource in the study of galaxy clusters to the extent that the scale to measure the richness of a galaxy cluster, i.e., the number of galaxies associated with that cluster, still refers to the what is defined in the Abell catalog. Abell richness classes go from 0 to 5, being class 0 a cluster with 30 - 49 galaxies, class 1 with 50 - 79 galaxies, class 2 with 80 - 129 galaxies, class 3 with 130 - 199 galaxies, class 4 with 200 - 299 galaxies and finally class 5 with more than 299 galaxies. Further results were achieved by de Vaucouleurs (1971) who shifted focus to poorer systems by studying nearby groups of galaxies. Gott & Turner (1977) made the first measurement of the group multiplicity function using the Turner & Gott (1976) catalog of groups, selected basing on the projected surface density of galaxies.

In 1966, Geiger counters on board of the rocket Areobee 150 detected X-ray emission around the galaxy M87 in the center of the Virgo cluster, being the first X-ray emitter found outside of our galaxy (Byram et al., 1966). After five years Coma and Perseus were also detected in the X-rays, which suggested that clusters were X-ray Sources (Cavaliere et al., 1971), confirmed by a survey

Figure 2.1: *Left:* Optical image taken with the Advanced Camera for Surveys (ACS) onboard NASA's Hubble Space Telescope of the core of the massive cluster RDCS 1252.9-2927. In this case two elliptical galaxies dominate the center of the cluster. *Right:* Optical image taken with the Gemini telescope of HCG 87, a nearby compact galaxy group composed of a large edge-on spiral galaxy visible near the image center, an elliptical galaxy visible to its right, and a spiral galaxy visible near the top.

with the X-ray satellite Uhuru (Giacconi et al., 1972).

Clusters and groups of galaxies are the largest gravitationally bound systems in the universe and they form its basic building blocks. Interactions within the group or cluster environment may have important effects on the star formation history, morphology, dynamics, and other properties of member galaxies. Galaxy clusters are usually located at the knots of the filamentary large-scale structures in the universe, and are composed typically from thirty to thousands of galaxies, see Fig. 2.1 left panel, with total masses up to 10^{15} $M_{\odot}$ and sizes of $\sim$ 1 - 2 Mpc.

Groups of galaxies however are smaller aggregates of galaxies. They can contain from 2 up to a few tens of galaxies (see Fig. 2.1 right panel) in sizes of $\sim$ 0.1 - 1 Mpc and having a total mass about 10^{13} $M_{\odot}$ (Bahcall & Oh, 1996). Familiar examples include the Local Group and the M81 group. However there is not sharp line between the two classes, a big group can be considered as a cluster. Groups are the most common structures of galaxies in the universe, comprising up to 55% of the galaxies in the local universe, while clusters are rare containing only about 5%. Typical properties of clusters and groups of galaxies are summarized on Table 2.1.

About 90% of the total mass in galaxy clusters is dark matter, while about 9% is represented by intergalactic medium (IGM), a hot X-ray emitting plasma between the cluster galaxies and extending as far as the main galaxy concentration (Dvorkin & Rephaeli, 2015). The typical temperature of this hot IGM ranges from 2 to 14 keV and the central gas density is $\sim 10^{-3}$ electrons cm^{-3}, see Fig. 2.2. The luminous X-ray emission is produced by thermal bremsstrahlung radiation, with $L_x \sim 10^{44}$ erg s^{-1} (Burg et al., 1994). Galaxies and their stars contribute to only about 1% of the total mass of a cluster.

Bright galaxies typically reside in groups or clusters, surrounded by less luminous neighbours. Spiral galaxies, i.e., late-type galaxies, are preferentially located in low-density environments and are usually isolated, while early-type galaxies, i.e., ellipticals and lenticulars are usually found as

Property	Rich clusters	Groups and poor clusters
Richness	30-300 galaxies	3-30 galaxies
Radius	(1-2) h^{-1} Mpc	(0.1-1) h^{-1} Mpc
Radial velocity dispersion	400-1400 km s^{-1}	100-500 km s^{-1}
Radial velocity dispersion (median)	$\sim$ 750 km s^{-1}	$\sim$ 250 km s^{-1}
Mass ($r \leq 1.5$ h^{-1} Mpc)	$(10^{14} - 2 \cdot 10^{15})$ $h^{-1} M_{\odot}$	$(10^{12.5} - 10^{14})$ $h^{-1} M_{\odot}$
Luminosity ($r \leq 1.5$ h^{-1} Mpc)	$(6 \cdot 10^{11} - 6 \cdot 10^{12})$ $h^{-2} L_{\odot}$	$(10^{10.5} - 10^{12})$ $h^{-2} L_{\odot}$
$< M / L_B >$	$\sim$ 300 h $M_{\odot}/L_{\odot}$	$\sim$ 200 h $M_{\odot}$ / $L_{\odot}$
X-ray temperature	2-14 keV	$\leq$ 2 keV
X-ray luminosity	$(10^{42.5}$ - $10^{45})$ h^{-2} erg s^{-1}	$\leq 10^{43}$ h^{-2} erg s^{-1}
Cluster number density	$(10^{-5}$ - $10^{-6})$ h^3 Mpc^{-3}	$(10^{-3}$ - 10^{-5}) h^3 Mpc^{-3}
Fraction of galaxies in	$\sim$ 5%	$\sim$ 55%

Table 2.1: Typical properties of galaxy clusters and groups (Bahcall, 1999).

members of clusters (Postman & Geller, 1984). While ∼70% of the cluster galaxies are red elliptical galaxies, the group population is a mixed bag of morphologies.

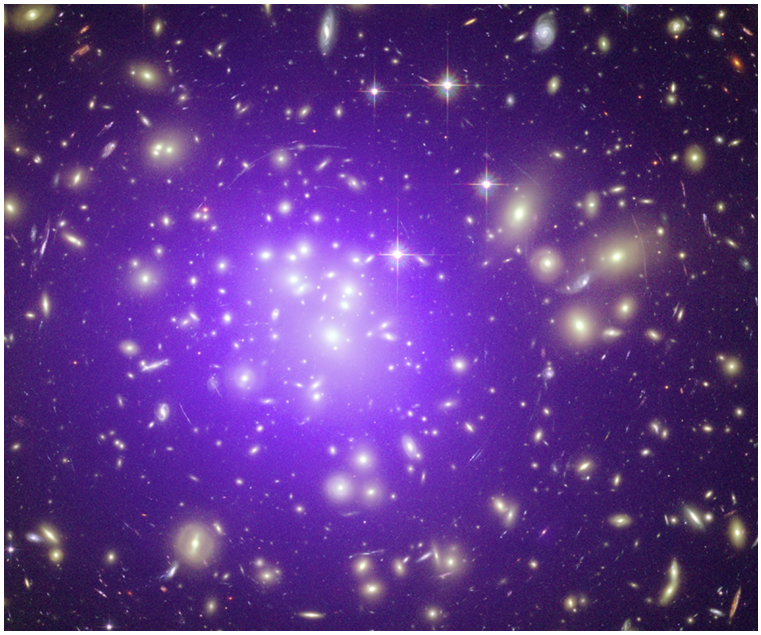

Figure 2.2: Composite image of the massive cluster Abell 1689. Gas at 10^8 K detected by NASA's Chandra X-ray is shown in purple.

Galaxy clusters have been extensively studied to understand how large-scale structures form and evolve during cosmic time. Most studies of the luminosity function evolution in clusters of galaxies are consistent with a scenario in which cluster galaxies formed in short, vigorous bursts of star formation at high redshift ($z > 2$) and evolved passively thereafter (Eisenhardt et al., 2008).

Each galaxy cluster has a Brightest Cluster Galaxy (BCG), generally found at its geometrical and kinematical center and also generally coincident with the peak of the cluster X-ray emission. BCGs are very massive elliptical galaxies, including the most massive galaxies in the local universe,

with old stellar populations and relatively low star-formation rates, and usually hosting a SMBH. They constitute a separate population from bright elliptical galaxies, and both their homogeneity and extreme luminosity have motivated their use as standard candles for cosmology (Lauer et al., 2014).

There is a relation between the cluster X-ray luminosity L_X and temperature (kT), and it can often be approximated as a simple power law with a slope $\sim$ -3 (see Fig. 2.3). Understanding the evolution of the L_X - kT relation is important as a step in the process of providing mass estimates for high redshift clusters, understanding the selection functions of X-ray cluster surveys, and also for probing the history of their heating mechanisms (Maughan et al., 2012).

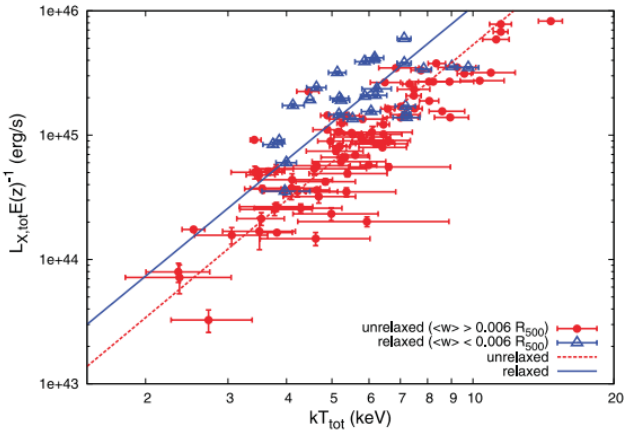

Figure 2.3: L_X - kT relation for a sample of 114 galaxy clusters observed with Chandra at $0.1 < z < 1.3$, separated into relaxed/unrelaxed subsamples (no recent mergers/merging clusters) taken from Maughan et al. (2012).

Galaxy clusters contain a well-defined, highly regular population of elliptical and lenticular galaxies. The existence of a uniformly old stellar population in these galaxies gives them remarkably similar SEDs with a strong 4000 Å break, thus galaxies within clusters are tightly "clustered" in both color and space in the so-called "Red Sequence" (see e.g. Gladders et al., 1998). An elliptical or lenticular galaxy of a certain redness in a cluster have a certain absolute magnitude, the faint galaxies are bluer than the bright cluster members (see Fig. 2.4). It is therefore possible to find clusters by looking for this property without worrying about projection effect problems. This relation only applies to early-type galaxies, while spirals, on the whole, tend to be bluer and do not demonstrate such a trend (Bower et al., 1992).

There are several methods to search for galaxy clusters by using their properties:

- The most obvious and straightforward method is to count the individual galaxies detected through optical imaging and spectroscopy, and search for overdensities of galaxies at the same redshift. This can be applied to the infrared band to find clusters at high redshift. The advantage of this method is that a lot of information is available in optical surveys such as Sloan Digital Sky Survey (SDSS, York et al., 2000; Eisenstein et al., 2011), but the drawback is that projection effects can be very important. Such projection effects can be partially solved by measuring the redshift. Recently, several group catalogues have been produced using the algorithm Friends of Friends (FoF) on optical surveys with spectroscopic redshifts, based on

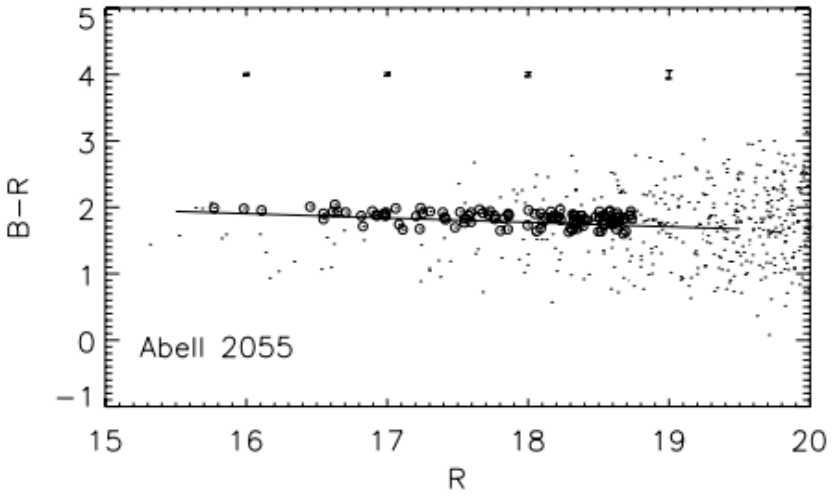

Figure 2.4: Example of the red sequence for the cluster Abell 2055, taken from Stott et al. (2009). Each big circle describes the color and brightness of an individual galaxy in the cluster, while small dots are background galaxies. The black line represents the red sequence. Representative error bands are shown on the top part of the figure.

the Two-degree Field Galaxy Redshift Survey (2dFGRS, see e.g. Eke et al., 2004; Tago et al., 2006) and on early releases of the SDSS (see e.g. Berlind et al., 2006; Tempel et al., 2012).

- It is possible to detect the hot ICM in the X-rays, since this emission points directly towards the existence of a potential well within which the gas is in dynamical equilibrium with the galaxies and the dark matter. Most clusters show bright, extended X-ray emission strongly peaked in their core. One of the first surveys of X-ray clusters of galaxies was the ROSAT Brightest Cluster sample (BCS, Ebeling et al., 1997), a X-ray flux limited sample of 199 clusters of galaxies in the northern hemisphere compiled from ROSAT All-Sky Survey data (Voges et al., 1999). A recent catalog is the XXL survey (Pierre et al., 2017), that compresses 500 independent XMM-Newton observations totalling ~ 6.9 Ms, the largest XMM programme to date. This survey was designed to provide a sample of ~ 500 clusters of galaxies out to a redshift $z \sim 1$, suitable for cosmological study. The survey is still ongoing and the 2016 results pertain to about 1/5 of the complete cluster sample. Another recent resource is the Cosmic Evolution Survey (COSMOS, Scoville, 2007), that combines a large 2 square degree area, deep multiwavelength information and high resolution imaging.

- Hot electrons in the ICM scatter radiation from the cosmic microwave background through the inverse Compton process. This produces a "shadow" in the observed cosmic microwave background at radio frequencies, known as the "Sunyaev-Zel'dovich effect" (SZ). It was presented an all-sky *Planck* catalogue of SZ sources detected from the 29 month full-mission data, the largest SZ-selected sample of galaxy clusters (Planck Collaboration et al., 2016). The highest redshift cluster ever detected to date in SZ is at $z \sim 1.9$ (Mantz et al., 2014).

2.2 The large-scale environments of RGs

The environments of RGs has been a extensively studied topic during the years. Back in the 70's, Longair & Seldner (1979) developed an objective estimate of the degree of clustering of radio sources. These authors were the first to use the autocorrelation function to describe quantitatively the association of an unbiased sample of radio sources of different luminosities and types, with groups and clusters of galaxies at $z < 0.1$. Briefly, the technique is as follows: all galaxies within a certain radius from the radio source brighter than some magnitude are counted. Then background galaxies in that area down to the same magnitude are subtracted. The number of excess galaxies is normalized to using an evolved galaxy luminosity function at the redshift of the object. These authors established that sources with double structure, i.e., FR IIs lie in regions of low galaxy density, whereas the more complex sources, i.e., FR Is are members of groups and clusters. Later on, Prestage & Peacock (1988, 1989) extended this method to higher redshift, $z < 0.25$, reaching the same conclusions. Since then, several studies have reinforced the hypothesis that FR Is and FR IIs inhabit different environments, and that the pressure due to the intergalactic medium is what prevents the formation of the classical double lobe structure of FR IIs leading FR Is (see e.g. Gonzalez-Serrano et al., 1993).

In the 90's, Hill & Lilly (1991) presented a study of the environments of about 50 radiogalaxies at $z \sim 0.5$ and compared them with the low redshift results of Prestage & Peacock (1988, 1989). The most striking difference found among both epochs is that FR II radio sources often inhabit rich-cluster environments at $z \sim 0.5$, but avoid them at lower redshift. These authors found that powerful radio sources at $z \sim 0.5$ inhabit Abell richness class 0 clusters (between 30 and 49 galaxies) on average. Low-power radio sources, on the other hand, do not show a significant change in environment between the two epochs. The same result was found by Zirbel (1997), pointing out that about twice as many FR II galaxies than FR Is show either interactions and/or have a neighbour within 50 kpc. Hardcastle & Worrall (1999) studied the X-ray gas emission in the large-scale environment of a sample of the revised 3C catalogue of radio sources (3CR, Bennett, 1962) galaxies, and determined that as in previous studies FR Is tend to lie in galaxy groups or in moderately rich clusters. For the FR IIs, several low-redshift FR II sources also show extended X-ray emission, but others must inhabit relatively poor environments. At higher redshifts, these author have found evidence for luminous X-ray emission surrounding several FR IIs, implying rich cluster environments for these sources.

On the other hand, more recent studies such as McLure & Dunlop (2001) found no epoch-depent change in cluster richness of RGs out to $z \sim 0.5$. Miller et al. (2002) performed multifiber optical spectroscopy on 25 galaxies in the vicinity of low redshift RGs, and found that all FR Is in their sample reside in clusters, whereas FR IIs often appear to be recent galaxy-galaxy mergers in regions of low galaxy density. Belsole et al. (2007) investigated the properties of the environment around 20 FR IIs at redshifts between 0.45 and 1 using *XMM-Newton* and *Chandra* observations, and found that 60% of the sources lie in X-ray emitting environments with luminosity larger than 10^{44} erg s^{-1}, a typical value of a rich cluster of galaxies. Ramos Almeida et al. (2013) presented a comparison between the environments of a complete sample of 46 southern RGs at intermediate redshifts ($0.05 < z < 0.7$), and found FR Is were consistent with clusters of Abell richness class 1, while for FR IIs they did not find any difference between the environment at high and low redshift.

More recently, it has been determined the role of different emission line class galaxies in the large-scale environment, since this dichotomy is directly linked to the accretion mode and host galaxy properties. Recent work has demonstrated fundamental differences between HERGs and LERGs (defined in Chapter 1) and show that these sources may have different relationships with

their environments. Gendre et al. (2013) determined a link between the excitation modes and the source environment, with HERGs found almost exclusively in low-density environments while LERGs were found in a wider range of densities. Ineson et al. (2015) performed the most detailed environmental characterization to date, studying the X-ray luminosity of the environments of two samples of radiogalaxies at different redshifts. These authors found no evolution for LERGs, while at low redshift HERGs inhabit poorer environments than at higher redshifts, and HERGs occupy groups and clusters with more compact central regions than the LERGs. Ching et al. (2017) performed an optical study of the environments of LERGs and HERGs in the redshift range $0.01 < z < 0.4$, finding that high-luminosity LERGs lie in dense environments and their clustering is connected to radio luminosity, while the environments of the HERGs and lower luminosity LERGs are indistinguishable from that of a matched control sample.

2.3 The large-scale environments of BL Lacs

Here I present a summary of the BL Lac environments literature, in chronological order up to date. Some studies were dedicated to particular objects, while in other cases the work was devoted to a sample of BL Lacs.

Back in the 90's, Stickel et al. (1991) selected a sample of 34 BL Lac objects and performed spectroscopic observations in some of their surrounding galaxies. They found three low-redshift ($z < 0.2$) BL Lacs that have one to three neighbouring galaxies at the same redshift, possibly indicating the presence of a group or cluster of galaxies. On the other hand, Romanishin (1992) presented optical imaging of 1E 1415.6+2557, an X-ray selected BL Lac at $z = 0.237$. Counting the number of galaxies in a radius of 0.6 Mpc from the BL Lac, the author did not find the field consistent with any galaxy enhancement, so the BL Lac should not be in a galaxy cluster. Fried et al. (1993) used the same sample of BL Lacs selected by Stickel et al. (1991) and performed an analysis of direct imaging data of the fields of BL Lac objects. By representing the galaxy surface density vs distance from the BL Lac (see Fig. 2.5) the authors observed a density increase towards the BL Lac corresponding to Abell richness classes 0 - 1.

The same year, Falomo et al. (1993a) published a study about the environment of the X-ray selected BL Lac H 0414+009 at $z = 0.287$. These authors plotted galaxy density as function of angular distance from the BL Lac, and observed an excess of galaxies at distances smaller than 0.5 Mpc. Moreover, analyzing the spectra of several objects around the BL Lac, the redshift of 3 galaxies was very similar to the giant galaxy hosting the BL Lac (see Fig. 2.6), therefore confirming the presence of a physical group. They concluded that H 0414+009 is in a moderately rich cluster (Abell class 0 - 1). These same authors presented a parallel study for the environment of the bright X-ray selected BL Lac PKS 2155-304 at $z = 0.116$ (Falomo et al., 1993b) . Again, an excess of galaxies was observed for this object at distances closer than 0.5 Mpc, which in this case would correspond to a poor cluster of galaxies, poorer than Abell richness class 0. In addition, using spectroscopic information these authors found 4 galaxies in the field at the same redshift as the BL Lac.

Wurtz et al. (1993) determined the clustering of five BL Lacs by means of the amplitude of the spatial covariance function within a 0.5 Mpc radius. These authors did not find any clustering around the source MS 0158+00 at $z = 0.298$, while the object MS 1207+39 at $z = 0.615$ was found at the center of a cluster of Abell richness 2. For H0414+009 these authors determined it is very likely near the center of an Abell richness class 1 cluster. Besides, the object MS 1407 + 59, at $z = 0.495$ was found to be at the center of cluster of Abell richness 1 - 2. These authors claimed the

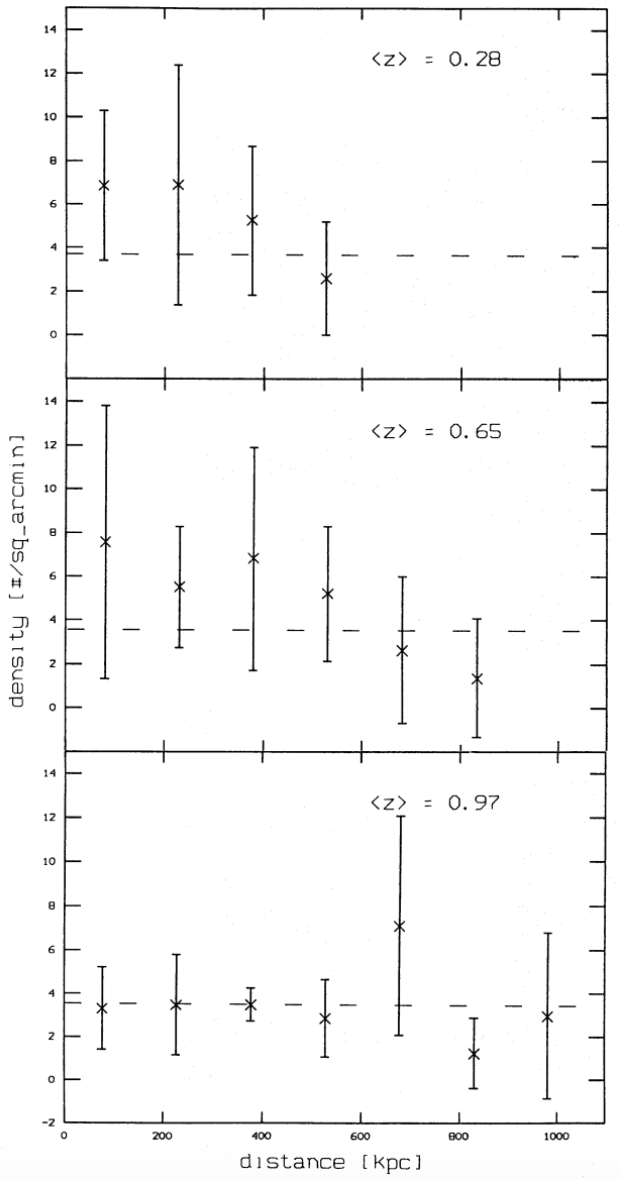

Figure 2.5: Galaxy surface density vs distance to the central BL Lac for 3 BL Lacs at different redshifts. The dashed line indicates the mean galaxy survey derived from the $< z > = 0.097$ subsample. The density increase observed corresponds to Abell richness class 0 - 1 (Fried et al., 1993).

richness of the cluster containing 3C 66A is Abell class 0, although this finding was based on the assumption of a redshift of $z = 0.444$ for this source, which is still uncertain.

Pesce et al. (1994) performed a multicolor photometric and spectroscopic analysis of galaxies in the fields of five BL Lacs: PKS 0829+046, H 1101-232, PKS 1400+162, PKS 1514-241 and PKS 2005-489. These authors did not find clear evidence that any of them belong to a cluster of galaxies. Nevertheless, a nearby galaxy was found at the same redshift as H 1101-232, and also two galaxies associated with PKS 2005-489. In Smith et al. (1995) the authors compared the megaparsec-scale environment of 17 BL Lacs with published redshifts $z < 0.4$ with those of FR I galaxies. The

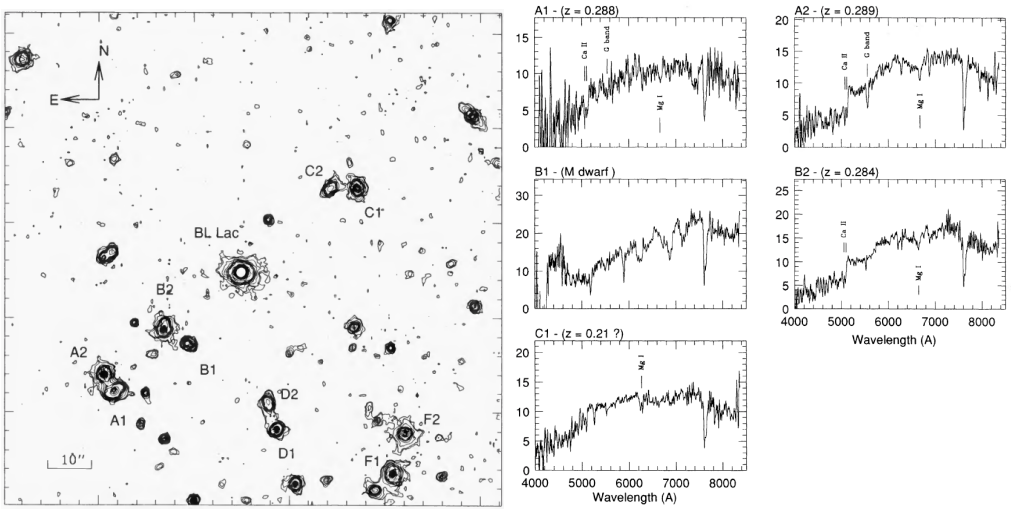

Figure 2.6: *Left:* Contour plot of the central part of the field around H 0414+009 and labels of the spectroscopically observed objects. *Right:* Spectra of some objects in the field of the BL Lac H 0414+009, 3 galaxies were found at its same redshift so they form a physical group (Falomo et al., 1993a).

results show a wide spread in the richness of the environments of BL Lacs, three of them (MS 0122.1+0903, MS 0158.5+0019 and MS 0607.9+7108) were found in very rich environments to at least Abell richness class 2. However, the rest of BL Lacs and the FR Is were all consistent with much poorer environments, which would correspond roughly to an Abell richness class 0. A Student's test revealed that BL Lac environments are consistent with those of the low-luminosity FR Is at the present epoch, finding a tendency of increasing richness of the clusters around BL Lacs at higher redshifts.

Falomo et al. (1995) continued with the study of single BL Lacs, this time PKS 0548-322 at the relatively low redshift $z = 0.069$. The distribution of galaxy density as a function of the distance within 0.5 Mpc corresponds to an environment of Abell richness 2. Moreover, five of the six galaxies for which spectroscopy was performed show a redshift close to that of the BL Lac, which indicates physical association. Moreover one of the nearby galaxies is in tidal interaction with the BL Lac host, see Fig. 2.7.

Pesce et al. (1995) presented a study showing large-scale environmental properties of a sample of 13 BL Lacs, evaluating the mean galaxy density of a large population of galaxies as a proxy of a non-clustered environment, calling it background. H 0323+022 at $z = 0.147$ was found with a local galaxy density significantly lower than the background mean galaxy density. For PKS 0521-365, a remarkable nearby BL Lac at $z = 0.05655$, galaxy counts were consistent with a cluster of Abell richness class 0. In addition the spectrum of a nearby galaxy was acquired, discovering it at the same redshift of PKS 0521-365. The BL Lac PKS 0548-322 was found to be in an cluster of Abell richness class 2 in a previous paper (Falomo et al., 1995), the observed spectra of several galaxies in the field confirmed these previous results. For objects with no available redshift (PKS 0048-097, PKS 0301-243, PKS 0422+004, PKS 0735+178, PKS 0754+100, PKS 0808+019 and MS 1402+042) these authors did not find any evidence for an excess of galaxies, except for PKS 0301-243. In this case they assumed for the analysis $z = 0.26$, a value that is now confirmed in the latest release of the Roma-BZCAT (Massaro et al., 2015a). Using this redshift they found a density enhancement of an Abell richness class 0 cluster, and the analysis of the spectra of two galaxies in its field finds them the

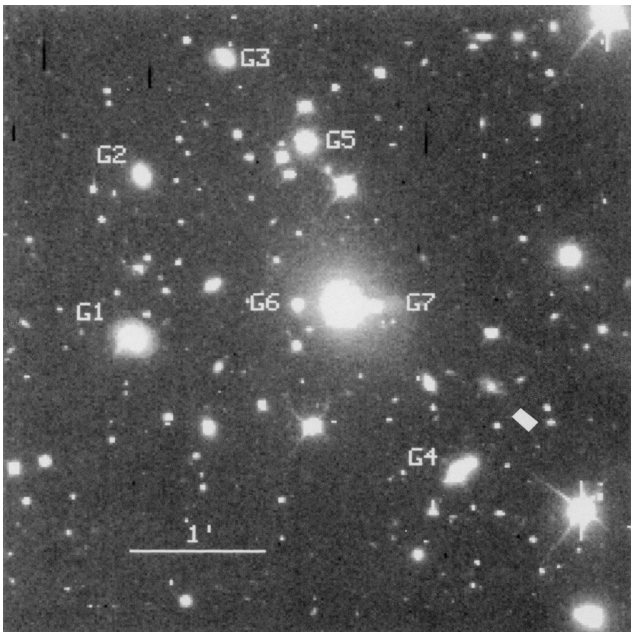

Figure 2.7: 5 × 5' image of the field of PKS 0548-322 and the galaxies extracted for spectroscopic analysis (Falomo et al., 1995).

same redshift. Two of the objects studied by these authors as BL Lacs are now classified differently: PKS 1034-293 is a quasar (Healey et al., 2007) and PKS 2335+031 a Seyfert 2 (Véron-Cetty & Véron, 2006).

The results presented by Owen et al. (1996) were based on the quantitative model predictions of Urry et al. (1991), that considered that for each FR I there should be a corresponding number of BL Lacs. They looked for emission associated with a BL Lac in a large sample of radiogalaxies in Abell clusters, finding none, which contradicts the predictions of the model.

Wurtz et al. (1997) applied the amplitude of the spatial correlation function in a radius of 0.5 Mpc to quantify the richness of the environments of a sample of 50 objects classified in one or more publications as a BL Lacs at $z < 0.65$. Only few BL Lacs appear to be in clusters as rich as Abell class 2 while most are consistent with Abell richness class < 0. These authors found several discrepancies with previous works. For MS 0122.1+0903, Smith et al. (1995) found a much higher value of the clustering and identified the Abell richness of the cluster as 1, while here the authors identified it as an Abell richness 0. The object MS 0158.5+0019 was observed by the same authors as the previous object, and again the Abell richness of the cluster found was 2, significantly higher than what was found by Wurtz et al., 0. For the BL Lac MS 0607.9+7108, Smith et al. (1995) found it in a cluster of Abell richness class 2, while Wurtz et al. did not find evidence for an excess above background galaxy counts. The Abell richness of MS1207+39 was found to be 0 by Wurtz et al. (1993), obtaining now a value lower than 0.

Gladders et al. (1997) presented the optical structure and local environment of 1E 1415.6+2557 at $z = 0.237$, an object previously studied by Romanishin (1992). These authors measured the richness of the environment using the amplitude of the spatial correlation function, and their results support Romanishin's claim, that the object is not in a cluster environment, but resides in a compact group or in a poor cluster of Abell richness 0 or less. Hardcastle et al. (1999) studied the X-ray emission of PKS 0521-365, a nearby BL Lac ($z = 0.05655$) for which Pesce et al. (1995) found it is

in cluster of Abell richness 0. They observed this BL Lac inhabits a cooling flow, this means that its environment is significantly different from those of the FR Is which tended to lie in less dense environments with much longer cooling times, see Fig. 2.8.

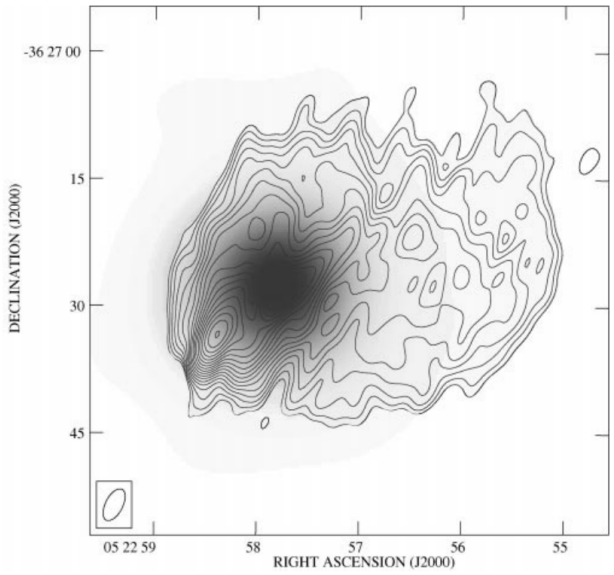

Figure 2.8: 1.4 GHz radio map of PKS 0521-365 overlaid on a smoothed X-ray image from *ROSAT* HRI (Hardcastle et al., 1999). This object inhabits a cooling flow, a different environment than a FR I.

Pesce et al. (2002) analysed images obtained with the *Hubble Space Telescope* WFPC2 and the F814W filter for a sample of nine BL Lacs at redshift between 0.19 and 0.997. These authors found that the environment for four of these objects tends to show a galaxy density enhancement over the background, while the other five seem to be isolated. Lietzen et al. (2008) studied the clustering environment of RGB 1745+398, this BL Lac at $z = 0.267$ and is in the center of a cluster with strong gravitational lensing, forming a blue arc. These authors measured the redshifts of five galaxies with optical spectroscopy, all of them were at the same distance of the BL Lac forming a physical cluster, see Fig. 2.9. The gravitational lensing was used for measuring a mass of $2.2 \cdot 10^{14} M_{\odot}$ inside a radius of 500 kpc, corresponding to at least 30 galaxies. This BL Lac therefore lies in a massive cluster of Abell richness class 1 or 2.

Abell 689 at z=0.279 is one of the most luminous clusters detected in X-rays. Giles et al. (2012) observed a bright point source at the center of the extended emission with *Chandra*. Cross-matching the X-ray peak emission position with SDSS, they found the point source spectrum to be similar to that of a BL Lac object at $z = 0.279$, consistent with the redshift previously assigned to the cluster.

The BL Lac PKS 0447-439 is one of the brightest High Energy (HE) γ-ray sources detected, but there is no spectroscopic redshift available for this source. Using multislit spectroscopy, Muriel et al. (2015) identified a group of galaxies of 7 members at $z = 0.343$ in the field of view of the BL Lac. These authors considered that since the probability of finding both a BL Lac and a group of galaxies of more than seven galaxies at the same position of the sky by chance is 3%, the BL Lac belongs to this group. Farina et al. (2016) performed a comprehensive study of PKS 2155-304, a prototype of X-ray selected BL Lac object at $z = 0.116$. Using both multi-object spectroscopy and overdensity to study the large-scale environment, these authors concluded that this source resides in a small cluster/group with an Abell richness class < 0, in agreement with previous results by

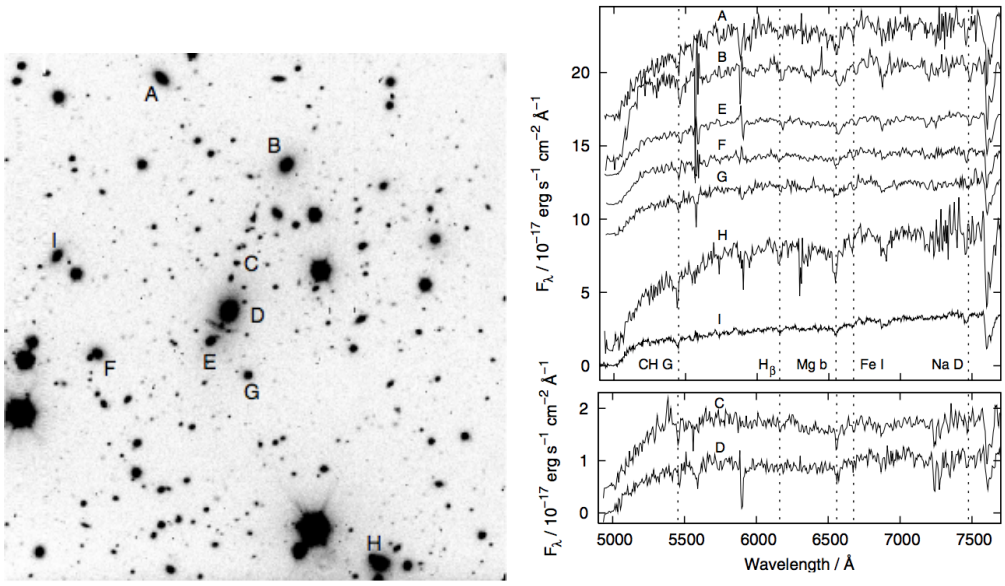

Figure 2.9: *Left:* A field of size 207 × 218" of RGB 1745+398 obtained with the Nordic Optical Telescope (NOT). The galaxy D is the central brightest galaxy of the cluster harbouring the BL Lac nucleus. *Right:* Spectra of the 5 galaxies in the field of the BL Lac RGB 1745+398. They are at the same redshift and belong to the same cluster (Lietzen et al., 2008).

Falomo et al. (1993b) and Wurtz et al. (1997). The same method used by Muriel et al. (2015) was applied by Rovero et al. (2016) to the unknown redshift BL Lac PKS 1424+240. Performing optical spectroscopic observations of thirty objects in its field of view and using spectroscopic information from the SDSS, these authors found a new group of galaxies with eight members at $z = 0.601$ (see Fig. 2.10). The probability of PKS 1424+240 being a member of this group was found to be 98%.

Muriel (2016) cross-correlated a catalog of groups of galaxies from the SDSS with the 5-th edition of the Roma-BZCAT finding 121 matches, 24 of them BL Lac. Due to incompleteness as a function of redshift that the friends-of-friend(FOF) algorithm used for their group catalog, this author restricted the analysis to BL Lacs at $z \leq 0.2$. He found $\sim$ 32% of the BL Lacs to be associated to single galaxies, while $\sim$43% were found in groups of three or more members. He estimated a correction factor that takes into account the incompleteness of the group catalog, and applying it to their sample he concluded that amount of BL Lacs in groups is higher than a 67%, although this results corresponds mainly to the galaxy dominated BL Lacs.

Most of these studies are based on photometric data only, and evidence for a rich environment is inferred from the increase number counts of sources in the proximity of BL Lacs. Only for a handful of objects the physical association of nearby sources has been further confirmed via dedicated spectroscopic observations. The results of BL Lacs environment studies are ambiguous, with some studies confirming the similarities of the environments of BL Lacs and FR Is, while others claim the opposite. In Table 2.2 is presented a summary of all the BL Lacs studied up to date, the type of their environment and the bibliography. To this date, however, there has been no systematic study of the clustering of galaxies around BL Lacs for unbiased samples.

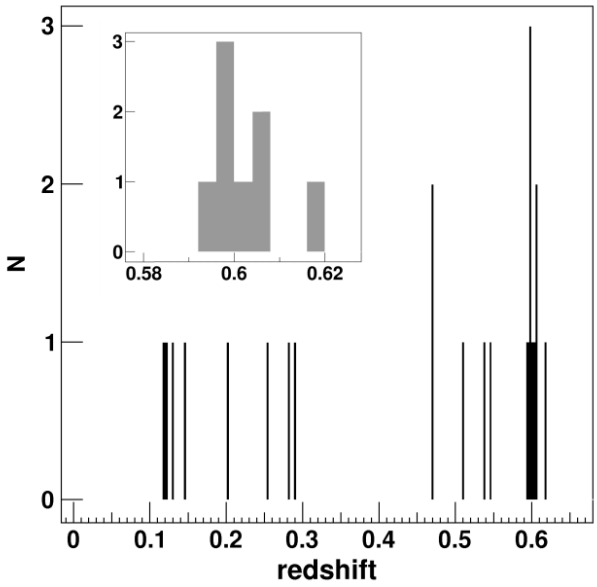

Figure 2.10: Distribution of redshifts for the galaxies observed in the field of view around PKS 1424+240. A narrow range is observed around the the redshift of the cluster $z = 0.601$ (Rovero et al., 2016).

2.4 Open questions and scientific objectives

According to the Unification Scenario of radio loud AGNs, RGs are the parent population of blazars, and in particular FR Is seen through their jets appear as BL Lacs. Despite the wide acceptance of the Unification Scenario, one of the observational test proposed by Urry & Padovani (1995) has not been profoundly studied yet. As shown in the previous section there is still not a complete, systematic study of the large-scale environments of BL Lacs. The investigations have been carried out using small samples or single objects, and results are controversial, with some authors claiming that BL Lacs reside in clusters and others concluding the opposite.

There are three possible scenarios expected from the systematic study of the large-scale environments of BL Lacs and its comparison with those of FR I RGs:

1. **BL Lacs and FR I RGS are hosted in similar environments (poor clusters).** One of the main difficulties in the study of BL Lacs is that in many cases it is not possible to measure any redshift because of lacking features in their optical spectra. In fact the redshift its only known for ~ 30 % of them. If BL Lacs were confirmed to be in clusters, it would be possible to measure the redshift of the galaxies in the cluster and hence estimate the distance to the BL Lac.

2. **BL Lacs are isolated.** This result would be challenging for the Unification Model since FR Is would not be directly the parent population of BL Lacs. This result would also distress the model of hierarchical clustering of cosmological structures, to have such huge objects growing outside of the cosmic web.

3. **BL Lacs are in rich environments different from those of FR I RGs.** In this case, we would have both of the previous outcomes, that is, we would be able to measure the redshift of featureless BL Lacs by measuring the redshift of galaxies belonging to the cluster, and at

Table 2.2: BL Lacs studied in the literature.

BL Lac name	Roma-BZCAT name	z	Literature?	In a cluster	Type of cluster
PKS 0048-097	5BZB J0050-0929	?	Pesce et al. (1995)	No	-
MS 0122.1+0903	5BZB J0124+0918	0.338	Smith et al. (1995) \Wurtz et al. (1997)	Yes \Yes	Abell class 2 \Much less dense cluster
MS 0158.5+0019	5BZB J0201+0034	0.298	Wurtz et al. (1993) \Smith et al. (1995) \Wurtz et al. (1997)	No \Yes \Yes	- \Abell class 2 \Much less dense cluster
MS 0205.7+3509	5BZB J0208+3523	0.318	Smith et al. (1995)	Yes	Abell class 0
3C66A	5BZB J0222+4302	?	Wurtz et al. (1993) \Wurtz et al. (1997)	Yes \Yes	Abell class 0 \Abell class <0
MS 0257.9+3429	5BZB J0301+3441	0.246	Smith et al. (1995) \Wurtz et al. (1997)	No \No	- \Void
PKS 0301-243	5BZB J0303-2407	0.266	Pesce et al. (1995)	Yes	Abell class 0
MS 0317.0+1834	5BZG J0319+1845	0.19	Smith et al. (1995) \Pesce et al. (1995) \Wurtz et al. (1997)	Yes \No \No	Abell class 0 \Void \Void
1ES 0323+022	5BZB J0326+0225	0.147	Smith et al. (1995) \Wurtz et al. (1997)	Yes \No	Abell class 0 \-
H 0414+009	5BZB J0416+0105	0.287	Falomo et al. (1993a) \Wurtz et al. (1993) \Wurtz et al. (1997)	Yes \Yes \Yes	Abell class 0 - 1 \Abell class 1 \Abell class 1
PKS B0422+004	5BZB J0424+0036	?	Pesce et al. (1995)	No	-
PKS 0447-439	5BZB J0449-4350	?	Muriel et al. (2015)	Yes	Group of 7 galaxies
PKS B0521-365	5BZU J0522-3627	0.05655	Pesce et al. (1995) \Wurtz et al. (1997)	Yes \No	Abell class 0 \-
PKS 0548-322	5BZG J0550-3216	0.069	Falomo et al. (1995) \Pesce et al. (1995) \Wurtz et al. (1997)	Yes \Yes \Yes	Abell class 2 \Abell class 2 2 \Abell class 2
MS 0607.9+7108	5BZB J0613+7107	0.267	Smith et al. (1995) \Wurtz et al. (1997)	Yes \No	Abell class 2 \-
PKS B0735+178	5BZB J0738+1742	> 0.424	Pesce et al. (1995)	No	-
MS 0737.9+7441	5BZB J0744+7433	0.314	Smith et al. (1995)	No	-
PKS 0754+100	5BZB J0757+0956	0.266	Pesce et al. (1995)	Yes	Abell class <0
PKS 0808+019	5BZB J0811+0146	1.148	Pesce et al. (1995)	No conclusions	-
S4 0814+42	5BZB J0818+4222	0.53	Smith et al. (1995) \Pesce et al. (2002)	No \No	-\-
PKS 0818-128	5BZB J0820-1258	?	Pesce et al. (1995)	No conclusions	-
PKS 0823+033	5BZB J0825+0309	0.506	Wurtz et al. (1997)	Yes	Abell class 0
PKS 0829+046	5BZB J0831+0429	0.174	Pesce et al. (1994)	No	-
S4 0828+49	5BZB J0832+4913	?	Wurtz et al. (1997) \Pesce et al. (2002)	No \No	Void \-
S4 0954+65	5BZB J0958+6533	0.367	Wurtz et al. (1997)	No	-
PKS 1034-293	5BZQ J1037-2934	0.312	Pesce et al. (1995)	No	-
H 1101-232	5BZB J1103-2329	0.186	Pesce et al. (1994)	No	-
MS 1207.9+3945	5BZB J1210+3929	0.617	Wurtz et al. (1993) \Wurtz et al. (1997)	Yes \Yes	Abell class 2 \Abell class 1 - 2
S3 1219+28	5BZB J1221+2813	0.102	Wurtz et al. (1997)	No	-
MS 1221.8+2452	5BZB J1224+2436	0.218	Wurtz et al. (1997) \Pesce et al. (2002)	No \No	Void \-
MS 1229.2+6430	5BZB J1231+6414	0.164	Wurtz et al. (1997)	Yes	Abell class < 0
MS 1235.4+6315	5BZB J1237+6258	0.297	Wurtz et al. (1997)	No	Void
B2 1308+32	5BZU J1310+3220	0.996	Pesce et al. (2002)	No	-
PKS 1400+162	5BZB J1402+1559	0.244	Pesce et al. (1994) \Wurtz et al. (1997)	No \No	-\-
MS 1402.3+0416	5BZB J1404+0402	0.344	Pesce et al. (1995) \Wurtz et al. (1997)	No \No	- \Void
MS 1407.9+5954	5BZB J1409+5939	0.495	Wurtz et al. (1993) \Wurtz et al. (1997) \Pesce et al. (2002)	Yes \Yes \Yes	Abell class 1-2 \Abell class 1 \Galaxy enhancement
PKS 1413+135	5BZU J1415+1320	0.247	Wurtz et al. (1997)	No	In a void
1E 1415.6+2557	5BZB J1417+2543	0.237	Romanishin (1992) \Wurtz et al. (1997) \Gladders et al. (1997)	No \No \Yes	-\- \Abell class < 0
PG 1418+546	5BZB J1419+5423	0.153	Wurtz et al. (1997)	No	In a void
PKS 1424+240	5BZB J1427+2348	?	Rovero et al. (2016)	Yes	Group of 8 galaxies
MS 1443.5+6349	5BZG J1444+6336	0.299	Wurtz et al. (1997)	No	Void
MS 1458.8+2249	5BZB J1501+2238	?	Wurtz et al. (1997)	No	-
PKS 1514-24	5BZB J1517-2422	0.048	Pesce et al. (1994)	No	-
MS 1534.2+0148	5BZB J1536+0138	0.312	Wurtz et al. (1997)	Yes	Abell class < 0
PKS 1538+149	5BZB J1540+1447	0.605	Wurtz et al. (1997) \Pesce et al. (2002)	Yes \Yes	Abell class \Enhancement above background
1ES 1552+203	5BZB J1554+2011	0.222	Wurtz et al. (1997)	No	-
Mrk 501	5BZB J1653+3945	0.033	Wurtz et al. (1997)	No	-
H 1722+119	5BZB J1725+1152	?	Wurtz et al. (1997)	No	Void
1ES 1727+502	5BZB J1728+5013	0.055	Wurtz et al. (1997)	No	-
RGB 1745+398	5BZG J1745+3951	0.267	Lietzen et al. (2008)	Yes	Abell class 1-2
PKS 1749+096	5BZB J1751+0939	0.322	Wurtz et al. (1997)	No	Void
MS 1757.7+7034	5BZB J1757+7033	0.407	Wurtz et al. (1997)	No	-
4C +69.24	5BZB J1806+6949	0.050	Wurtz et al. (1997)	Yes	Abell class 0
4C +56.27	5BZB J1824+5651	0.663	Pesce et al. (2002)	Yes	Enhancement above background
PKS B1921-293	5BZQ J1924-2914	0.352	Wurtz et al. (1997)	Yes	Abell class 0
S5 2007+77	5BZB J2005+7752	0.342	Wurtz et al. (1997)	No	Void
PKS 2005-489	5BZB J2009-4849	0.071	Pesce et al. (1994)	No	-
MS 2143.4+0704	5BZB J2145+0719	0.237	Smith et al. (1995) \Wurtz et al. (1997) \Pesce et al. (2002)	No \No \Yes	- \- \Enhancement above background
PKS 2155-304	5BZB J2158-3013	0.116	Falomo et al. (1993b) \Wurtz et al. (1997) \Farina et al. (2016)	Yes \No \Yes	Abell class < 0 \- \Abell class < 0
S4 2200+42	5BZB J2202+4216	0.0686	Smith et al. (1995) \Wurtz et al. (1997)	Yes \Yes	Abell class 0 \Abell class < 0
4C +04.77	5BZU J2204+0440	0.027	Smith et al. (1995) \Wurtz et al. (1997)	No \No	-\-
PKS 2254+074	5BZB J2257+0743	0.19	Smith et al. (1995) \Wurtz et al. (1997)	Yes \No	Abell class 0 \-
MS 2347.4+1924	5BZU J2350+1941	0.515	Smith et al. (1995)	No	-

Column description. (1): BL Lac name, (2): BL Lac name in the Roma-BZCAT v.5, (3): redshift, (4): reference, (5) is the BL Lac in a cluster yes/no, (6) if in a cluster type of cluster.

the same time the Unification Model would need to be revised, since possibly FR Is would no longer be the parent population of BL Lacs.

CHAPTER 3

Clustering analysis

With the increasing number of big datasets in astronomy, automated classification has become crucial. The collection of methods to classify objects in very large datasets and to search for patterns is called "data mining". Its development is very recent and one of the analysis that data mining can focus on is clustering, which is partitioning a data set into subgroups (clusters) so that data into each cluster share some common characteristics. Clustering analysis has played an important role for a long time in a wide variety of fields such as biology, psychology, marketing, business or astronomy. The reason is that it has many applications in the analysis of practical problems since its methods are essential when the dimension and/or size of the datasets are too high to be analysed individually.

When the training data includes both the input and the desired final results it is called supervised clustering, these methods are fast and accurate. However, if the final results are unknown it is called unsupervised clustering and it can be used to organize the input data in classes only on the basis of their statistical properties. The results are often uncertain and highly dependent on the mathematical procedure chosen for the calculation, such as distance measure chosen, initial parameters, the dataset, etc. Different methods can and do generate different solutions because of the different statistical methods applied in each one of them. Besides, the final results can vary from one method to another, since they are different regarding sensitivity to the initial parameters, shape of the cluster, etc. In the present work results a priori are unknown so unsupervised clustering will be used for spatial data analysis.

Clustering algorithms are divided according to their data treatment in:

- **Exclusive vs Overlapping vs Fuzzy.** Exclusive is when each object is assigned to a single cluster. There are situations in which a point can be placed in more than one cluster: overlapping clustering is used to reflect the fact that an object can simultaneously belong to more than one cluster, while fuzzy clustering assigns to each object a probability from 0 to 1 of belonging to one or several clusters.

- **Complete vs Partial.** A complete clustering assigns every object to a cluster, while partial

clustering takes into account that the data-set might not be well defined, so not every object must belong to a cluster due to the presence of noise and/or outliers.

Clustering aims to find useful groups of objects, where usefulness is defined by the goals of the data analysis. The major clustering methods are the following:

- **Partitioning algorithms.** They minimize a given clustering criterion by iteratively relocating data points between clusters until a locally optimal partition is attained.
- **Hierarchical algorithms.** Finds successive clusters using previously stablished clusters. They can be agglomerative (bottom-up) or divisive (top-down). Hierarchical methods are commonly used to find groupings in multivariate data without any parametric assumptions.
- **Density-based.** Defines a cluster as a dense region of objects that is surrounded by a low density region. This methodology is often employed when there are noise and outliers. Density-based clustering requires a distance metric between points and works well on high dimensional data and on irregular clusters.
- **Grid-based.** Two objects are connected only if they are within a specified distance of each other. This implies that each object is closer to some other object in the cluster than to any point in a different cluster. This definition is useful when clusters are irregular or intertwined but can have trouble if noise is present.
- **Model-based.** A model is hypothesized for each of the clusters and the idea is to find the best fit of that model to each other.

In this work the large-scale environment of galaxies is analyzed looking for clusters in a circular region of certain radius surrounding FR Is and BL Lacs, combining several clustering methods to avoid the individual problems related to each one of them, hence to validate of the procedures success in achieving correct classifications and avoid misclassifications.

3.1 Gnomonic projection

To perform a clustering algorithm it is crucial to choose a metric defining the distances between two objects and the simplest metric to use is the Euclidean distance, based on standarized variables. To be able to use Euclidean distances between celestial objects in the algorithms, I make use of the gnomonic projection that converts angular to Euclidean distances. The gnomonic projection is a nonconformal map projection obtained by projecting the point P_1 (or P_2) on the surface of sphere from a sphere's center O to point P in a plane that is tangent to a point S (see Fig. 3.1). Its most important property is that every geodesic including the equator and all meridians is mapped to a straight line, so the Euclidean distance is correspondent to the angular separation in the clustering algorithm.

The gnomonic projection is applied to every source in each field of the data set. It changes the coordinates from right ascension and declination $RAJ2000$ and $DEJ2000$ to X and Y, being the position of the central source in each field $(X, Y) = (0, 0)$ and the gnomonic coordinates of each source in the same field are obtained using the following transformation:

$$\begin{aligned} X =& \frac{cos(DEJ2000) \cdot sin(RAJ2000 - ra)}{cos(dec) \cdot cos(DEJ2000) \cdot cos(RAJ2000 - ra) + sin(dec) \cdot sin(DEJ2000)} \\ Y =& \frac{cos(dec) \cdot sin(DEJ2000) - cos(DEJ2000) \cdot sin(dec) \cdot cos(RAJ2000 - ra)}{sin(dec) \cdot sin(DEJ2000) + cos(dec) \cdot cos(DEJ2000) \cdot cos(RAJ2000 - ra)} \end{aligned} \tag{3.1}$$

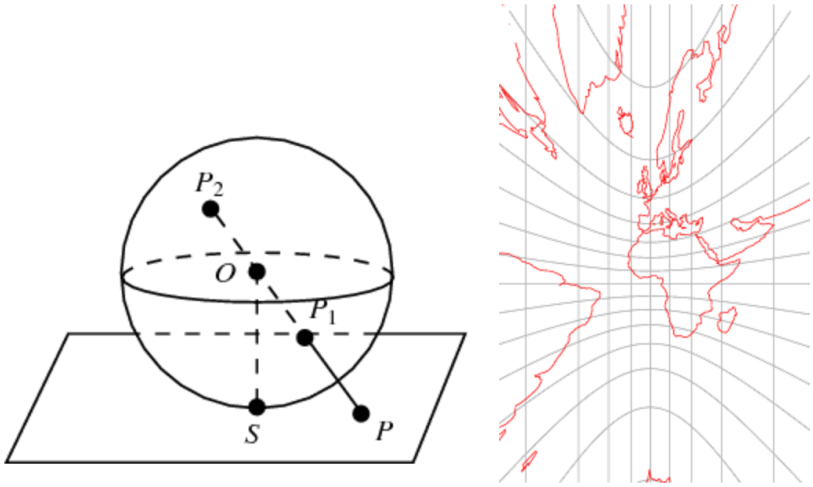

Figure 3.1: *Left:* Schematic representation on the conformation of gnomonic projection. *Right:* Gnomonic projection of a partial map of the Earth.

Being:

$(RAJ2000, DEJ2000)$ the coordinates of the field source in the standard epoch $J2000.0$.

(ra, dec) the coordinates of the central source in the standard epoch $J2000.0$.

By doing this transformation, the distance between two points P_1 and P_2 in the sky can be calculated using the Euclidean metric:

$$D = \sqrt{(X_2 - X_1)^2 + (Y_2 - Y_1)^2} \tag{3.2}$$

The amount of scalar distortion for polar aspect increases with the distance from the center, for a distance of 15^o from the center, there is a distortion of 7.2% in the meridians and 3.5% in the latitude. The fields of view however are rarely bigger than a few degrees, so this effect is negligible.

3.2 Clustering algorithms

There is a great number of different clustering methods. For the purposes of this work, several complementary methods have been chosen according to their specific conditions to be optimal for the analysis of the data set, also these methods have previously proven to be useful in astronomy.

3.2.1 DBSCAN + OPTICS

DBSCAN comes from Density Based Spatial Clustering of Applications with Noises and it is a partitional density-based clustering algorithm first developed by Ester et al. (1996). It locates regions of high density (clusters) that are separated from each other by regions of low density (noise). There are several methods to describe density, and DBSCAN uses the center-based approach. Density is estimated for a particular object in the data set by counting the number of objects within a specific radius, including the object itself. The density of any point depends on the radius chosen, and a cluster is defined as a maximal set of density-connected points. Points in low-density regions are considered as noise and omitted, which means DBSCAN produces a partial clustering.

The local density for a point p is defined by two parameters:

- $\boldsymbol{\varepsilon}$: radius for the neighbourhood of point p.
- ***MinPts***: minimum number of points inside the given radius ε.

High density is considered as a ε-neighbour of an object that contains at least $MinPts$, see Fig. 3.2. Both parameters are specified by the user.

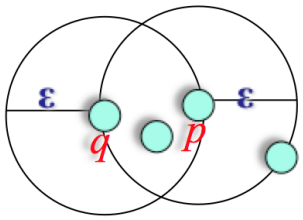

Figure 3.2: If $MinPts$ =4, density of p is high and density of q is low.

Given ε and $MinPts$, it is possible to categorize the objects into three groups, see Fig. 3.3:

- **Core points:** Inside a dense region, a point is a core point if the number of points within a radius ε exceeds a certain threshold, $MinPts$. Any two core points that are within a distance ε from each other are considered in the same cluster.
- **Border points:** Located on the edge of a dense region. A border point can fall within the neighbourhoods of several core points.
- **Noise points:** Any point that is neither a core point not a border point. Noise points are discarded.

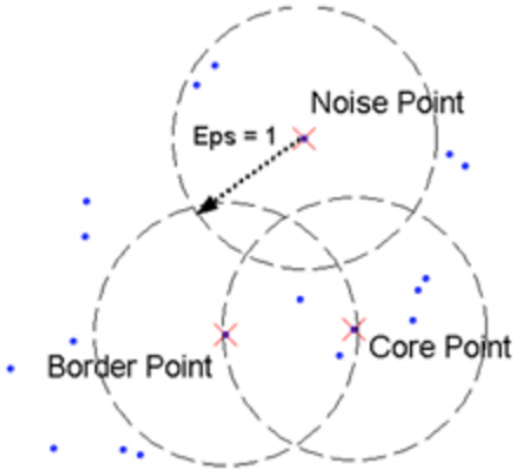

Figure 3.3: DBSCAN classification of points if $MinPts = 4$.

In density-based clustering, two points are considered to be on the same cluster if they are both density reachable and density connected, see Fig. 3.4:

- **Density reachable:** A point p is density-reachable from a point q within a radius r if there is a chain of points $p_1, ..., p_n$, $p_1 = q$, $p_n = p$ such that p_{i+1} is in the cluster defined by p_i.

Density-reachability is asymmetric, a point q can be density-reachable from a point p and it is possible that p is not density-reachable from q.

- **Density-connected:** A point p is density-connected to a point q within a radius r if there is a point o such that both, p and q are density reachable from o within r. Density-connectivity is symmetric.

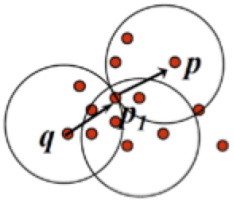

(a) density reachable

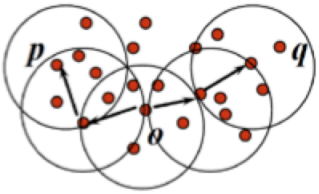

(b) density connected

Basic DBSCAN algorithm:

1. Arbitrarily select a point p.
2. Retrieve all $MinPts$ points density-reachable from p within ε.
3. If p is a core point, a cluster is formed.
4. If p is a border point, no points are density-reachable from p and DBSCAN goes to the next point of the database.
5. Continue the process until all of the points have been processed.

The strengths of DBSCAN are that since it is a density-based clustering algorithm, it is relatively resistant to noise, it is able to find clusters of arbitrary shapes and sizes, it is less vulnerable than hierarchical clustering algorithms to accidental chaining of clusters by intervening points and it is computationally efficient with O(n log n) operations. However, this algorithm has problems when the clusters have varying densities. The main problem is its strong dependance on the initial parameters ε and $MinPts$, and they are difficult to dictate automatically. Determining the initial parameters ε and $MinPts$ is critical for the correct behaviour of the algorithm; if $MinPts$ is too small then even a small number of closely spaced points that are noise or outliers will be incorrectly labeled as clusters, but if $MinPts$ is too large then small clusters are likely to be labeled as noise.

To determine automatically the initial parameters as a previous step before DBSCAN, the algorithm OPTICS is applied. OPTICS comes from Ordering Points To Identify the Clustering Structure, and it is a density-based hierarchical clustering method that addresses the DBSCAN problem of detecting meaningful clusters of varying density (Ankerst et al., 1999). OPTICS can be seen as a generalization of DBSCAN, that replaces the ε parameter with a maximum value that mostly affects performance, then $MinPts$ essentially becomes the minimum cluster size to find. OPTICS does not produce clusters explicitly, but rather generates an ordering of data objects representing density-based clustering structure.

The main difference with DBSCAN is that OPTICS produces similar results for a big range of the initial parameters, the algorithm is relatively insensitive to parameter settings. Similarly to DBSCAN, the local density at a point is defined by two parameters and it produces good results if the following two parameters are just "large enough" (see Fig. 3.5):

- ε: generating distance, it is the largest distance considered for clusters.
- ***MinPts***: minimum cluster size.

The algorithm generates the distance parameters:

- **Core distance of a point** p: the distance ε' between the point p and its $MinPts$-th neighbour.
- **Reachability distance of an object** p **with respect to another object** o: is the smallest distance such that p is directly density reachable from o if o is a core object.

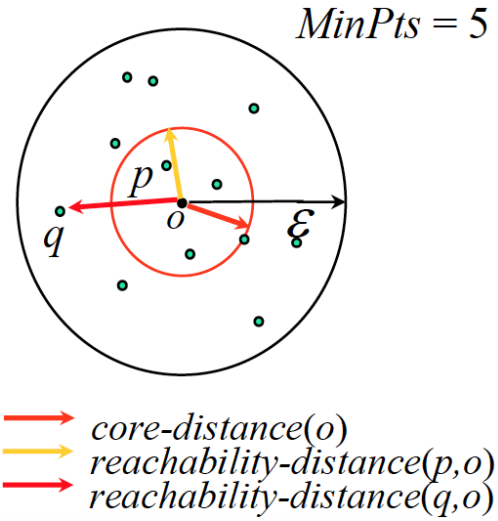

Figure 3.5: OPTICS core and reachability distances being $MinPts = 5$.

OPTICS computes an ordering of all objects in a given database and stores the core-distance and the reachability-distance for each one, it maintains a list called *OrderSeed* to generate the output ordering. Objects in *OrderSeed* are sorted by the reachability-distance from their respective closest core, which is the smallest reachability-distance.

Basic OPTICS algorithm:

1. Begin with an arbitrary object from the input database p.
2. Retrieves the ε-neighbour of p, determines the core-distance and sets the reachability distance to undefined.
3. The object p then is written to output.
4. If p is not a core object then it moves to the next object in the *OrderSeeds*.

5. If p is a core object then for each object q in the ε-neighbour of p, q's reachability-distance is updated and inserts q into *OrderSeeds* if q has not yet been processed.

6. Continue the process until the input is fully consumed and *OrderSeeds* is empty.

The cluster-ordering of the data set can be represented by a "reachability plot", that helps visualizing the clustering structure. A "reachability plot" is a bar chart that shows each object's reachability distance in the order the object was processed. Since points belonging to a cluster have a low reachability distance to their nearest neighbour, the clusters show up as valleys in the reachability plot, the deeper the valley, the denser the cluster, while large bars in the plot represent noise, as seen in Fig. 3.6. The generating distance ε must be chosen high enough because it influences the number of levels in the reachability plot: the smaller ε, the more objects have an undefined reachability distance, so low density clusters might be lost. A reachability plot for a data set is not unique, using different starting points will lead to different reachability plots, but representing the same clustering structure.

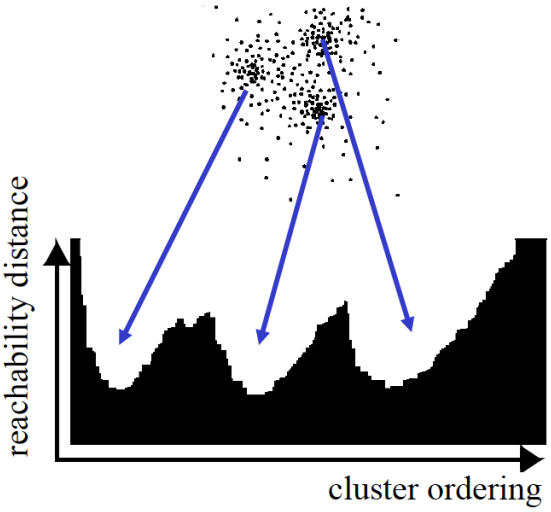

Figure 3.6: Example of clusters represented in a reachability plot. Clusters correspond to valleys and noise is represented by large bars.

In this work the algorithm OPTICS is adopted as a pre-procesing for selecting DBSCAN initial parameters. Since clusters are represented as valleys in the reachability plot, the task of automatic cluster extraction is to identify significant valleys, the initial parameters for DBSCAN are automatically extracted by defining an horizontal cut in the dendogram built with the function *optics* from the R package "dbscan" (Hahsler & Piekenbrock, 2017). The significance of a separation between regions is determined by the ratio between the height of a local maximum in the reachability plot and that of the regions to the left and to the right of that local maximum. To consider a local maximum as a cluster separation this ratio is set to 0.75, i.e., the average reachability value to the left and to the right must be smaller than 0.75 times the value of the local maximum (Sander et al., 2003). All the values of the reachability distance for these local maxima are collected, and I select as an starting ε value for DBSCAN the mean of 0.75 $\times$ all local maxima. The value $MinPts$ chosen

for DBSCAN is 5, the minimum value in OPTICS to smoothen the "reachability plot" since for lower values it looks jagged. Then the DBSCAN algorithm is applied to locate the clusters using the function *dbscan* from the R package "dbscan".

Outline OPTICS + DBSCAN:

1. Apply the OPTICS algorithm using the initial parameters:

$$MinPts = 5$$
$$\varepsilon = \sqrt{\frac{d^2 \times MinPts}{N}} \tag{3.3}$$

   being d the distance between two points in the data set, and N the total number of points in the dataset.

2. Obtain the reachability plot and identify the local maxima. A point p is a local maxima if:

$$height(p) > 0.75\times < height(p) - height(MinPts) > \rightarrow \textit{at its right and left} \tag{3.4}$$

3. Set an horizontal cut in the reachability plot:

$$\varepsilon' = \textit{mean (}0.75 \times \textit{height all local maxima)}$$

4. Apply the DBSCAN algorithm to obtain the clusters using the initial parameters:

$$\textit{MinPts'=5}$$
$$\varepsilon\textit{' obtained in the previous step}$$

3.2.2 Voronoi Tesselation

Given a set of n points in the space, a Voronoi Tessellation diagram (Voronoi, 1908) is a non-arbitrary and non-parametric subdivision of the space into n cells, one for each point p, with the property that every cell contains an original point and all positions in each area are closer to its point than any other, as seen in the left panel of Fig. 3.7. The line segments of the Voronoi diagram are all the points in the plane that are equidistant to the two nearest sites. The Voronoi vertices or nodes are the points equidistant to three sites. The Voronoi diagram of a set of points is dual to its Delaunay triangulation (Lejeune Dirichlet, 1850), that is obtained by linking its nodes, see right panel of Fig. 3.7. The area of each Voronoi cell is inversely proportional to the density of sources in the neighbourhood, thus smaller areas correspond to regions of higher source density. To compute clusters using this algorithm, it is necessary to identify the areas with high source density.

Basic Voronoi Tesselation algorithm:

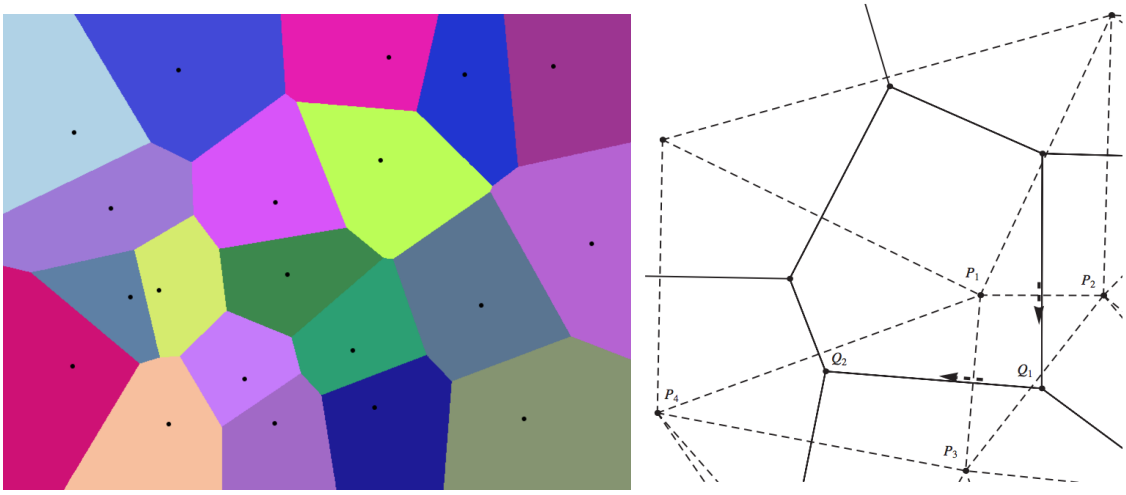

Figure 3.7: *Left:* basic Voronoi diagram. *Right:* Illustration of the Voronoi diagram (solid lines) and its dual Delaunay triangulation (dashed lines). For each generator set P_i, there is one and only one set of Voronoi cells given by the vertices Q_i.

1. Starting from a point P_1 identify its nearest neighbour P_2 and make the perpendicular bisector between these two points.
2. Stop when reach for a point Q_1 equidistant from P_1, P_2 and any third point P_3.
3. Again make a perpendicular bisector between P_1 and P_3 until the point Q_2 equidistant to P_1, P_3 and P_4 is reached.
4. Successive repetition of this process will eventually bring us back to Q_1 after a finite number of steps.
5. The set of points Q_i are the vertices of a polygon, the Voronoi cell, associated with P_i. This process is repeated for all the n points until the Voronoi Tesselation diagram is complete.

To find clusters in the data set, regions of high source density needed to be identified. The first step was to apply the Basic Voronoi Tesselation algorithm previously described to the n-size dataset in the determined circular region using the function *deldir* from the R package "deldir" (Turner, 2016) and compute all the normalized areas for each polygon. Afterwards, 100 simulations were performed for n-sources uniformly distributed in that same plane of the sky. To this simulations I applied the basic Voronoi Tesselation algorithm and computed all their normalized areas. Then I calculated the 95% quantile of all the areas in the simulations as a threshold for high density regions. A cluster is considered a number of contiguous points higher than 4 and whose polygon areas are smaller than that 5% threshold.

The advantage of this method is that it is independent of cluster shape, but the main drawback is that it cannot find clusters by itself and a significance threshold needs to be set by the user.

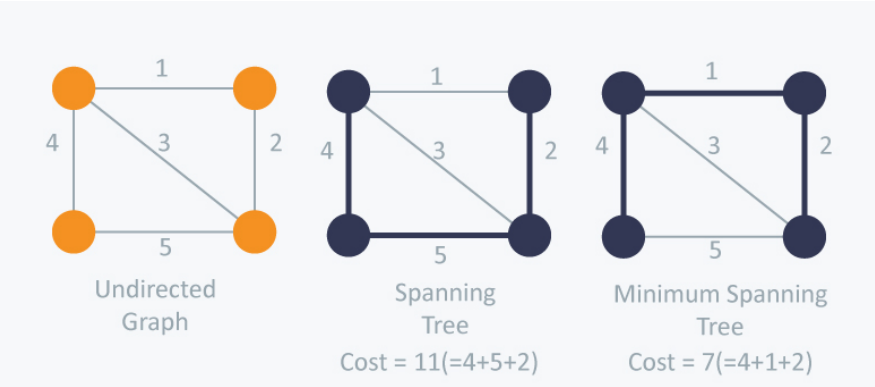

Figure 3.8: The graph on the left shows a set of points that are connected to each other, and a value for the edge weight has been given for each connection. The central illustration shows a spanning tree, where the graph is connecting all the points with as less lines as possible. The graph in the right is the minimum spanning tree in which the sum of weights is minimum.

3.2.3 Minimum Spanning Tree

The Minimum Spanning Tree (MST) is a hierarchical clustering method. In graph theory, a spanning tree of a given a set of p_n points in the space is the subgraph that is a tree and includes all the n points of a data set, with a minimum possible number of edges or lines. The minimum spanning tree is the spanning tree whose lengths of the lines connecting points is as small as possible, as seen in Fig. 3.8.

The main advantage of this method is its simplicity to understand and compute, however it does not behave well with noise since it tends to build unphysical elongated chains. There is a variety of computational algorithms for constructing the MST that goes back to the 20's; here I use that of Campana et al. (2008) where this method was developed for γ-ray source detection.

Basic MST algorithm:

1. Begin with an arbitrary object p from the input database.
2. Find the nearest neighbour and connect this two points: this is the first edge of the MST.
3. Find the nearest point to any point that is already connected in the MST.
4. After $n-1$ iterations being n the total number of points, the complete MST is built.

Once the MST is found, it is necessary to do a parameter selection to extract the clusters in a high density region. The primary selection is to set a limit on the edge length $\lambda < \Lambda_m$, where Λ_m is the mean length for a random-field MST and can be written as:

$$\Lambda_m = 0.65\sqrt{\frac{A}{N_{tot}}} \tag{3.5}$$

Being A the field area and N_{tot} the total number of points.

A secondary selection is performed to avoid satellite clusters, a primary selection artefact usually located in the surroundings of a true big cluster. To do so it is necessary to compute the cluster

parameter magnitude M_k, defined as:

$$M_k = n_k g_k \tag{3.6}$$

That combines the number of nodes n_k with their clustering degree:

$$g_k = \frac{\Lambda_m}{\lambda_{m,k}} \tag{3.7}$$

Where Λ_m is the mean length for a random-field MST previously defined, and $\lambda_{m,k}$ is the mean of the edge lengths in the k-th cluster.

Clusters in the dataset were selected with the MST algorithm using the following procedure: I first began with a mock sample of thousands of different sky random fields at different redshifts. I applied the MST algorithm to find the MST for each one of the fields, and made the primary selection on the edge length $\lambda < \Lambda_m$. For each redshift interval, I calculated the distribution of the parameter M_k of the spurious clusters found and then the 95% quantile of that M_k distribution as a threshold for high density regions. Afterwards I applied the MST algorithm to the data set and applied the edge length primary distribution and the M_k distribution. Those sources with a value M_k higher than the 5% threshold in its same z range are considerer clusters.

In Table 3.1 are summarized all the algorithms presented in this Chapter, together with their advantages and drawbacks. The algorithms selected are complementary to each other, so combining their use leads to a consistent result.

Algorithm	Advantages	Drawbacks
OPTICS + DBSCAN	Resistant to noise Find clusters of arbitrary shapes and sizes	DBSCAN strongly dependant of the initial parameters
Voronoi Tesselation	Find clusters of arbitrary shapes and sizes	Cluster definition strongly dependant of the simulations
MST	Simple to understand and compute	Tendency to build unphysical elongated chains Bad behaviour with noise

Table 3.1: Summary of the algorithms used in the data set and their advantages and drawbacks.

CHAPTER 4

Datasets and Catalogs

The advent of large area surveys opens the opportunity to set the results on several key issues based on strong statistical foundations, due to the large amount of available data. The selection of large and well-defined samples is of great importance to properly address several issues, such as studying environments and cosmic evolution for different populations. In particular, the radio, infrared, and optical observations available thanks to recent large-area surveys are a powerful tool, allowing us to perform photometry and obtain spectroscopic redshifts for a large number of sources.

4.1 The Sloan Digital Sky Survey

The Sloan Digital Sky Survey (SDSS, York et al., 2000; Eisenstein et al., 2011) is a large imaging and spectroscopic survey performed using the Sloan Foundation 2.5-m wide-angle optical telescope at Apache Point Observatory in New Mexico, United States. Currently it is being extended to the Southern Sky with the 2.5-m Du Pont optical telescope at Las Campanas Observatory in Chile. The SDSS started in the year 2000 and since then it has created the most detailed three-dimensional maps of the Universe ever made, with deep multi-color images of one third of the sky, making it one of the most successful surveys in the history of astronomy.

SDSS includes three types of data: images, spectra, and catalog data (parameters measured from images and spectra, such as magnitudes and redshifts). The imaging camera collects photometric imaging data using an array of 30 2048 by 2048 pixel CCDs arranged in six columns of five CCDs each. Each row has five different optical filters named u, g, r, i, z with average wavelengths of 355.1, 468.6, 616.5, 748.1 and 893.1 nm, with 95% completeness in typical seeing to magnitudes of 22.0, 22.2, 22.2, 21.3 and 20.5 respectively. The global astrometric precision is 0.1", and the median Point Spread Function (PSF) Full Width at Half Maximum (FWHM) in the r-band is 1.3". The SDSS telescope uses the drift scanning technique, which tracks the telescope along a great circle continuously recording small strips of the sky, allowing consistent astrometry over a wide field. The camera moves along great circles on the sky and reads the CCDs at the same time. As an image of an object moves along the column of CCDs, a CCD in each row collects the data of that object. This way the camera produces for the same column of CCDs five images of the same object, one

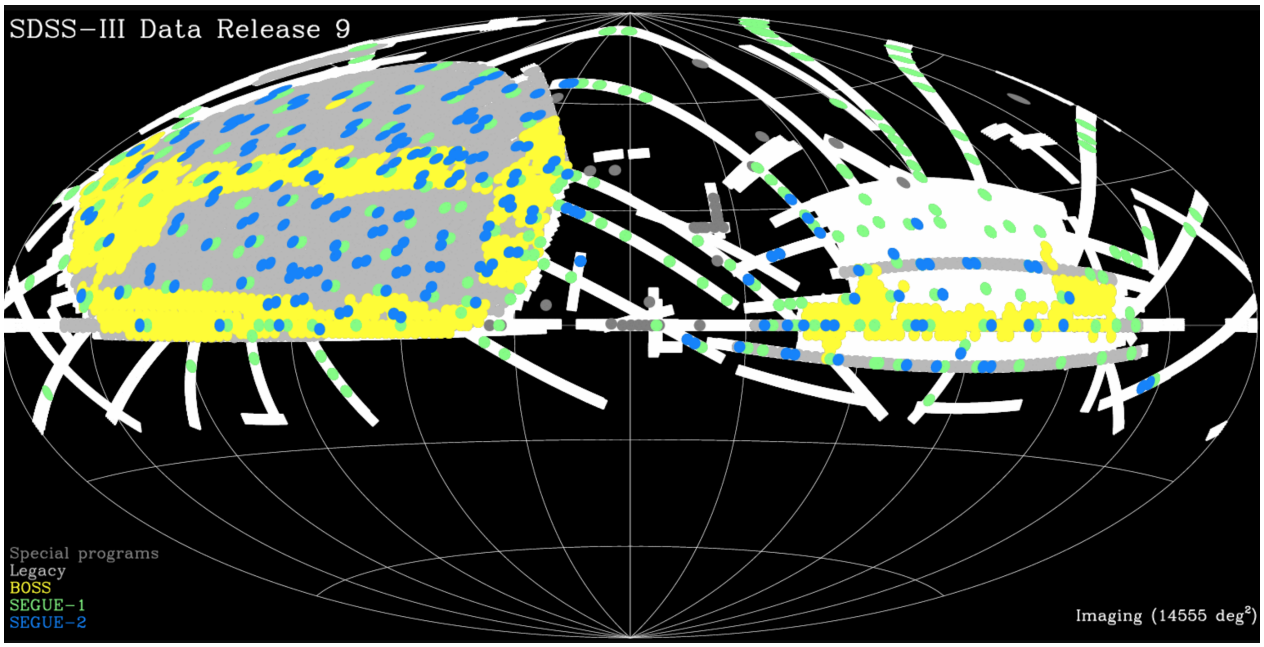

Figure 4.1: Map of the sky coverage of the SDSS DR9. In white there is the distribution on the sky of all SDSS imaging. In grey there is the original SDSS observing plan, which ran from 2000 to 2008 and is now known as the SDSS Legacy Survey. In yellow there are the areas of the sky covered by the BOSS spectrograph used for the first time in this DR. Green and blue represents the areas of the sky covered by the programs SEGUE-1 and SEGUE-2 respectively, two similar programs that obtained spectra of thousands of stars over a range of spectral types to investigate the Milky Way structure.

from each CCD in that column. Since an object takes 54 seconds to move from the beginning of a CCD to the end, the effective exposure time in each filter is 54 seconds. Because there is some space between the rows of CCDs it takes 71.7 seconds for an image to move from the beginning of one row to the next. Each row corresponds to a different filter, so each object has one image in each filter, taken at 71.7 second intervals.

In this work it is adopted the Data Release 9 (DR9, Ahn et al., 2012), which includes all imaging and spectra from prior SDSS data releases and more than 800,000 spectra over 3,300 square degrees of sky observed with the new 1,000-fiber BOSS spectrograph, the sky coverage is shown in Fig. 4.1. It also provides corrected astrometry for the imaging from DR8. The spectroscopic data obtained from previous data from DR1 to DR8 were taken by the SDSS spectrograph. This instrument takes 640 spectra in a single observation using a plate, an aluminium disk placed in the focal plane of the telescope. Each plate corresponds to a specific patch of sky, and is pre-drilled with holes corresponding to the sky positions of objects in that area, meaning each sky area requires its own unique plate. Optical fibers of 3" diameter plugged into each hole bring the light from the focal plane to the spectrograph. The SDSS spectrograph has a wavelength coverage of 3800 - 9200 Å, and a resolution of 1500 at 3800 Å.
DR9 is the first data release from the BOSS spectrograph, an instrument for which 1,000 holes are drilled in an aluminium plate with optical fibers of diameter 2". Each spectrum is split into two parts, blue and red, and the two parts are recorded on separate CCDs. The blue cameras have a coverage of 3600 - 6350 Å and the red cameras cover at least 5650 - 10000 Å, having a resolution of

2500 at 9000 Å.

The data is processed by a pipeline that reduces CDD images, performs the astrometric calibration, and detects objects, calculating position, brightness and shape (Padmanabhan et al., 2008). The photometric pipeline provides a simple star/galaxy separator, depending whether the object is extended ("galaxy") or point-like ("star") based on the difference between the model and PSF magnitude. In this work are only selected the objects classified as "galaxy" by the photometric pipeline. The r magnitude completeness limit is r < 22.5 (Anderson et al., 2012). The summary of all the observations performed in this data release is given in Table 4.1.

Sky coverage	14,555 square degrees
Catalog objects	932,891,133
Stars	260,562,744
Galaxies	208,478,448
Unknown	12,682
Galaxy spectra	1,457,002
Quasar spectra	228,468
Star spectra	668,054

Table 4.1: Summary of the observations performed in the DR9.

4.2 Catalogs of RGs and BL Lacs

The catalogs used to compare the properties between FR Is and BL Lacs have been selected for the reliability in their source selection, with well defined classes. In the following are defined the catalogs that are used in Chapters 5 and 6 to compare the environments between FR Is and BL Lacs.

4.2.1 FRICAT

The FRICAT (Capetti et al., 2017) is a catalog of 219 FR I RGs selected morphologically combining data from the radio catalogues National Radio Astronomy Observatory Very Large Array Sky Survey (NVSS, Condon et al., 1998), Faint Images of the Radio Sky at Twenty-cm (FIRST, White et al., 1997) and the SDSS survey. In the first place they selected the sources classified as radio loud AGNs from a sample of 18,286 sources, constructed by combining another sample from the SDSS DR7 selected spectroscopically by a group from the Max Planck Institute for Astrophysics and The Johns Hopkins University (Best & Heckman, 2012), with the radio catalogues NVSS and FIRST. They focused on the 3,357 sources with redshift $z < 0.15$ and visually inspected the FIRST images of every single source, looking for those whose radio emission reaches a distance of at least 30 kpc from the center of the optical host. They selected those sources showing either one-sided jet or two-sided jets, in which the surface brightness decreases along its whole length, lacking of any brightness enhancement at the jet end. They considered also sources with bent jets (NATs), but excluded sources having a substantial brightening along the jet (WATs). The authors conducted this morphological analysis independently, and included in the catalog as FR Is the sources for which at least two of them agree on their classification, see an example in Fig. 4.2.

In addition they considered 14 nearby objects ($z < 0.05$) with radii among 10 and 30 kpc and called them the "small" FR Is sample or sFRICAT.

The FRICAT hosts are remarkably homogeneous, since they are all luminous red Early Type Galaxies (ETGs) with a distribution of their absolute magnitude covering the range -21 $< M_r <$ -24, peaking at $M_r \sim$ -22.5. Their black hole masses range from 10^8 up to $3 \times 10^9 M_\odot$. Their spectroscopic classification based on the optical emission line ratios indicates that they are all LERGs, except for four objects that could not be spectroscopically classified.

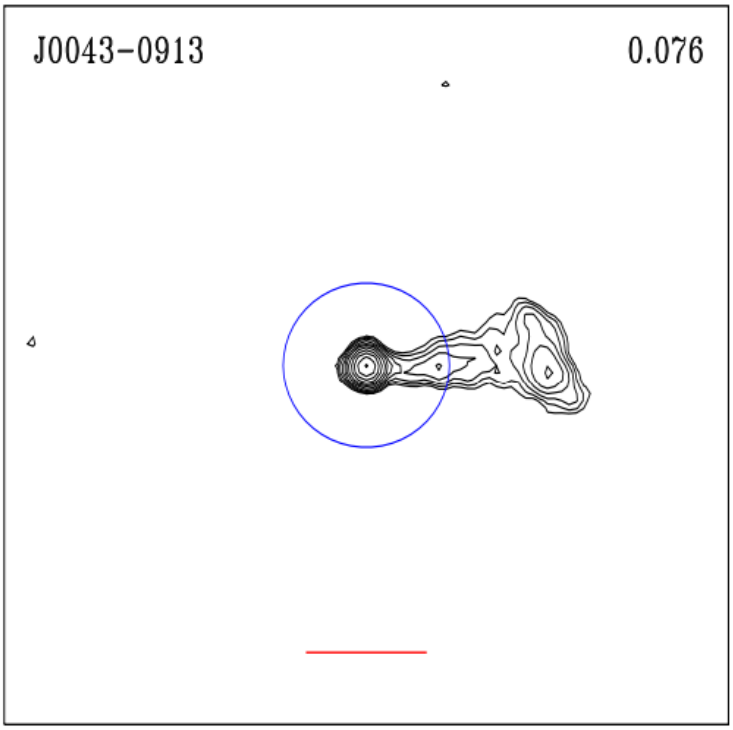

Figure 4.2: FIRST images of a FR I included in FRICAT. The blue circle is centered on the host galaxy and has a radius of 30 kpc, the minimum size considered. The field of view is 3' × 3' and the red tick at the bottom is 30" long.

4.2.2 Roma-BZCAT

The "Multifrequency Catalogue of Blazars", also named as Roma-BZCAT, constitutes the most comprehensive list of blazars known to date and it is based on multifrequency surveys and on information reported in the literature. The first version was presented by Massaro et al. (2009) and it consisted on 2,728 sources. The most recent edition is the fifth (Massaro et al., 2015a) and it contains 3,561 sources, about 30% more than the first one. There are several criteria they consider for classifying a source as a blazar. The first one is that the source must be detected in the radio band down to mJy flux densities, either in the catalog NVSS, FIRST, Sydney University Molonglo Sky Survey Source Catalog (SUMSS, Mauch et al., 2003), Green Bank 6-cm Radio Source Catalog (GB6 Gregory et al., 1996), or Parkes-MIT-NRAO Surveys (PMN Wright et al., 1994); moreover, the sources must have a compact radio morphology or, when extended, one dominant core and a one-sided jet. In addition, there must be detection of isotropic X-ray luminosity close to or higher than 10^{43} erg s^{-1}. Finally, an optical spectra must be available in the literature confirming the classification as a blazar. If the object is likely a blazar but there is no spectra to confirm this

classification, the object is reported as a "BL Lac candidate". In the particular case of FSRQs they must present radio flat spectra, i.e., the spectral index α measured between 1.4 GHz and 5 GHz must be lower than 0.5.

Each blazar is identified by a three-letter code, where the first two are BZ for blazar and the third one specifies the type followed by its equatorial coordinates (J2000). The types they distinguish are the following:

- **BZB**: BL Lacs, AGNs with a featureless optical spectrum, or very weak and narrow emission/absorption lines.
- **BZG**: BL Lac of Galactic type. This classification was added in the fifth edition and is used for sources usually reported as BL Lac objects in the literature, but exhibiting a typical elliptical galaxy spectrum with a low Ca H&K break contrast (see Fig. 4.3). This is defined by the ratio $C = (F_- - F_+)/F_+$ where F_- and F_+ are the mean flux densities measured in small ranges ($\sim$ 200 Å) at wavelengths just lower and higher than that of the break (Massaro et al., 2012).
- **BZQ**: FSRQ, with an optical spectrum showing broad emission lines and flat radio spectrum ($\alpha < 0.5$).
- **BZU**: Blazars of Uncertain type, adopted for a number of sources having peculiar characteristics but also exhibiting blazar activity: for instance, occasional presence/absence of broad spectral lines or other features, transition objects between a RG and a BL Lac, galaxies hosting a low luminosity blazar nucleus, etc.

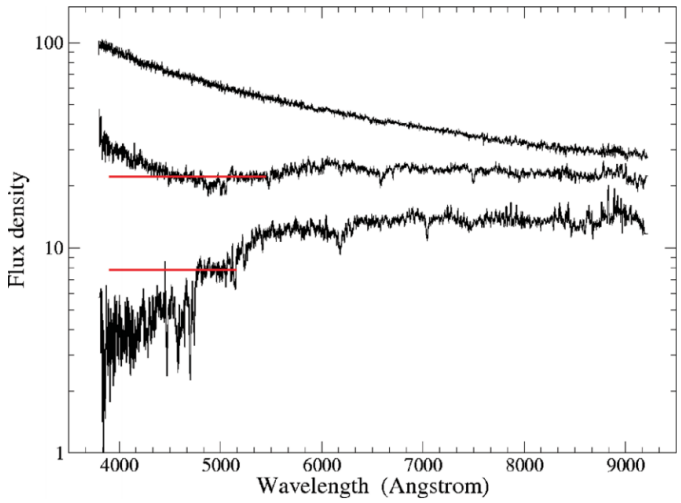

Figure 4.3: SDSS spectra of three BL Lac objects showing different ratio of the nuclear to galaxy luminosities. From top to bottom: BZB J1120+4212 ($(u-r)_{obs} = 0.4$), BZB J0909+3105 ($z = 0.272$, $(u-r)_{obs} = 1.3$) and BZB J0751+2913 ($z = 0.194$, $(u-r)_{obs} = 2.9$). Red lines correspond to the mean flux level in a 400 Å, a wide wavelength interval in the Ca H&K break used to distinguish galactic type BL Lacs (Massaro et al., 2012).

Most of the sources of the 5-th edition of the Roma-BZCAT are BZQs, 1,909. From all the 1,151 sources classified as BZBs, 92 are reported as candidates because they could not find an optical spectra to confirm their classification. Moreover, only 369 of the BZBs have a known redshift, about

a 30% because of lacking of any emission/absorption features in their optical spectra. The rest of the sources are 274 BZGs and 227 BZUs.

In addition to their classification and to the J2000 coordinates derived from VLBI, they give the following information for each source (when available): the apparent magnitude R, radio flux density from NVSS, FIRST, SUMSS, GB6 or PMN, microwave flux density at 143 GHz from PLANCK (Planck Collaboration et al., 2014), the 0.1 - 2.4 keV X-ray flux from ROSAT archive (Voges et al., 1999) or Swift-XRT catalogues (Evans et al., 2014), hard X-ray flux (15 - 150 keV) from Palermo BAT Catalogue (Cusumano et al., 2010), γ-ray flux from the First and Second *Fermi* γ-ray LAT point source catalogs (Abdo et al., 2010; Nolan et al., 2012, 1FGL and 2FGL, respectively) and redshift.

This catalog was designed to be the most complete list of published blazars, and it has been extensive used for identifying the counterparts of high energy sources; in fact, it has been used by the *Fermi* collaboration in the elaboration of all of their γ-ray source catalogues. It has been probed to be a useful tool to extract samples satisfying statistical criteria for investigating blazar properties and evolution. However, the completeness of the catalogue is an open problem. The number of sources is higher on the Northern Hemisphere because of the sky coverage the surveys used is not uniform. Moreover, many of the sources have been identified using spectroscopic observations available in the SDSS, a survey of the Northern Hemisphere, and there is no similar coverage in the Southern sky yet.

4.2.3 Quiescent elliptical catalog

Since FR Is are hosted in luminous elliptical galaxies (M_r < -21.5), I build a catalog of quiescent elliptical galaxies having the same properties of the hosts of FR Is to compare the large-scale environments of these two populations. I first considered all the sources listed in the Galaxy Zoo [1] DR 1 (Lintott et al., 2008). Galaxy Zoo is a citizen astronomy project which invites people to assist in the morphological classification of large numbers of galaxies in the largest galactic census ever carried out. In the original Galaxy Zoo project, volunteers classified a data set made up of $\sim$ 900,000 SDSS galaxies as belonging to one of six categories: elliptical, clockwise spiral, anticlockwise spiral, edge-on, star/don't know or merger, between July 2007 until February 2009. I considered those galaxies classified as ellipticals in the Galaxy Zoo DR 1 with at least 45 votes.

Then I selected from these sources those for which an optical spectra is available in the SDSS DR9. I included only sources with a clean photometry (i.e., SDSS flags q_{mode}=1 and Q > 2) and classified as galaxies (i.e., SDSS flag cl=3). Galaxies with spectroscopic redshift higher than $z > 0.15$ were excluded to match the limit of the FRICAT, since the aim is to compare this two catalogs. As last step, sources with a radio counterpart within 5" were excluded to avoid possible RG contamination.

This selection procedure led to a final sample of 3,523 quiescent elliptical galaxies all spectroscopically confirmed, hereafter ELL catalog.

4.2.4 Catalog of mock sources

A catalog of fake sources was created shifting the position of each source in the quiescent elliptical catalog by a random shift between 2 and 3 degrees in a random direction in the sky (hereafter MOCK catalog). The smallest value for the shift was chosen to be greater than 2 degrees, the maximum angular separation correspondent to 2 Mpc in the RG catalogs and smaller than 3 degrees

[1] www.galaxyzoo.org

to preserve the sky distribution of sources inside the SDSS footprint. The random shift was applied to the quiescent elliptical catalog before performing the last step, the removal of radio sources. Since this catalog serves as a comparison for a flux limited sample in which the typical luminosity varies across the volume of the sample, the redshift of another object was assigned to each source with no repetitions to maintain the same redshift distribution in both catalogs, and to preserve the same luminosity distribution I kept all the optical magnitudes associated with each redshift value. Analogously, the final step was to exclude fake sources having a radio source within 5". The final MOCK sample lists 4,056 sources. The small difference between the source number in the MOCK and in the ELL catalogs is due to the source cut lacking of a radio counterpart within 5" from the optical positions, since it is less likely to find such associations in random positions of the sky.

4.3 Catalogs of groups and clusters of galaxies

To carry out the analysis, several catalogs of galaxy clusters and groups available in the SDSS footprint were selected.

4.3.1 T12 catalog

A catalog of groups and clusters of galaxies covering the central 7,221 square degrees of the SDSS was considered, as seen in Fig. 4.4 (hereinafter T12 catalog, Tempel et al., 2012). This catalog was selected because it has the largest number of galaxy cluster/group detections with spectroscopic redshifts in the SDSS up to date. The catalog searches for clusters and groups using the method friends-of-friends (FoF, Press & Davis, 1982). They used a modified version of the FoF algorithm with a variable linking length in the transverse and radial directions to eliminate selection effect, applied to the SDSS DR8. Their primary selection was to use those objects that were classified as galaxies by the SDSS algorithm and with an optical spectra available, cleaned from duplicated entries and oversaturated stars or other artefacts. The lower limit of the sample is m_r =17.77 applied after Galactic extinction correction, the limiting magnitude for which the spectroscopic galaxy sample is complete (Strauss et al., 2002). They report 576,493 galaxies in a redshift range between $z = 0.009$ to exclude at lower redshift the local supercluster, and $z = 0.2$ because at higher redshift the sample becomes very diluted. The distribution peaks at $z = 0.08$ becoming less efficient at greater z values. Almost half of the galaxies in their sample (46%) belong to a group and 10% of galaxies belong to groups with ten or more members. Most of their groups (60%) have two member and 21% have four or more members.

4.3.2 GMBCG catalog

I furthermore considered a catalog of optically selected galaxy clusters using the new Gaussian Mixture Brightest Cluster Galaxy (GMBCG) algorithm to the SDSS DR7 (hereinafter GMBCG catalog Hao et al., 2010). This algorithm detects clusters by combining the identification of the red sequence and the brightest cluster galaxy (BCG), two features that are unique for galaxy clusters and do not exist among field galaxies. These features provide a powerful means to detect galaxy clusters without projection effects. The algorithm uses the GMBCG and the Error Corrected Gaussian Mixture Model (ECGMM) to identify the BCG plus red sequence feature and convolves the identified red sequence galaxies with a spatial smoothing kernel to measure the clustering strength of galaxies around BCGs. The GMBCG algorithm uses the BCG's photometric redshift to determine the

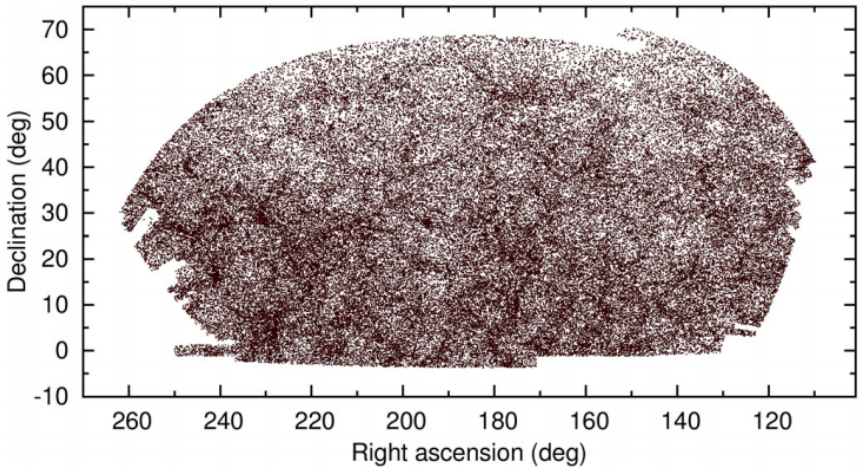

Figure 4.4: T12 catalog coverage of the central 7,221 square degrees of the SDSS.

metric aperture size and uses the red sequence color to select member galaxies evaluating them with ECGMM. The final catalog consists of about 55,000 clusters in a redshift range up to $z = 0.55$.

CHAPTER 5

Environments of FR I Radio Galaxies

According to the Unification Model, the environments of the intrinsic low luminosity radio loud AGNs, i.e FR Is and BL Lacs, are expected to be similar. Here I presented a study of the large-scale environment of a sample of FR Is reported in the FRICAT, so in Chapter 6 I can compare the large-scale environments of FR Is with those of BL Lacs using the same methodology.

For each source listed in both the FRICAT and the ELL catalog, I downloaded a table listing all the optical sources detected in the SDSS DR9 having a clean photometry and classified as galaxies according to the SDSS algorithm (i.e., SDSS flags q_{mode}=1, Q=3 and mode=1) lying within a circular region correspondent to 2 Mpc at the redshift of the central source, that is either a FR I, a quiescent elliptical galaxy (ELL) or a MOCK source. The value 2 Mpc was selected because since the typical size of a cluster is 1 - 2 Mpc, I wanted to be conservative and be able to identify when a source belongs in a cluster, even if it lies in its outskirts.

Unless otherwise stated I adopted cgs units for numerical results and I assumed a flat cosmology with $H_0 = 69.6$ km s^{-1} Mpc^{-1}, $\Omega_M = 0.286$ and $\Omega_\Lambda = 0.714$. Spectral indices α are defined by flux density $S \propto \nu^{-\alpha}$.

5.1 Comparing FRICAT with catalogs of clusters/groups of galaxies

Here I presented an analysis of the large-scale environment of a well-defined and statistically homogeneous sample of FR Is using the FRICAT. This is a catalog at $z < 0.15$ lying in the footprint of SDSS, selected on the basis of homogeneous criteria (as explained in Chapter 4) and classified using radio, infrared and optical observations, uniformly available for all FR Is. All selected FR Is RGs belonging to the FRICAT are optically selected LERGs.

For the current analysis I only selected sources lying within the footprint of the central part of the SDSS because the comparison catalog (i.e., T12) only covers this area of the sky, thus the FRICAT that includes 219 RGs was reduced to 195 sources. In addition, I compared the results on the RGs population with those derived for a catalog of quiescent elliptical galaxies (ELL, see Chapter 4). This control sample was selected having similar colors to the RGs, allowing a direct comparison.

5.1.1 Positional cross-matches FRICAT and T12 catalog

I cross-matched the positions of the groups/clusters of galaxies from the T12 catalog with the positions of each galaxy reported in the FRICAT and also to the positions of each galaxy reported in the the catalog of quiescent elliptical galaxies (ELL) for comparison.

I considered a FR I/ELL to be associated with a group or a cluster of galaxies of richness with at least $N_{gal} = 4$ listed in the T12 catalog, when both following criteria are satisfied:

- The projected distance d_{proj} between the center of the cluster and the FR I/ELL is smaller than 2 Mpc.
- The difference between the redshift of the cluster z_{cl} and the central FR I/ELL z_{src} is $\Delta z = |z_{cl} - z_{src}| < 0.005$, corresponding to a velocity difference of 1,500 km/s.

In addition, I considered a FR I/ELL in a rich environment when there was more than one group in T12 satisfying the previous criteria and with T12 richness $N_{gal} = 2$ or 3. I added this requirement since the clustering algorithm FoF used to build the T12 catalog tends to split large clusters into smaller ones creating an unphysical elongated chain, thus a large cluster could be found in separate substructures in the T12 catalog. The total number of FR Is I found in clusters according with the positional cross-matches using the T12 catalog was 139. For 34 of them ($\sim$ 25% of the total number), the entire cluster was found partitioned in a chain of several substructures.
The error for this method was found searching for cross-matches with the T12 catalog under the same previous conditions with a MOCK population of elliptical galaxies.

5.1.2 Positional cross-matches FRICAT and GMBCG catalog

I performed a cross-match of the positions reported in the GMBCG catalog and those reported in FRICAT, to discover how many of the FR Is are compatible with being a BCG. I considered a FR I at z_{src} to be a BCG when its redshift difference computed with that reported for the central BCG in the GMBCG catalog (z_{cl}) is $\Delta z = |z_{cl} - z_{src}| < 0.005$, and it lies at a projected distance d_{proj} smaller than 1 kpc. I found 20 sources that accomplish these criteria, thus 10% of the sample selected from the FRICAT is compatible with being the BCG of their cluster.

5.1.3 Cosmological neighbors

The peak of the T12 catalog redshift distribution lies around $z = 0.08$, at higher redshifts the performance of the FoF algorithm used to fund clusters by this catalog decreases, thus for sources at redshifts higher than 0.08 the environmental density could be underestimated. As a new method, I considered all the SDSS sources lying within a 2 Mpc radius from the central source and having a spectroscopic redshift which differs from that of the central source in less than 0.005, and I defined these sources as *"cosmological neighbors"* . I found all the *"cosmological neighbors"* in the fields of the sources of FRICAT, and for the ELL and MOCK catalogs for comparison. A FR I/ELL at $z <$ 0.1 was considered in a galaxy rich large-scale environment, also called a *"cosmological neighbor"* overdensity, when the number of *"cosmological neighbors"* within 500 kpc was higher than a certain threshold, defined according to the following. Inspecting the MOCK catalog at the same redshift bin of the central FR I/ELL (sizes of 0.01), this threshold was set where less than 5% of the fake MOCK sources were surrounded by the same or a higher number of galaxies. However, for redshifts greater than $z > 0.1$, to prevent spurious fluctuations due to small number statistics I considered the number of *"cosmological neighbors"* imposed for a source to be in a rich large-scale environment

greater than 2 within 1 Mpc, a number higher than the threshold detected using the MOCK catalog.

In addition, I defined the so-called *"candidate elliptical galaxies"*. For each FR I redshift, I created the $u-r$ vs $g-z$ color-color plot for all the galaxies from the ELL catalog with a difference in their redshift from that of the central FR I of $\Delta z < 0.005$. Using the Kernel Density Estimator (KDE), I selected those elliptical galaxies falling inside the contours at a 90% level of confidence. KDE is a method that provides an effective procedure to estimate the probability function by assuming a gaussian as a density estimator function. For each FR I, I represented all the SDSS galaxies in that same color-color plot, and selected those falling inside that contour selected at the 90% level of confidence, thus optical colors of these SDSS sources are compatible with those of quiescent elliptical galaxies at the redshift of the FR I (see Fig. 5.1).

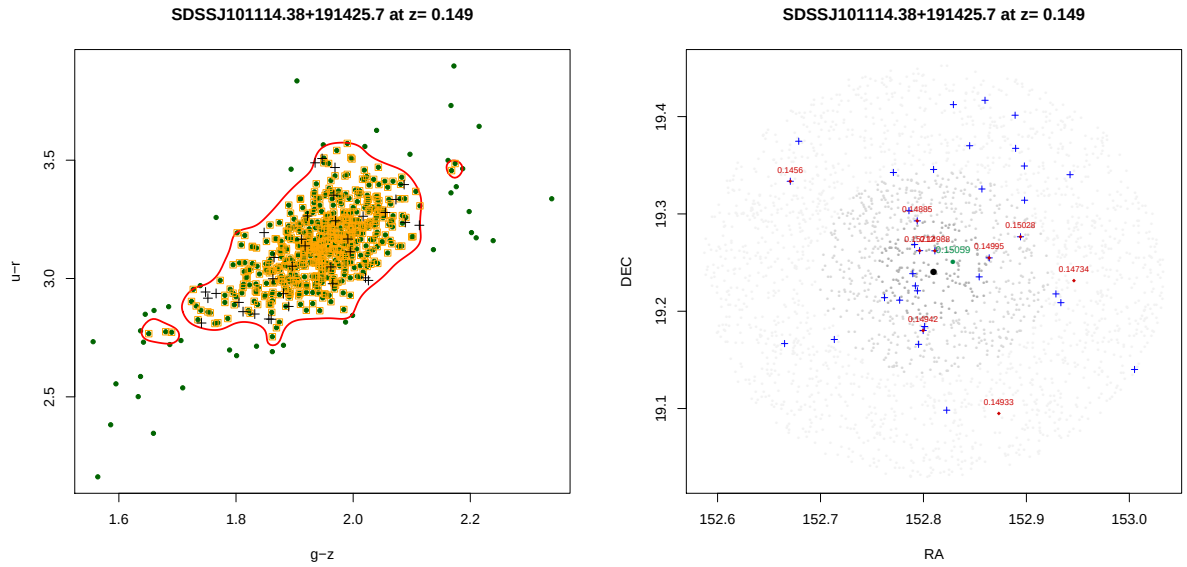

Figure 5.1: *Left:* $u-r$ vs $g-z$ color-color plot for elliptical galaxies at a $\Delta z < 0.005$ from the selected FR I at $z_{src} = 0.149$. Green circles are elliptical galaxies from the ELL catalog. The red line corresponds to the contour selected at the 90% level of confidence using the KDE technique. Orange squares are those elliptical galaxies from the ELL catalog falling inside that 90% contour. Black crosses are the *"candidate elliptical galaxies"*, those galaxies from the SDSS selected within 2 Mpc of the FR I falling inside that 90% contour, meaning their optical colors are compatible with being a quiescent elliptical galaxy at a similar redshift of the central FR I. *Right:* All the SDSS sources within a circular region of 2 Mpc having a clean photometry are plotted in decreasing intensities of grey, indicating those inside 500 kpc, 1 Mpc and 2 Mpc respectively. A green point marks the location of the closest group/cluster of galaxies from the T12 catalog at $\Delta z < 0.005$, together with its redshift value. Red points indicate *"cosmological neighbors"* and their redshift, i.e., sources with a spectroscopic redshift in the SDSS $\Delta z < 0.005$. Blue crosses indicate *"candidate elliptical galaxies"*.

The source SDSSJ104045.34+395448.5 at $z = 0.134$ is an example for which the environmental density using the positional cross-match with the T12 catalog was underestimated, since a single group of galaxies with $N_{gal} = 2$ was identified in a 2 Mpc radius from this FR I. Consequently it did not accomplished the requirements to be considered in a galaxy rich large-scale environment by that method. However, it had 6 *"cosmological neighbors"* within 2 Mpc (see Fig. 5.2). In the redshift bin

between 0.13 and 0.14 of the MOCK catalog there were 493 sources, and only 18 of them (i.e., less than 4% in this redshift bin) showed a number of *"cosmological neighbors"* larger than 6. Since this threshold was smaller than 5%, the source was indicated as a member of a *"cosmological neighbor"* overdensity. Using this method, I found 13 sources in *"cosmological neighbor"* overdensities out of the 56 sources for which no positional cross-matches were found using the T12 catalog, and all of them were at $z > 0.1$.

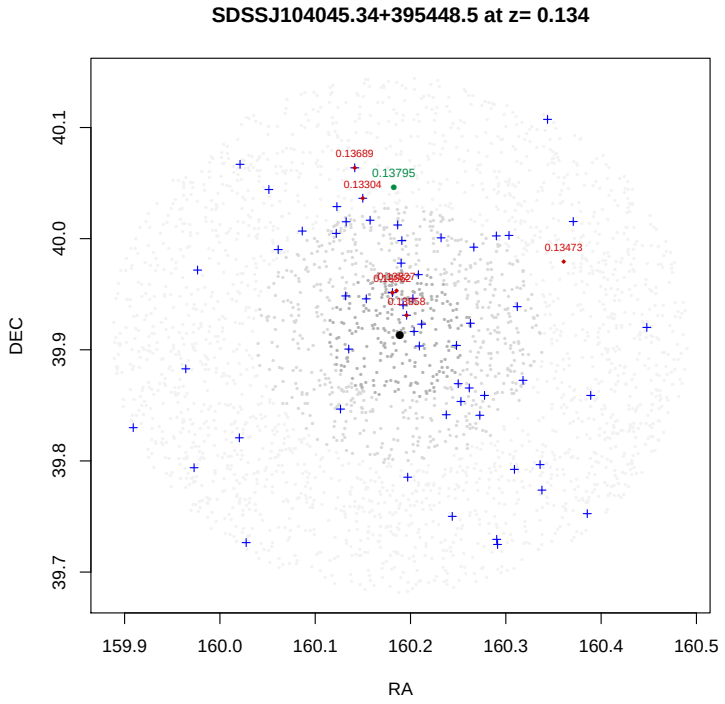

Figure 5.2: SDSS sources within a circular region of 2 Mpc having a clean photometry are plotted in decreasing intensities of grey, indicating those inside 500 kpc, 1 Mpc and 2 Mpc respectively. For this FR I (black central point) there is an association with a group of galaxies from the T12 catalog with an environmental density $N_{gal} = 2$ and located further than 1 Mpc from the central source (green point). However the number of *"cosmological neighbors"* is 6 (in red with the redshift indicated above the point), three of which lie within 500 kpc, above the threshold to consider a source in a *"cosmological neighbor"* overdensity. Blue crosses mark the location of the *"candidate elliptical galaxies"*.

5.1.4 Results

In Fig. 5.3 I show an example of a FR I found to inhabit a galaxy rich large-scale environment using both methods previously described, i.e., there was a positional cross-match with a cluster reported in T12 catalog with richness $N_{gal} = 16$ and I found 6 *"cosmological neighbors"* inside a 500 kpc radius from the central FR I, when more than 95% of the sources in the MOCK catalog at the same redshift bin had 2 or less *"cosmological neighbors"*. This FR I was also a BCG candidate according to the positional cross-match with the GMBCG catalog.

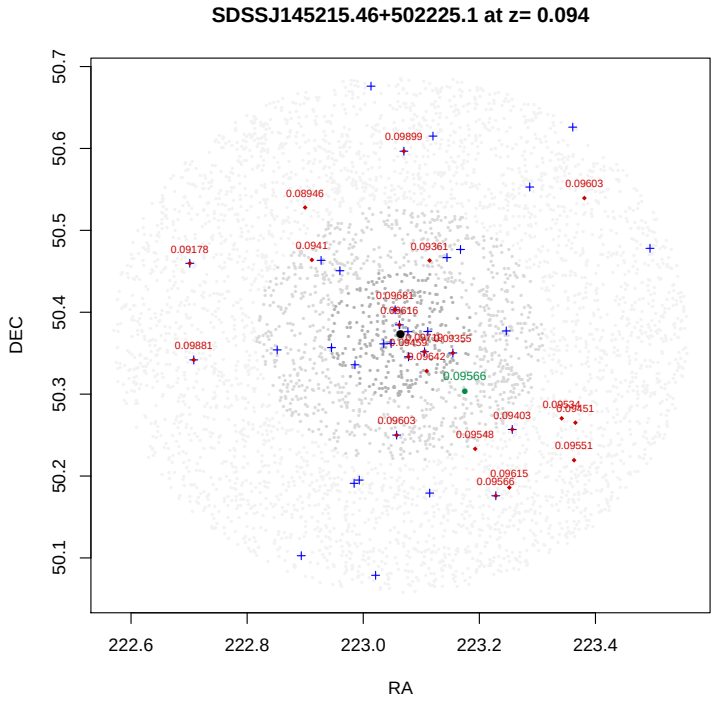

Figure 5.3: An example of the galaxy rich large-scale environment for the FR I SDSSJ145215.46+502225.1. Three intensity-decreasing shades of grey are used to mark the SDSS sources located within 500 kpc, 1 Mpc and 2 Mpc, respectively. Blue crosses mark the *"candidate elliptical galaxies"*, red squares represent *"cosmological neighbors"* together with their redshift value and the green circle shows the location of the closest galaxy cluster according to the T12 catalog. This FR I is also a BCG candidate according to the GMBCG catalog.

From the positional cross-matches of FRICAT with the T12 catalog, I show in the left panel of Fig. 5.4 that plotting the projected distance from each FR I to the closest galaxy group/cluster as function of Δz, more than 70% of the FR Is lie at $\Delta z < 0.005$, thus are in galaxy rich environments according to this method. Quiescent elliptical galaxies in the ELL sample also show a significant fraction (58%) of associations with groups/clusters of galaxies as seen in Fig. 5.4 right panel. I estimated the probability of finding spurious associations by applying the same analysis to the MOCK sample, created with the same redshift distribution of the ELL catalog. Sources in the MOCK sample show a uniform distribution in the Δz vs d_{proj} plot as expected since they were chosen to lie in random sky positions, their distinct behaviour with respect to the real sources is seen in the right panel of Fig. 5.4.

In the left panel of Fig. 5.5, I represented the number of *"cosmological neighbors"* (N_{cn}) within 2 Mpc as function of redshift of the central FR I and ELL (z_{src}), and in the right panel of the same figure the average number of *"cosmological neighbors"* within 2 Mpc as function of redshift for both classes. Here it is shown that there is no significant difference in cluster richness between both classes when they both reside in groups/clusters of galaxies, so in the situation when FR Is and ELLs lie in galaxy rich environments, these are similar.

As a comparison between these both methods previously mentioned, I represented in the left panel of Fig. 5.6 the fraction of FR Is and ELL found in galaxy rich large-scale environment evalu-

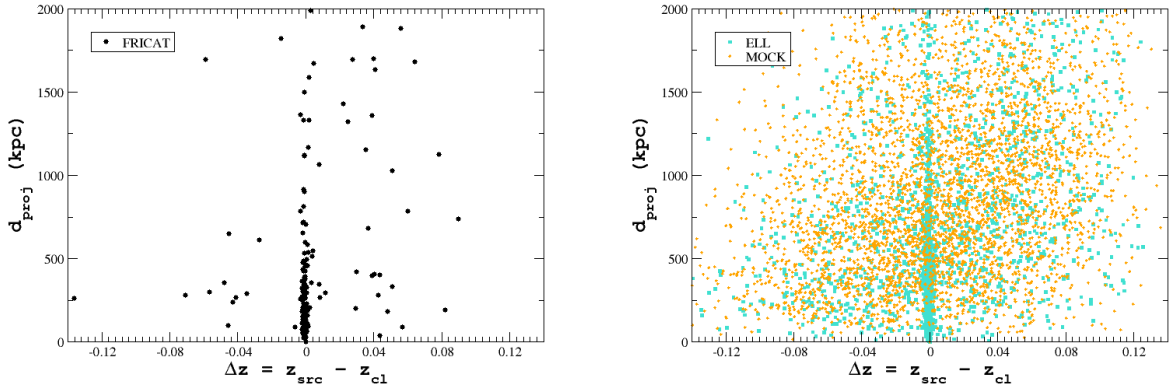

Figure 5.4: *Left:* the projected distance d_{proj} as function of the redshift difference Δz between that of the FR I (z_{src}) and the positional closest group/cluster of galaxies reported in the T12 catalog (z_{cl}). *Right:* same as left for the quiescent elliptical galaxies (ELL) represented by cyan squares and and for the mock galaxy sample (MOCK) shown as orange diamonds.

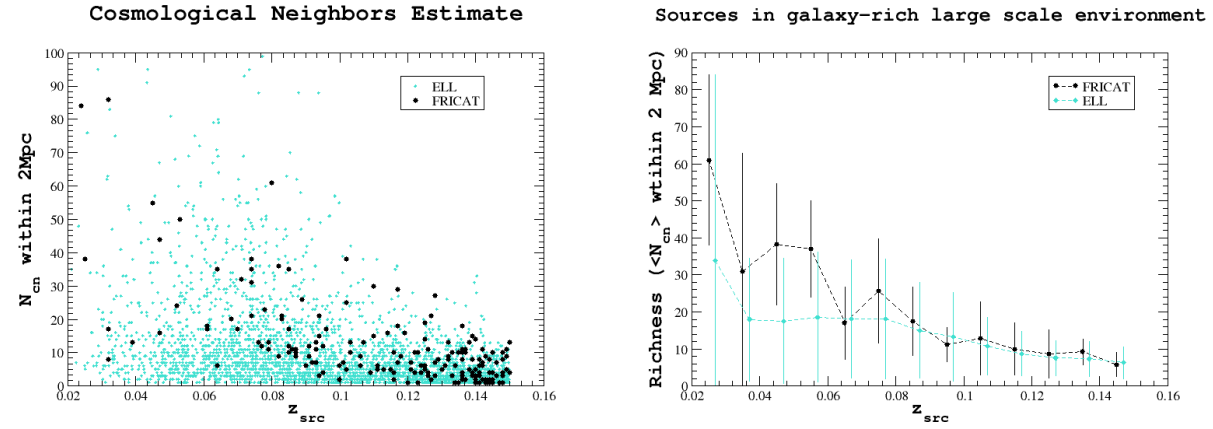

Figure 5.5: *Left:* Number of all *"cosmological neighbors"* N_{cn} inside 2 Mpc vs source redshift z_{src}. Black circles represent FR Is while cyan points represent ELLs. *Right:* The average number of *"cosmological neighbors"* $< N_{cn} >$ counted within 2 Mpc from the central source as function of the source redshift z_{src}. The error on $< N_{cn} >$ is the standard deviation. Again, black represents FR Is and cyan is used for ELLs.

ated using the cross-matches with the T12 catalog. In the right panel of the same figure I depicted the fraction of FR Is and ELL found in a *"cosmological neighbor"* overdensity. In both panels I show the fraction of MOCK sources found to reside in a group/cluster of galaxies using each method, representing the error. The efficiency of the positional cross-matches with the T12 catalog in finding groups/clusters of galaxies reduces significantly with redshift, because of the decreasing efficiency with redshift of the algorithm used by this catalog to find groups/clusters of galaxies. The effect of finding less number of sources using the *"cosmological neighbor"* overdensity method with increasing redshift is less evident than with the previous procedure but still existent, since in the SDSS the number of sources having available spectroscopic redshift decreases with redshift too. Both methods

show a gap between the fraction of FR Is and ELLs belonging to a galaxy rich large-scale environment and those in the MOCK catalog, but it is evident that a higher fraction of FR Is lie in groups/clusters of galaxies than ELL.

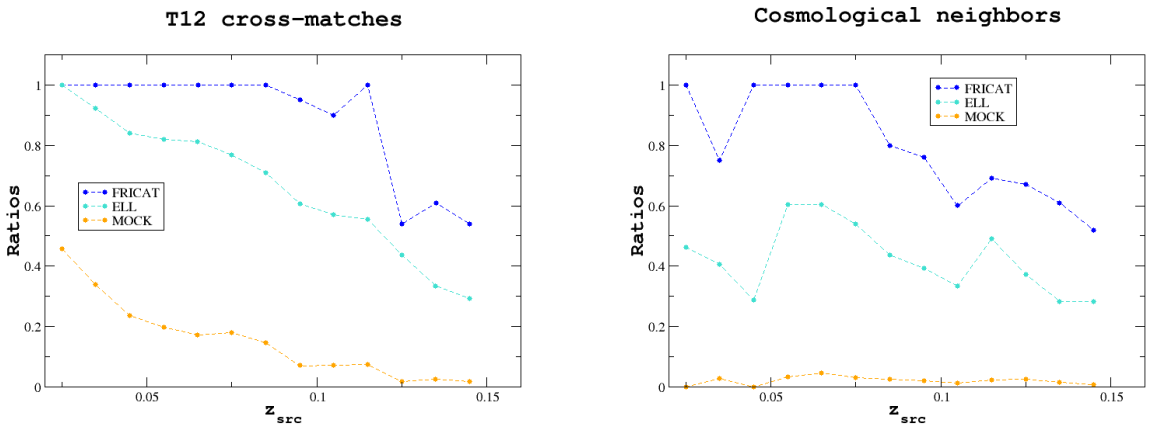

Figure 5.6: *Left:* For the positional cross-matching analysis using the T12 catalog, the fraction of FR Is inhabiting galaxy rich environments is shown in blue, same ratio for ELL in cyan and mock in orange. The efficiency significantly decreases with redshift because the performance of the algorithm used by the T12 catalog to find groups/clusters of galaxies reduces with redshift. *Right:* The same for the " *"cosmological neighbors"* analysis. The efficiency decreases with redshift, but not as much as using the T12 catalog because at higher redshift there are less sources with spectroscopic redshift available in the SDSS. It is evident how both methods show a gap between the fraction of real sources in galaxy rich large-scale environments and those in the MOCK catalog, with FR Is lying in richer environments than ELL.

Fig. 5.7 shows the total number of sources in galaxy rich environments in each redshift bin, considering the cross-matches with T12 catalog, the *"cosmological neighbors"* and their combination for FR Is in the left panel and for ELL the right panel. It is clear how *"cosmological neighbors"* improved the detection of galaxy rich large-scale environments at redshift higher than ~ 0.1, where the efficiency of the T12 catalog decreases.

As an additional check I verified the presence of the red sequence, a characteristic common to most of the galaxy clusters by building the $r - i$ vs i color-magnitude plot for each field. As previously stated, galaxies that are members of clusters of galaxies tend to be redder than background and foreground galaxies in the same field. In Fig. 5.8 I show an example for the FR I SDSSJ080113.28+344030.8, for which it is clear that both *"cosmological neighbors"* and *"candidate elliptical galaxies"* belong to the red sequence.

Finally, in the left panel of the Fig. 5.9 I show the fraction of sources considered inside a group/cluster of galaxies as function of the source redshift combining the results of the positional cross-matches with the T12 catalog and *"cosmological neighbors"* overdensities. A large fraction of FR Is sources inhabit galaxy rich ambients up to $z = 0.08$ and then the fraction decreases with redshift. The same value for ELLs shows a systematic offset of $\sim 20\%$ lower fraction at all redshifts with respect to FR Is. The right panel of this same figure shows the fraction of sources considered

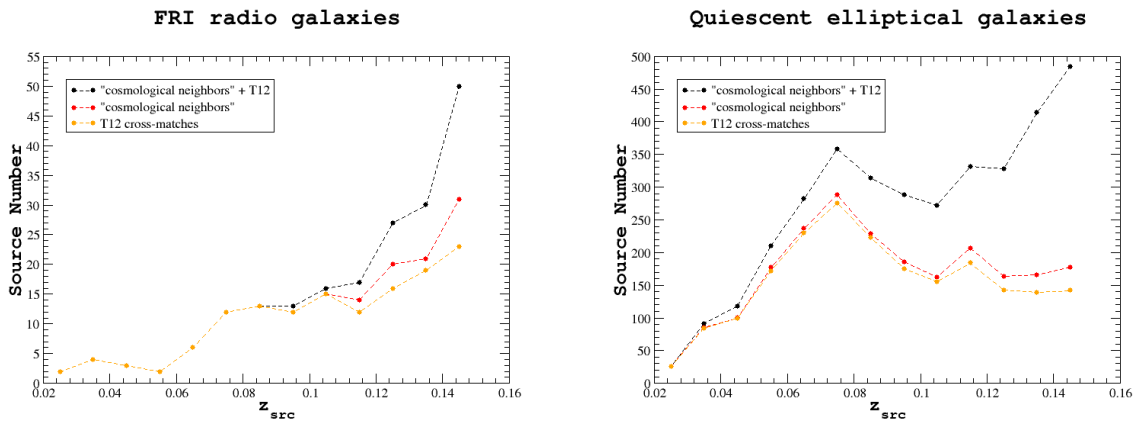

Figure 5.7: *Left:* Number of FR Is found in groups/clusters of galaxies in each redshift bin considering each method separately and their combination. Orange circles mark those sources having a cross-match with a group/cluster of galaxies in the T12 catalog, red circles mark those sources for which a *"cosmological neighbor"* overdensity was found, and black circles represent the total number of sources in a group/cluster of galaxies combining these two methods. *Right:* Same as left panel for ELLs.

inside a group/cluster of galaxies in each bin of absolute magnitude in the R band, M_r. A clear dependence of the fraction of ELL in galaxy rich environments appears with absolute magnitude, decreasing from $\sim$ 80% for the brightest galaxies down to $\sim$ 60% at $M_r \sim$ -22.5. For fainter galaxies at $M_r >$ -22.25 the percentage rises again by about a 10% mimicking a similar growth in the MOCK sample.

The reason for the deficit in the fraction between ELLs respect to FR Is might be the presence of two families of elliptical galaxies in our ELL sample. Recent studies have showed that there are two classes of elliptical galaxies related mainly to their optical luminosity (Graham, 2013). The brightest elliptical galaxies generally show a light deficit in their central regions with respect to their larger scale profile (i.e., *core galaxies*), *boxy* isophotes and a small value of specific angular momentum tending to be more luminous in both radio and X-rays. On the other hand, less luminous ellipticals have disky isophotes (i.e., *disky galaxies*) and are fast rotators (Bender et al., 1989; Hao et al., 2006). RGs are hosted only in core galaxies (Tremblay et al., 2007), and *core galaxies* are also more often found in galaxy rich environment than *disky galaxies* (Quillen et al., 2000). The presence of *disky* galaxies in our comparison ELL sample thus affects the fraction of those lying in galaxy rich environments. As seen in the right panel of Fig. 5.9, for the more luminous ELL sources, the contamination from *disky* galaxies is negligible and the fractions of ELL and FR Is lying in rich large-scale environments are both high and reaching the same value at $M_r \sim$ -23.3. At lower luminosities *disky* galaxies contribute for a larger fraction to the ELL population and, being less frequently found in rich environments (Faber et al., 1997), reduce the overall fraction of ELL associations with groups/clusters of galaxies. This could be the reason why in the right panel of Fig. 5.9 the ratios for the ELL sample are systematically below those for the FRICAT until $M_r \sim$ -23, were their fraction starts rising for brighter sources.

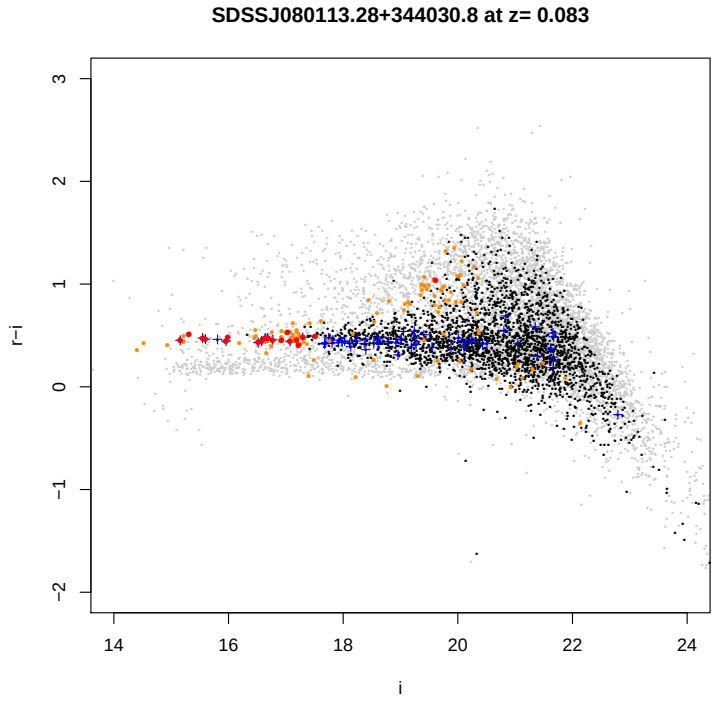

Figure 5.8: $r - i$ vs magnitude i plot for the FR I SDSS J080113.28+344030.8 at $z_{src} = 0.083$. Background/foreground SDSS sources are represented by black circles and grey points following the same trend for the shades of grey with distance used in the right panel of Fig. 5.1, while those SDSS with an available spectroscopic redshift are represented as orange points, *"cosmological neighbors"* are shown as red dots and *"candidate elliptical galaxies"* are marked as blue crosses.

5.2 Clustering algorithms

As an additional step in the analysis, I present in this section the several clustering algorithms applied to the sample of FR I RGs to analyze their large-scale environment. Different clustering algorithms can and do generate different solutions because of the different statistics of each method and their different performances, so the reason to apply several of them to the same sample is for consistency. I applied this algorithms to the SDSS DR9 optical sources having a clean photometry and classified as galaxies lying within a circular region of 2 Mpc at the redshift of the central source for the FRICAT, ELL and MOCK catalogs. When an algorithm detected the central FR I/ELL inside a group/cluster of galaxies, I only considered it belonged to a galaxy rich large-scale environment when at least one of the sources in such a group/cluster were classified as *"cosmological neighbor"* or *"candidate elliptical galaxy"*. All the algorithms used in this section were defined and explained in Chapter 3.

To define the threshold for a FR I/ELL to be considered inside a rich environment, I analyzed the MOCK sample using the same algorithms. A source was considered in a galaxy rich large-scale environment when applying the same algorithm to the MOCK catalog, less than 5% of the sources at the same redshift of the central FR I/ELL were surrounded by the same or higher number of galaxies.

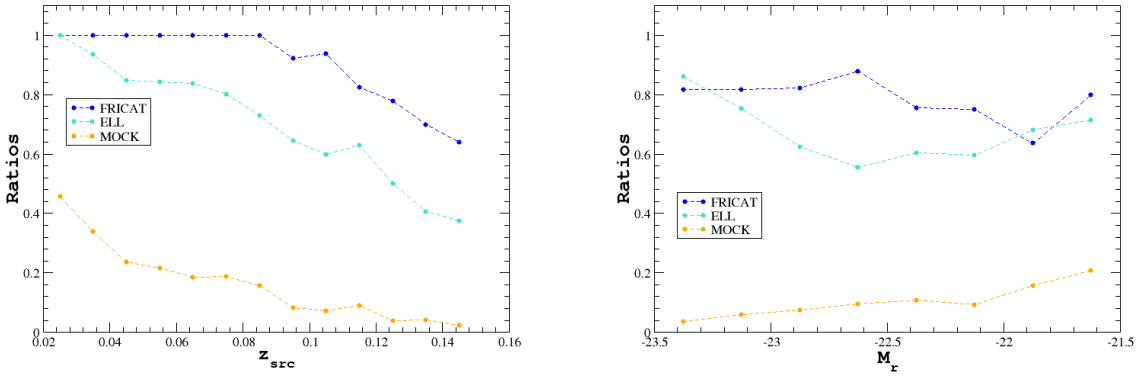

Figure 5.9: *Left:* The fraction of FR Is (blue), ELL (cyan) and MOCK (orange) that lie in galaxy rich large-scale environments as function of redshift bin. These fractions were estimated using the combination of the two methods above described, i.e., cross-matches with a cluster/group of galaxies in the T12 catalog plus *"cosmological neighbors"*. *Right:* Same as left panel, but as function of absolute magnitude in the R band M_r. Both panels clearly show the gap between real sources (FR Is and ELL) and fake MOCK sources associated with galaxy rich large-scale environments.

5.2.1 DBSCAN + OPTICS

DBSCAN is a density-based clustering algorithm able to located regions of high source density separated by noise, where a cluster is defined as a maximal set of density-connected points. This algorithm is strongly dependant on two parameters: ε, the maximum radius of a neighbor and $MinPts$, the minimum number of points within a ε-neighborhood. To define the size of this ε-neighborhood I adopted the OPTICS algorithm, an implementation of DBSCAN that replaces the ε parameter with a value large enough to order the points of the database, such that points that are spatially closest become neighbors in the ordering.

I applied OPTICS to the dataset with $MinPts$ =5 because this value was high enough to smoothen the curve of the reachability plot. To consider a local maximum as a cluster separation, the average reachability value to the left and to the right must be smaller than 0.75 times the value of the local maximum, the starting ε value for DBSCAN was 75% the mean of all local maxima and again $MinPts = 5$.

The results of applying DBSCAN + OPTICS are represented in Fig. 5.10, where I show that when at least one of the members of the cluster was either a *"cosmological neighbor"* or a *"candidate elliptical galaxy"*, the fraction of FR Is/ELLs lying in galaxy rich environment was higher in comparison with the MOCK population. Using this combination of algorithms for *"cosmological neighbors"* in the left panel of that figure, it is shown that about $\sim$ 60 % of FR Is lie in a rich environment, while the fraction for ELLs residing in galaxy rich environments is about 30 %, lower than FR Is but well above the MOCK population that measured the error. Using the number of clusters for which one of its members was a *"candidate elliptical galaxies"*, the algorithm was much less efficient since the number of FR Is found in galaxy rich environments was only about a $\sim$ 30% for all redshifts, while the fraction of ELLs found in galaxy groups/clusters was of $\sim$ 15% for all redshifts (Fig. 5.10 right panel). There was a decrease of the performance of this method with redshift in detecting groups/clusters of galaxies seen in the left panel of Fig. 5.10, when DBSCAN + OPTICS was ap-

plied to *"cosmological neighbors"*, since in the SDSS the number of sources having a spectroscopic redshift available decreases with redshift. This redshift dependence disappears in the right panel of the same figure because *"candidate elliptical galaxies"* were defined according to a photometric color and at $z < 0.15$ the photometric data from the SDSS are complete at $M_r \sim 20$ (Jin et al., 2014).

In the left panel of Fig. 5.13, I show an example of a cluster detected using DBSCAN + OPTICS for the FR I SDSSJ073014.37+393200.4 at $z_{src} = 0.142$. I represented as connected points all the clusters found using this combination of algorithms, depicting in different colors those clusters composed by normal SDSS galaxies, those clusters hosting at least a *"cosmological neighbor"* and also those for which one of its members was a *"candidate elliptical galaxy"*.

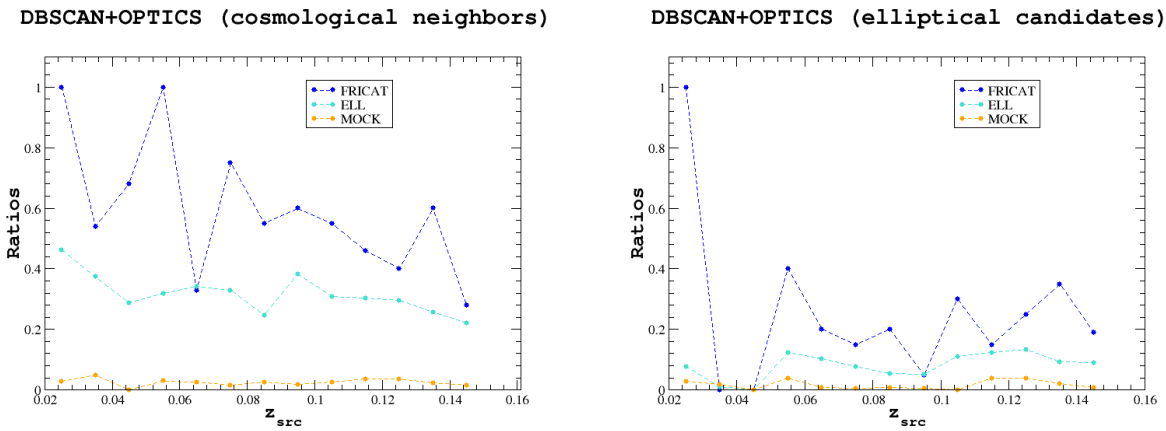

Figure 5.10: *Left:* fraction of FR Is (blue), ELL (cyan) and MOCK(orange) that lie in galaxy rich large-scale environments as function of redshift bin using DBSCAN + OPTICS. In this panel is shown the fraction of clusters hosting at least one *"cosmological neighbor"*. *Right:* Same as left panel, but showing the fraction of the total clusters having at least one *"candidate elliptical galaxy"*.

5.2.2 Voronoi Tesselation

Voronoi Tesselation is a clustering algorithm that partitioning a spatial region, creates the so-called Voronoi diagram on the basis of the distances between sources, so that all points inside the area of a Voronoi cell (substructures of the Voronoi diagram) are closer to that source than to any other. The area of each Voronoi cell is inversely proportional to the density of sources in the neighborhood, thus smaller areas correspond to regions of higher source density. To identify high density regions, I first counted the number of SDSS galaxies within a radius of 2 Mpc and performed 100 simulations of that same region of the sky with sources uniformly distributed, and computed all their normalized areas. The threshold to consider the area of the Voronoi cell as high density was set to the top 5% smaller areas of the simulated fields. In the middle panel of Fig. 5.13 is shown an example of the Voronoi Tessellation algorithm computed for the same source as in the previous section with DBSCAN + OPTICS.

Results using the Voronoi Tesselation algorithm are shown in Fig. 5.11. Again, the fraction of FR Is and ELLs were above the MOCK population that measured the uncertainty, meaning there was an excess of galaxies in the large-scale environment with respect to random positions in the sky for both cases. However, the performance of the algorithm was lower than for DBSCAN + OPTICS.

For clusters having at least one *"cosmological neighbor"* (see left panel of that same figure), about $\sim 40\%$ of the FR Is were found in galaxy groups/clusters, and the fraction decreases with redshift until only $\sim 20\%$ at $z_{src} = 0.15$. Only about 20% of the ELLs were found in galaxy rich large-scale environments. In the right panel of Fig. 5.11 for clusters hosting at least one *"candidate elliptical galaxy"*, the results oscillate around the value $\sim 20\%$ of the FR Is in clusters/groups of galaxies at all redshifts, an around $\sim 15\%$ for the ELLs. The redshift dependance was analogous to the previous section with the algorithm DBSCAN + OPTICS.

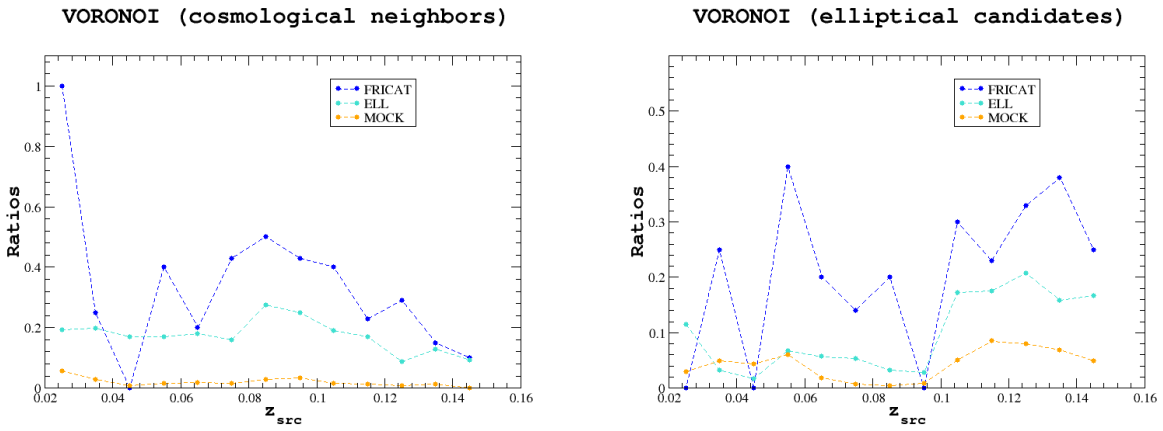

Figure 5.11: *Left:* fraction of FR Is (blue), ELL (cyan) and MOCK(orange) that lie in galaxy rich large-scale environments as function of redshift bin using Voronoi Tesselation. In this panel is shown the fraction of clusters hosting at least one *"cosmological neighbor"*. *Right:* Same as left panel, but showing the fraction of the total clusters having at least one *"candidate elliptical galaxy"*.

5.2.3 Minimum Spanning Tree

The MST is a hierarchical clustering algorithm in which galaxy positions are treated as the nodes of a 2-dimensional graph, over which the tree with the minimal length is constructed. The edges with a length (in this case angular distance) greater than the MST average value are removed, leaving several disconnected clusters, which are further selected by their characteristics. The parameters used for the selection are the *number of nodes* N of the cluster, its *clustering degree* g (i.e., the ratio between the mean edge length in the MST and the local cluster average edge length) and the *magnitude* M (defined as $M = gN$). An example of the MST applied to the same FR I as in previous algorithms for comparison is shown in the right panel of Fig. 5.13.

The fraction of FR Is found in a group/cluster of galaxies is represented in the left panel of Fig. 5.12 for clusters hosting at least one *"cosmological neighbor"*, finding about an 80% of the FR Is in groups/clusters of galaxies at $z < 0.1$, a value that decreases with redshift to values of $\sim 40\%$ at $z = 0.15$, while about 30% of ELLs are found in groups/clusters of galaxies. For clusters hosting a *"candidate elliptical galaxy"* the results are similar as for previous algorithms, oscillating about $\sim 30\%$ - 40% of the FR Is lying in groups/clusters of galaxies, and $\sim 15\%$ for ELLs. The redshift dependance was analogous to the previous sections with the algorithms DBSCAN + OPTICS and Voronoi Tesselation.

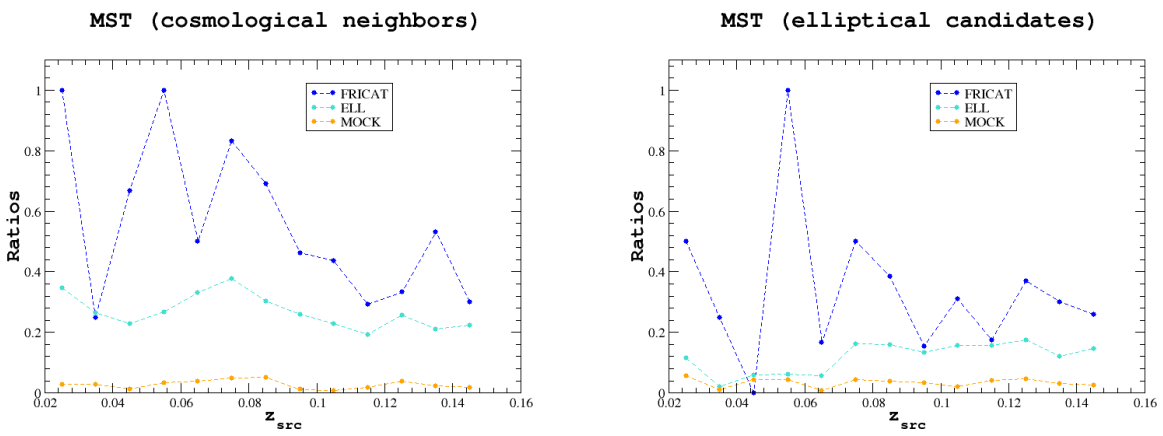

Figure 5.12: *Left:* fraction of FR Is (blue), ELL (cyan) and MOCK(orange) that lie in galaxy rich large-scale environments as function of redshift bin using MST. In this panel is shown the fraction of clusters hosting at least one *"cosmological neighbor"*. *Right:* Same as left panel, but showing the fraction of the total clusters having at least one *"candidate elliptical galaxy"*.

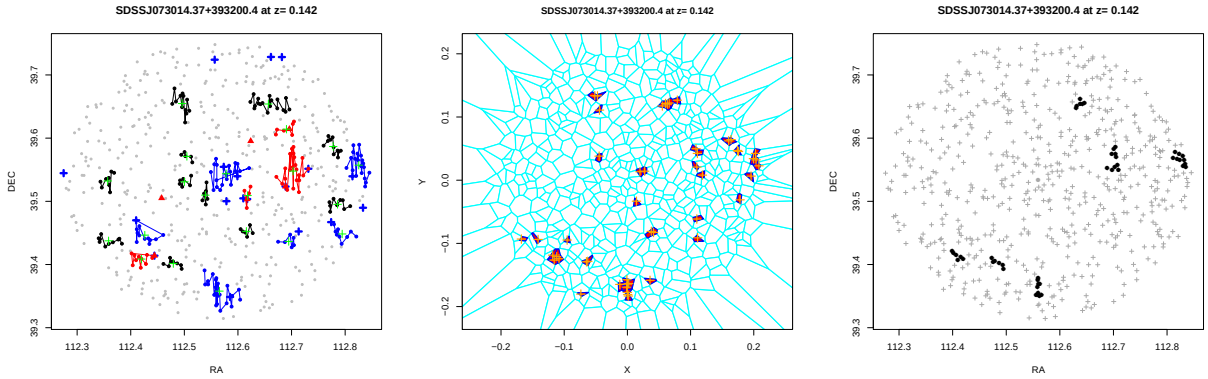

Figure 5.13: *Left:* Example of the application of the combination of algorithms DBSCAN + OPTICS for the FR I SDSSJ073014.37+393200.4. SDSS galaxies are represented by grey points, *"cosmological neighbors"* as red triangles and *"candidate elliptical galaxies"* as blue crosses. Clusters detected using the combination of these two algorithms are represented by connected points: in black those composed by SDSS galaxies, in red those for which one of its members is a *"cosmological neighbors"* and in blue those hosting a *"candidate elliptical galaxy"*. A green cross marks the centroids of each cluster. *Middle:* The Voronoi diagram is shown in cyan, while cells with an area smaller than the top 5% average value computed on 100 replicas of the field are marked in blue. Orange crosses point the location of sources in high-density cells. *Right:* The clusters detected using the MST algorithm. Grey crosses represent the SDSS galaxies and clusters are represented by black points.

5.3 Σ_k nearest neighbor

The Σ_k nearest neighbor analysis technique was developed before large spectroscopic catalogues were available, and foreground and background field galaxies had to be statistically subtracted. The number surface density can be defined as the ratio between the source number k and the projected area:

$$\Sigma_k = \frac{k}{\pi {r_k}^2} \tag{5.1}$$

where r_k is the projected distance between the central galaxy and the k-th nearest neighbor. I used the fifth nearest neighbor density, Σ_5, that uses the projected distance r_5 to a galaxy's 5th nearest neighbor, since this is a value used as beacon to trace the dark matter halo density, that is well correlated with halo mass (Haas et al., 2012; Sabater et al., 2013).

This parameter was computed adopting Σ_5 the distance in kpc between the central galaxy in each field and the 5-th closest *"candidate elliptical galaxy"*. The distribution of the Σ_5 value calculated for FR Is, ELLs and MOCK is reported in Fig. 5.14, and shows that FR Is lie in large-scale environments with higher values of Σ_5 than the MOCK catalog, thus with highest vales of their cluster halo mass.

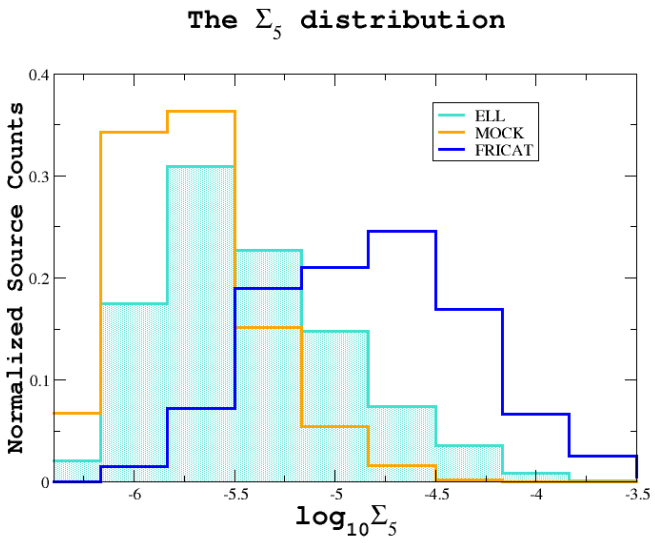

Figure 5.14: Normalized distribution of the fifth nearest neighbor density defined by the Σ_5 parameter for FR Is (blue), ELL (cyan area) and MOCK (orange).

The FR Is lie in clusters having higher mass halos than the MOCK control sample, with the median values for FR Is and the MOCK sample being $log\Sigma_5 = -5.13 \pm 0.51$ and $log\Sigma_5 = -5.76 \pm 0.34$ respectively. Applying the two-sample Kolmogorov-Smirnov test (KS-test) to this environmental metric parameter to quantify the significance of any observed differences between the FRICAT and the MOCK population, they show a difference over a 99% level of confidence. The median for the ELL is $log\Sigma_5 = -5.50 \pm 0.46$, however for this case applying the KS-test for ELL and MOCK, this two populations did not show any difference over a 95% level of confidence.

5.4 Conclusions

In this Chapter I presented a detailed statistical analysis on the large-scale environment of a well-defined and statistically homogeneous sample of FR Is, and compared the results with those obtained for a sample of quiescent elliptical galaxies (ELL), both populations selected lying in the footprint of the SDSS.

To study their clustering environment, I performed a positional cross-match with the catalog T12 of groups/clusters of galaxies with available spectroscopic redshift in the SDSS to see how many of the FR Is/ELLs belong to any of them. Additionally I searched for *"cosmological neighbors"* overdensities in the fields of FR Is/ELLs, i.e., sources for which spectroscopic redshift was available in the SDSS DR9 that were compatible in both projected distance and redshift with the central source, and see if the number of them was sufficient to be considered as a galaxy rich environment. Additionally, I applied several clustering algorithms with different statistics and performances to the photometric sources classified as galaxies in the SDSS DR9, in a radius of 2 Mpc from the central FR I/ELL. For all methods applied, the regions with high source density were computed based on a significance level chosen using a randomly selected MOCK sample. Finally, I studied the distribution for the value of the Σ_5 nearest neighbor, for both FR Is and ELLs populations, comparing them to the same value distribution for the MOCK sample, since this value is related to the dark matter halo density of a galaxy cluster.

This study revealed that many of the FR Is and elliptical galaxies live in galaxy rich large-scale environments, with FR Is lying in systematically higher density environments than quiescent elliptical galaxies (a fraction of about 70% of the total number of FR Is lying in groups clusters of galaxies, compared to $\sim$ 50% of the total number of ELLs.). However, comparing the richness between FR Is and ELLs in the cases when both classes reside in groups/clusters of galaxies, I found no difference between their environments, they lie in clusters of similar richnesses. The deficit in the fraction of ELLs in galaxy rich large-scale environments with respect to FR Is, might be caused by the contamination in the ELL sample from *"disky"* galaxies at low luminosities ($M_r \geq$ -22). *"Disky"* galaxies galaxies are usually found in less rich environments than *"core"* galaxies, and RGs usually are hosted in the latter class.

CHAPTER 6

Environments of BL Lacs

For this analysis I selected those objects classified as BL Lacs in the latest release of the Roma-BZCAT (I did not consider BL Lac candidates since there could be contaminants among them) inside the footprint of SDSS and having a known value for their redshift, that is a total of 59 BL Lacs. Separately, I considered sources classified as BZGs in the latest release of the BZCAT, i.e., sources usually reported as BL Lac objects in the literature but exhibiting a typical elliptical galaxy spectrum, to see if their environments showed any difference from those of BL Lacs. The sample of BZGs selected from the Roma-BZCAT v.5 in the footprint of the SDSS reports 129 sources, all of them with a known value of their redshift.

For the environmental analysis, I downloaded all the optical sources within a circular radius of 2 Mpc from the central BZB/BZG that are detected in the SDSS DR9, having clean photometry and classified as galaxies by the SDSS algorithm (i.e., SDSS flags qmode=1, Q=3 and mode=1).

The sample of BL Lacs was further classified into HBLs and LBLs to unveil the existence of any differences between these two flavours. To classify BL Lacs into HBLs and LBLs, I calculated the ratio between the X-ray and the radio flux (see Giommi et al., 2005; Maselli et al., 2010):

$$\phi_{XR} = \frac{F_X}{S_{1.4}\Delta\nu} \tag{6.1}$$

Both flux values were selected from the 5-th edition of the Roma-BZCAT, where the X-ray flux in the 0.1-2.4 keV band is given in units of W m^{-2} and radio flux density at 1.4 GHz in mJy. To express this ratio in a convenient adimensional number, the radio flux density was multiplied by a bandwidth of $\Delta\nu$ assumed equal to 1 GHz. Typical values of this ratio for LBL sources are about 0.1 or lower, so sources above this value were considered as HBLs and those below as LBLs.

Applying this ratio to the sample with known redshift, most of the BL Lacs were classified as LBLs, 34, while 20 of them were HBLs. It was not possible to calculate this ratio for 5 BL Lacs due to the absence of X-ray flux information.

6.1 Environments BL Lacs

The BL Lacs in the sample are 59 with redshifts ranging between $z_{min} = 0.03002$ and $z_{max} = 0.299$. In parallel a sample of 129 BZGs was also studied, all of them having known redshifts that spanned from $z_{min} = 0.0107$ up to $z_{max} = 0.3$. The analysis applied to BZBs and BZGs was analogous to the one performed to the FR Is, to compare the clustering results between these populations. In Fig. 6.1 is presented an histogram of their redshift, where it is shown that the limiting redshift for FR Is is $z = 0.15$ with a redshift distribution peaking around $z \sim 0.12$, while at redshifts lower than $z < 0.12$ there is a small number of BZBs, since their distribution peaks around $z \sim 0.27$. For BZGs there are very few objects under $z \sim 0.07$, with a distribution peaking at about $z \sim 0.17$ and 0.22.

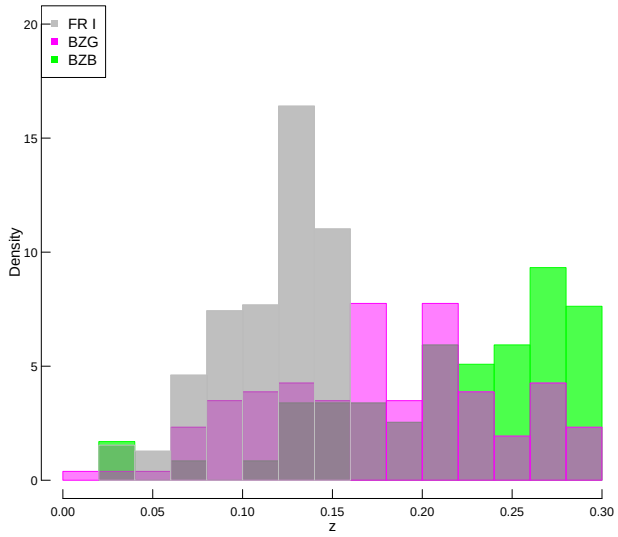

Figure 6.1: Histogram of the redshifts of the samples of FR Is (grey), BZGs (magenta) and BZBs (green).

6.1.1 Positional cross-matches Roma-BZCAT and T12 catalog

The positions of the groups/clusters of galaxies from the T12 catalog were cross-matched with the positions of the 19 BL Lacs at $z < 0.2$, the redshift limit of T12, to find out how many of the BL Lacs could belong to any of those clusters. The conditions that needed to be satisfied for a BZB/BZG to be associated with a group/cluster of galaxies from this catalog were the same that in the previous Chapter for FR Is: for groups/clusters of at least 4 members in the T12 catalog, the projected distance d_{proj} between the central BZB/BZG and the position of the center of the group/cluster reported in T12 must be smaller than 2 Mpc, and their redshift difference $\Delta z < 0.005$. For groups of galaxies of richness 2 or 3 in the T12, there must be a minimum of 2 groups satisfying these constraints to consider a BZB/BZG associated with a group or a cluster of galaxies.

From the cross-match with the T12 catalog, 6 BL Lacs out of 19 were found to be associated with a T12 group/cluster of galaxies according to the conditions previously enunciated. These objects were 5BZBJ1104+3812, 5BZBJ1117+2014, 5BZBJ1203+603, 5BZBJ1428+4240, 5BZBJ1442+1200 and 5BZBJ1653+3945.

The richness of the closest associated T12 cluster for 5BZBJ1203+6031 was only $N_{gal} = 3$, but there were other 2 clusters at $\Delta z < 0.005$ lying within a projected distance of 2 Mpc from the central source, therefore they were associated with the BZB, so this was one of the cases for which

the algorithm FoF used to build the T12 catalog split the same cluster in several. The same situation occurred for the source 5BZBJ1428+4240, the closest cluster detected had only 2 members according to T12, but 3 clusters were found nearby and at similar redshifts, each one with richness $N_{gal} = 2$. The source was considered to inhabit a galaxy rich environment.

The same analysis was performed for the 77 out of 129 BZGs from the sample at $z < 0.2$ thus inside the redshift limit of T12, using the exact same restrictions for considering a source belonging to a T12 group/cluster of galaxies, and I found that 32 of them were compatible with these conditions.

6.1.2 Positional cross-matches Roma-BZCAT and GMBCG catalog

I used the GMBCG catalog to discover how many of the sources in the samples of BZBs and BZGs were compatible with being the BCG of a cluster. A source was considered a BCG if the redshift between the source and that reported in the GMBCG catalog was $\Delta z < 0.005$ and the projected distance between them was smaller than 1 kpc. None of the BZBs of the sample satisfied this conditions, thus none of them could be considered a BCG. However, I found 3 BZGs satisfying these conditions that could be considered BCGs: 5BZGJ1028+0555, 5BZGJ1647+2909 and 5BZGJ1717+2931.

6.1.3 Cosmological neighbors

Sources for which a spectroscopic redshift was available in the SDSS DR9, lying within a projected distance of 2 Mpc and having a redshift difference of $\Delta z < 0.005$ from that of the central BZB/BZG were called *"cosmological neighbors"*, analogously to the analysis of FRICAT performed in Chapter 5. A BZB or a BZG at a particular redshift were considered to be in a galaxy rich environment (*"cosmological neighbors"* overdensity) with this particular method, when they were surrounded by a number of *"cosmological neighbors"* higher than 95% of the MOCK sources inside their same redshift bin.
The $u - r$ and the $g - z$ optical colors were computed for all the SDSS DR 9 sources downloaded within 2 Mpc from the central BZB/BZG, to search for those having optical colors compatible with elliptical galaxies at the same redshift of the central object, an they were defined as *"candidate elliptical galaxies"*.

For only 6 out of 59 BL Lacs *"cosmological neighbors"* overdensities were found: 5BZBJ0837+1458, 5BZBJ1117+2014, 5BZBJ1104+3812, 5BZBJ1419+5423, 5BZBJ1442+1200 and 5BZBJ1653+3945. Their fields are shown in Fig. 6.2. There were areas of the sky for 5BZBJ1104+381 not covered by the SDSS footprint, shown as blank areas in this figure. However, this source was found in a rich environment separately by the two methods so far reported in this Chapter, i.e., both associated with a T12 cluster of galaxies of richness $N_{gal} = 13$, and having 5 *"cosmological neighbors"* inside a radius of 500 kpc from the central BZB. For the source 5BZBJ1653+3945, only a small part of the sky was covered by the SDSS, less than a physical distance of 500 kpc and not centered on the source, as shown in the bottom right part of this figure. Despite the small part covered, it was possible to find this source in a rich environment separately by this two methods, i.e., it was associated cluster of galaxies of richness $N_{gal} = 10$ reported in the T12 catalog, and also it had 6 *"cosmological neighbors"* inside 500 kpc. In the case of BZGs, 34 sources were found in a galaxy rich environment using *"cosmological neighbors"* overdensities, about the 26% of the total BZG sample.

The left panel of Fig. 6.3 shows the fraction of BZGs and FR Is that were found to be associated with a group/cluster of galaxies in the T12 catalog according to the conditions previously discussed. FR Is were reported until the limiting redshift of the used sample (FRICAT, $z < 0.15$) while BZBs and BZGs were analyzed until the limiting redshift of the T12 catalog, $z = 0.2$. Since

only 6 BZBs were found to be associated with a group/cluster of galaxies with the T12 catalog, they are not represented in this plot. The number of sources found associated with clusters decreases with redshift, because the efficiency of the T12 catalog in finding clusters decreases with redshift too. In the right panel of the same figure I show the fraction of FR Is and BZGs found in a rich environment using *"cosmological neighbors"* overdensities. Again, BZBs were not plotted because only 6 BL Lacs were found in a galaxy rich environment using only this method. For both figures, at $z < 0.1$ there are strong fluctuations between two consecutive redshift bins because the number of BZGs is very low. It seems that BZGs lie in significantly richer environments than a random population of MOCK sources, but not as rich as FR Is. The fraction of sources found in clusters using *"cosmological neighbors"* overdensities decreases with redshift, since in the SDSS the number of sources having available spectroscopic redshift decreases with redshift too.

Using the *"cosmological neighbors"* overdensities method, I compared both the environments of BZBs and BZGs with those for FR Is. In the left panel of Fig. 6.4 it is shown the number of *"cosmological neighbors"* N_{cn} inside 2 Mpc as function of the redshift of the central source z_{src}. The average number of *"cosmological neighbors"* was computed in the right panel of Fig. 6.4 inside 2 Mpc as function of redshift, to highlight the difference between populations. The median for the BZBs is $< N_{cn\ BZB} >_{median} = 0$ or $< N_{cn\ BZB} >_{mean} = 1.9$ and for BZGs is $< N_{cn\ BZG} >_{median} = 1$ or $< N_{cn\ BZG} >_{mean} = 4.1$, while the average for FR Is was $< N_{cn\ FRI} >_{median} = 7$ or $< N_{cn\ FRI} >_{mean} = 11.1$.

6.2 Clustering algorithms

To look for regions of high density among SDSS DR9 sources classified as galaxies and having a clean photometry around a 2 Mpc radius from each BZB/BZG, I adopted several clustering algorithms that are complementary to each other. In Chapter 3 there was a description of the algorithms, while in Chapter 5 there was a detailed explanation of the application to the sample of FR Is, analogous to the analysis of BZBs and BZGs. For a source to be considered in a high density region, one of the members of the cluster found by the algorithm must be either a *"cosmological neighbor"* or a *"candidate elliptical galaxy"*. A region was considered of high density when, using the same algorithm to the MOCK sample, less than 5% of the sources at the same redshift bin lied in such a rich environment.

6.3 Results

Finally, a BZB/BZG was considered to be in a group/cluster of galaxies when it satisfied one of the following conditions:

- The BZB/BZG was found to lie in a galaxy rich environment using *"cosmological neighbors"* overdensities.
- The BZB/BZG was found to be associated with a group/cluster of galaxies with the T12 catalog plus at least two of the algorithms found a high density region, for which one of the members was a *"cosmological neighbor"* or a *"candidate elliptical galaxy"*, associated with the central source.

For BZBs, 7 sources were found to be in a galaxy rich large-scale environment according to the previous conditions. A summary of all the BZBs studied and the results is given in Table 6.1. Here it

is reported the name in the Roma-BZCAT v.5 together with their redshift, the class (LBL or HBL), a flag when the BZB was detected at TeV, a flag when the object was inside a group/cluster of galaxies and a flag when the cluster was found for each method: positional cross-match with a group/cluster of the T12 catalog, *"cosmological neighbors"* overdensities, DBSCAN+OPTICS, Voronoi Tesselation and MST.

Only 7 BZBs out of 59 were found in a galaxy/cluster of galaxies, about a 12% and the total number of BZBs and these objects were: 5BZBJ0837+1458 at $z = 0.278$, 5BZBJ1104+3812 at $z = 0.03002$, 5BZBJ1117+2014 at $z = 0.138$, 5BZBJ1653+3945 at $z = 0.033$, 5BZBJ1419+5423 at $z = 0.153$, 5BZBJ1442+1200 at $z = 0.163$ and 5BZBJ1428+4240 at $z = 0.129$. From these objects, 6 of them were classified as HBLs and 1 is a LBL.

For the BZGs the ratio of sources found in clusters according to the conditions previously described was higher than for BZBs, since 43 out of 129 sources were found to lie in galaxy rich large-scale environments, 1/3 of the total number of BZGs. A summary of all the BZGs studied is reported in Table 6.2, describing the Roma-BZCAT v.5 name, redshift, a flag when the object satisfied the conditions to be inside a group/cluster of galaxies, a flag when the object was found in a group/cluster of galaxies by T12 positional cross-matches, a flag when the object was found in a group/cluster of galaxies by *"cosmological neighbors"* overdensities, a flag when the source was compatible with being a BCG, and a flag when the cluster was found using the algorithms: DBSCAN+OPTICS, Voronoi Tesselation and MST.

Fig. 6.5 shows the fraction of BZGs considered to reside in a group/cluster of galaxies for each redshift bin according to the conditions previously described, comparing them to the ratio of FR Is found in rich environments in Chapter 5. Since only 7 BZBs were found in clusters, they are not represented in this plot. Here it is shown that about 40 % of BZGs inhabit galaxy rich ambients, a fraction lower than FR Is, for which the lowest fraction was found to be 60%. Since for two of the methods selected the effectivity decreases with redshift, i.e., T12 positional cross-matches and *"cosmological neighbors"* overdensities, here the trend also decreases with z. At lower redshift the ratios of BZGs show a strong fluctuation because of their small number at $z < 0.1$.

6.4 Σ_k nearest neighbor

The Σ_k nearest neighbor analysis technique was applied, defined as the ratio between the source number k and the projected area $\pi {r_k}^2$, being r_k the projected distance between the central galaxy and the k-th nearest neighbor. Since the analysis was parallel to that for FR Is, I used again the distance to the fifth neighbor as an indicator of the density of the dark matter halo in a cluster of galaxies. The parameter Σ_5 was computed using the projected distance to the fifth closest *"candidate elliptical galaxy"*. The distribution of the analysis for both BZBs and BZGs is given in Fig. 6.6, together with the distribution of the same parameter for FR Is and the MOCK catalog for comparison. The median value for the distribution was calculated to highlight differences between the populations: for FR Is was $log\Sigma_5 = -5.13 \pm 0.51$, while for BZBs was $log\Sigma_5 = -5.839033 \pm 0.51$ and for BZGs was $log\Sigma_5 = -5.51298 \pm 0.56$. That distribution shows that BZBs lie in lower halo mass environments than FR Is, since the KS-test was applied to compare the values of Σ_5 of BZBs and BZGs with the FR Is, resulting FR Is and BZBs showed a difference over a 94% of confidence, while BZGs and FR Is did not show a difference in the distribution of the Σ_5 value over a 90% interval.

6.5 BL Lacs previously studied in the literature

For the BL Lac 5BZB J0757+0956 (a.k.a. PKS 0754+100), Pesce et al. (1995) found a slightly excess of galaxies with respect to the background. Their study was performed using a tentative value for its redshift of $z = 0.66$ that is now known to be wrong, since this source now has been found to be at $z = 0.266$ (Carangelo et al., 2003). Only one *"cosmological neighbor"* was found and it is beyond 1 Mpc (see top panel Fig. 6.7), also none of the cluster algorithms found it in a cluster of galaxies. In the bottom panel of the same figure it is shown the results for the Voronoi Tesselation algorithm. This BL Lac was not found to reside in a galaxy rich large-scale environment.

5BZB J0831+0429 or PKS 0829+046 is a BL Lac at $z = 0.174$ that, when studied by Pesce et al. (1994), was not found to be in a group/cluster or galaxies. Here I found 4 *"cosmological neighbors"*, i.e., 4 sources with a difference in the spectroscopic redshift from the central source of $\Delta z < 0.005$ and inside a 2 Mpc circular region, one of them inside 1 Mpc as seen in the top panel of Fig. 6.8. This number of sources was not statistically higher than a random population of quiescent elliptical galaxies according to the analysis performed in the MOCK sample. In addition only one of the algorithms found the source to be in a cluster of galaxies, DBSCAN + OPTICS, shown in the bottom panel of Fig. 6.8. The source was not found to inhabit a galaxy rich large-scale environment, in agreement with Pesce et al. (1994).

Wurtz et al. (1997) did not find the BL Lac 5BZB J1221+2813 (a.k.a S3 1219+28) at $z = 0.102$ to be in a group/cluster of galaxies. My results are in agreement with what found by the previous study since only 2 *"cosmological neighbors"* were found inside a 2 Mpc radius (see top panel of Fig. 6.9), not enough to consider it a group of galaxies. Besides, none of the algorithms found any galaxy enhancement for this source, so this BL Lac does not reside in a galaxy rich large-scale environment. An example of the application of the MST algorithm is shown in the bottom panel of the same figure.

The object 5BZB J1224+2436 (a.k.a. MS 1221.8+2452) at $z = 0.218$ was studied twice, (Wurtz et al., 1997; Pesce et al., 2002) and both times the authors did not find significant galaxy enhancement, concluding it is not in a cluster of galaxies . I did not find any *"cosmological neighbors"* at a similar redshift in its field, as shown in the top left panel Fig. 6.10. Additionally, none of the

Table 6.1: Sample BZBs in the Roma-BZCAT in the SDSS DR9.

Roma-BZCAT name	z	class	TeV	inside	T12 cross-match	*"cosmological neighbors"*	DBSCAN+OPTICS	Voronoi Tesselation	MST
5BZBJ0737+2846	0.272	LBL							
5BZBJ0757+0956	0.266	LBL							
5BZBJ0809+5218	0.138	HBL	yes						
5BZBJ0818+2814	0.226	LBL							
5BZBJ0831+0429	0.174	LBL					yes		
5BZBJ0837+1458	0.278	HBL		yes		yes	yes	yes	yes
5BZBJ0847+1133	0.199	HBL	yes						
5BZBJ0854+6218	0.267	LBL							
5BZBJ0857+0135	0.281	LBL							
5BZBJ0902+4544	0.289								
5BZBJ0909+2311	0.223	LBL							
5BZBJ0909+3106	0.272	LBL						yes	yes
5BZBJ0930+4950	0.187	HBL							
5BZBJ0945+5757	0.229	LBL							
5BZBJ1015+4926	0.212	HBL	yes						
5BZBJ1024+2332	0.165	LBL							
5BZBJ1025+0402	0.208	LBL					yes		
5BZBJ1051+0103	0.265	LBL							
5BZBJ1058+5628	0.143	LBL					yes		
5BZBJ1104+3812	0.03002	HBL	yes	yes	yes	yes	yes		yes
5BZBJ1111+3452	0.212	HBL						yes	
5BZBJ1117+2014	0.138	HBL		yes	yes	yes			yes
5BZBJ1136+6737	0.136	HBL	yes						
5BZBJ1140+1528	0.244	LBL					yes	yes	
5BZBJ1154-0010	0.254	HBL					yes	yes	
5BZBJ1202+4444	0.297	LBL							
5BZBJ1203+6031	0.065	LBL			yes		yes		
5BZBJ1204+1145	0.296	LBL							
5BZBJ1219-0314	0.299	LBL							
5BZBJ1221+2813	0.102	LBL							
5BZBJ1221+3010	0.184	HBL	yes						
5BZBJ1224+2436	0.219	LBL	yes					yes	
5BZBJ1231+1421	0.256	HBL							
5BZBJ1231+6414	0.163	LBL							
5BZBJ1237+6258	0.297	HBL							
5BZBJ1251+1039	0.245	HBL							
5BZBJ1257+2412	0.141	HBL							yes
5BZBJ1258+6120	0.224								
5BZBJ1325+6621	0.21	LBL							
5BZBJ1331-0022	0.243	LBL							
5BZBJ1336+2319	0.267	LBL							
5BZBJ1337+0035	0.299	LBL							
5BZBJ1341+5514	0.207	LBL							
5BZBJ1354+0622	0.276								
5BZBJ1402+1559	0.244	LBL							
5BZBJ1417+2543	0.237	HBL							
5BZBJ1419+5423	0.153	LBL		yes		yes	yes	yes	yes
5BZBJ1428+4240	0.129	HBL	yes	yes	yes		yes	yes	yes
5BZBJ1442+1200	0.163	HBL	yes	yes	yes	yes	yes		yes
5BZBJ1508+2709	0.27	LBL							
5BZBJ1534+3715	0.143	LBL					yes	yes	
5BZBJ1535+3922	0.257	LBL							
5BZBJ1554+2011	0.222	LBL							
5BZBJ1605+5421	0.212	HBL							
5BZBJ1606+1345	0.29	LBL							
5BZBJ1617+4106	0.267	LBL							
5BZBJ1632+1758	0.287								
5BZBJ1651+4212	0.269								
5BZBJ1653+3945	0.033	HBL	yes	yes	yes				

Column description. (1): BL Lac name in the Roma-BZCAT v.5, (2): redshift, (3): class (LBL/HBL), (4): is the BZB observed in the TeV yes/no, (5): is the BL Lac in a cluster yes/no, (6): is the BZB in cluster yes/no according to: T12 cross-match, (7): *"cosmological neighbors"*, (8): DBSCAN + OPTICS, (9): Voronoi Tesselation, (10): MST.

Table 6.2: Sample BZGs in the Roma-BZCAT in the SDSS DR9.

Roma-BZCAT name	z	inside	T12 cross-match	*"cosmological neighbors"*	BCG	DBSCAN + OPTICS	Voronoi Tesselation	MST
5BZGJ0737+3517	0.21					yes	yes	
5BZGJ0741+3205	0.179							
5BZGJ0745+3312	0.22	yes				yes	yes	
5BZGJ0748+2115	0.263							
5BZGJ0749+2313	0.175							
5BZGJ0751+1730	0.187	yes	yes	yes		yes	yes	yes
5BZGJ0751+2913	0.194							
5BZGJ0753+2921	0.161							yes
5BZGJ0754+3910	0.096							
5BZGJ0756+3834	0.216	yes		yes		yes	yes	yes
5BZGJ0758+2705	0.099	yes	yes	yes		yes	yes	yes
5BZGJ0809+3122	0.296						yes	
5BZGJ0809+3455	0.083	yes	yes	yes		yes	yes	yes
5BZGJ0810+2846	0.272	yes				yes	yes	
5BZGJ0810+4911	0.115	yes	yes	yes		yes	yes	yes
5BZGJ0820+4853	0.133	yes	yes	yes		yes	yes	yes
5BZGJ0823+1524	0.167							
5BZGJ0828+4153	0.226							
5BZGJ0829+1754	0.089	yes	yes	yes		yes	yes	yes
5BZGJ0831+4608	0.131	yes		yes		yes		yes
5BZGJ0831+5400	0.062	yes	yes	yes				
5BZGJ0834+5534	0.242						yes	
5BZGJ0835+1517	0.169							
5BZGJ0839+4015	0.194					yes		
5BZGJ0850+3455	0.145	yes	yes	yes				
5BZGJ0850+4036	0.267							
5BZGJ0856+5418	0.259	yes				yes	yes	yes
5BZGJ0903+4055	0.188						yes	yes
5BZGJ0905+4705	0.174							
5BZGJ0906+4124	0.0275	yes	yes	yes		yes		yes
5BZGJ0906+4636	0.0848			yes				
5BZGJ0912+1555	0.212						yes	
5BZGJ0912+4235	0.266	yes				yes	yes	yes
5BZGJ0912+5320	0.102	yes	yes					
5BZGJ0916+5238	0.19	yes	yes				yes	
5BZGJ0927+5327	0.201							
5BZGJ0927+5545	0.221	yes				yes		
5BZGJ0932+3630	0.154							
5BZGJ0940+6148	0.211							
5BZGJ0946+5819	0.147							
5BZGJ0948+5535	0.118							
5BZGJ0950+1804	0.154							
5BZGJ1012+3932	0.171							
5BZGJ1018+3128	0.161							
5BZGJ1020+6250	0.25							
5BZGJ1022+5124	0.142							
5BZGJ1028+0555	0.234				yes			
5BZGJ1028+1702	0.169							
5BZGJ1033+4222	0.211					yes		
5BZGJ1041+3901	0.21							
5BZGJ1052+4241	0.136	yes	yes					
5BZGJ1053+4929	0.14	yes		yes				
5BZGJ1056+0252	0.236							
5BZGJ1103+0022	0.275							
5BZGJ1105+3946	0.099							
5BZGJ1105+4653	0.112	yes	yes	yes		yes	yes	yes
5BZGJ1108+0202	0.157							
5BZGJ1108-0149	0.106							
5BZGJ1121+4314	0.185						yes	
5BZGJ1124+5133	0.235							
5BZGJ1132+0515	0.101							
5BZGJ1136+2550	0.156	yes	yes	yes		yes		yes
5BZGJ1145-0340	0.167							
5BZGJ1147+2205	0.276							
5BZGJ1147+3501	0.063	yes	yes	yes				

Roma-BZCAT name	z	inside	T12 cross-match	*"cosmological neighbors"*	BCG	DBSCAN + OPTICS	Voronoi Tesselation	MST
5BZGJ1147+2205	0.276							
5BZGJ1147+3501	0.063	yes	yes	yes				
5BZGJ1148+5924	0.0107	yes	yes	yes		yes		yes
5BZGJ1150+5528	0.139	yes	yes	yes		yes		
5BZGJ1154+0238	0.211							
5BZGJ1154+1225	0.0812	yes	yes	yes		yes		yes
5BZGJ1156+4238	0.172					yes		yes
5BZGJ1157+2822	0.3							
5BZGJ1158+2450	0.202							
5BZGJ1200+4758	0.27					yes		
5BZGJ1201-0007	0.165	yes	yes			yes		
5BZGJ1201-0011	0.164	yes	yes			yes	yes	yes
5BZGJ1215+0732	0.136							
5BZGJ1216+0929	0.0935	yes	yes	yes				yes
5BZGJ1221+0821	0.132					yes		yes
5BZGJ1221+4742	0.21							
5BZGJ1223+4650	0.261							
5BZGJ1226+2604	0.176							
5BZGJ1233+5026	0.207							
5BZGJ1238+5406	0.224							
5BZGJ1243+5212	0.2							
5BZGJ1253+0326	0.066	yes	yes	yes				
5BZGJ1301+4634	0.205					yes	yes	
5BZGJ1323+0439	0.224						yes	yes
5BZGJ1324+5739	0.115	yes	yes	yes		yes	yes	yes
5BZGJ1326+1229	0.204					yes	yes	yes
5BZGJ1331+5655	0.27							
5BZGJ1341+3716	0.175	yes	yes	yes				yes
5BZGJ1341+3959	0.172	yes	yes	yes		yes	yes	yes
5BZGJ1346+2440	0.167							
5BZGJ1348+0756	0.25							
5BZGJ1350+0940	0.133	yes	yes	yes		yes	yes	yes
5BZGJ1353+3741	0.216							
5BZGJ1404+2701	0.138							
5BZGJ1407+2827	0.0766							
5BZGJ1413+4339	0.0899	yes	yes	yes		yes	yes	yes
5BZGJ1414+3430	0.275							
5BZGJ1424+3705	0.29							
5BZGJ1427+3908	0.165							
5BZGJ1427+5409	0.106							
5BZGJ1428+3912	0.258							
5BZGJ1435+5815	0.299							
5BZGJ1435-0055	0.285							
5BZGJ1444+6336	0.298							
5BZGJ1449+2746	0.227							
5BZGJ1502+2528	0.178						yes	yes
5BZGJ1504-0248	0.217							
5BZGJ1506+0219	0.22	yes				yes	yes	
5BZGJ1510+3335	0.114	yes	yes	yes		yes	yes	yes
5BZGJ1512+0203	0.22							
5BZGJ1515+2426	0.228							
5BZGJ1516+0015	0.0525					yes	yes	
5BZGJ1516+2918	0.13					yes		
5BZGJ1518+4045	0.065	yes	yes	yes				yes
5BZGJ1531+0852	0.159							
5BZGJ1532+3016	0.0653	yes	yes	yes				yes
5BZGJ1539+4143	0.119			yes				
5BZGJ1604+3345	0.177							
5BZGJ1616+3756	0.202							
5BZGJ1624+3726	0.199							
5BZGJ1628+2527	0.22							
5BZGJ1637+4547	0.192	yes		yes		yes	yes	yes
5BZGJ1643+2131	0.154	yes	yes	yes		yes	yes	yes
5BZGJ1644+4546	0.225							
5BZGJ1647+2909	0.132	yes	yes	yes	yes	yes	yes	yes
5BZGJ1717+2931	0.276	yes		yes	yes	yes		yes

Column description. (1): BL Lac name in the Roma-BZCAT v.5, (2): redshift, (3): is the BL Lac in a cluster yes/no, (4): is the BZB in cluster yes/no according to: T12 cross-match, (5): *"cosmological neighbors"*, (6): is a BCG yes/no, (7): DBSCAN + OPTICS, (8): Voronoi Tesselation, (9): MST.

clustering algorithms find any group/cluster of galaxies for this BL Lac.

Wurtz et al. (1997) found a little galaxy enhancement in the environment of 5BZB J1231+6414 (a.k.a. MS 1229.2+6430), a BL Lac at $z = 0.164$. I did not confirm their results, since only one *"cosmological neighbor"* was found in the field and it is beyond 1 Mpc as seen in the top middle panel of Fig. 6.10, not enough to consider it in a group/cluster of galaxies. Algorithms did not confirm their result either since none of them found any significant clustering degree above the considered threshold for a MOCK population.

The BL Lac at $z = 0.297$, 5BZB J1237+6258 (a.k.a. MS 1235.4+6315) was not found to be in a galaxy rich large-scale environment by Wurtz et al. (1997), a result that I now confirm because only one *"cosmological neighbor"* was found in the field and it was beyond 1 Mpc as seen in the top right panel of Fig 6.10 and none of the algorithms found any galaxy enhancement. The object was not found to reside in a galaxy rich large-scale environment.

Pesce et al. (1994) and Wurtz et al. (1997) investigated the environment for the BL Lac 5BZB J1402+1559 (a.k.a. PKS 1400+162), and none of them found it to be in a group/cluster of galaxies. It was not possible to cross-match its environment with the T12 catalog since the value for its redshift is $z = 0.244$ (T12 limiting redshift $z = 0.2$). I did not find any *"cosmological neighbors"* in a circular region of 2 Mpc as shown in the middle left panel of Fig. 6.10, and none of the algorithms found it to be in an environment with any galaxy enhancement. It was not found in a galaxy rich large-scale environment, in agreement with previous studies.

The object 5BZBJ1417+2543, (a.k.a. 1E 1415.6+2557) is a BL Lac at $z = 0.237$ studied several times in the past by Romanishin (1992); Wurtz et al. (1997) and Gladders et al. (1997). The first two studies did not find any galaxy enhancement, while the last one found it was consistent with being in a compact group. It was not possible to perform the cross-match with the T12 since the redshift of the BL Lac is higher than this catalog. However, the number of *"cosmological neighbors"* was only one (see middle middle panel in Fig. 6.10) and none of the clustering algorithms found any galaxy enhancement above the mock threshold, suggesting that this source is not in a group/cluster of galaxies. This result confirms what previously found by Romanishin (1992) and Wurtz et al. (1997).

5BZB J1419+5423 (a.k.a. PG 1418+546) is a BL Lac at $z = 0.153$ found to be in an low-density environment by Wurtz et al. (1997). I found 4 *"cosmological neighbors"* for this object inside 2 Mpc as seen in the middle right panel of Fig. 6.10, a number statistically significant according to the analysis performed at this redshift bin to the MOCK catalog. In addition, it was found to be in a group of galaxies by two algorithms, Voronoi Tesselation and DBSCAN + OPTICS. For this case, the BL Lac was found to inhabit a group/cluster of galaxies and my results do not agree with what found by the previous work.

The environment of the BL Lac of galactic type 5BZG J1444+6336 (a.k.a. MS 1443.5+6349) at $z = 0.299$ was studied by Wurtz et al. (1997), not finding any galaxy enhancement. I confirmed their results, since there was only one source in the 2 Mpc field with a $\Delta z < 0.005$ (i.e. *"cosmological neighbor"*, see bottom left panel of Fig. 6.10), not enough to consider it in a group of galaxies. Moreover, none of the algorithms found any clustering around the source, the BL Lac was not found to inhabit a galaxy rich large-scale environment.

5BZB J1554+2011 (a.k.a. 1ES 1552+203) at $z = 0.222$ was not found in a group/cluster of galaxies by Wurtz et al. (1997). I confirmed their results, not finding any *"cosmological neighbors"* in a circular region of 2 Mpc (see bottom middle panel of Fig. 6.10) or any galaxy enhancement using clustering algorithms. The BL Lac was not found to reside in a galaxy rich large-scale environment.

5BZB J1653+3945 is the closest BL Lac known to date. It lies at $z = 0.033$ and it is also known as Mrk 501. Wurtz et al. (1997) did not find any galaxy enhancement, opposed that my result, since I found 6 *"cosmological neighbors"* inside a radius of 500 kpc as shown in the bottom right panel of Fig. 6.10. The field for this BL Lac was incomplete, so it was not possible to assure the correct performance of the algorithms and they were not applied in this case. The source was found in a galaxy rich large-scale environment.

6.6 Conclusions

FR Is were predominantly found in clusters as seen in Chapter 5 being their lowest fraction 60% at the highest redshift bin, while BL Lacs tend to avoid high-density large-scale environments since only a few number of them were found in a group/cluster of galaxies (12% of the total sample of BZBs). This results are in contradiction to the expectations of the Unified Model, in which BL Lacs are FR I RGs observed close to the axis of a relativistic jet, so this new line of evidence suggest that a critical reexamination of the Unification Scenario is required for these two classes .

It has been suggested by previous authors that BL Lacs might be associated with FR IIs instead of FR Is (Owen et al., 1996; Wurtz et al., 1997), since FR IIs are typically found in regions of low galaxy density (see e.g. Hill & Lilly, 1991; Miller et al., 2002), so their environments show more similarities than those of BL Lacs and FR Is. Additionally, recent studies of AGN clustering show discrepancies between the environments of obscured and unobscured AGNs, suggesting that the observed difference between obscured and unobscured AGNs does not only relate to their relative geometry, but also to different accretion models or to a difference of their host halo assembling histories. In this scenario, obscured AGNs represent an early evolutionary phase, before the growing black hole produces a high enough accretion luminosity to expel the surrounding material (see Hopkins et al., 2008; Hickox et al., 2009). Following their model, it would be possible that FR Is and BL Lacs constitute two different phases of the same evolutionary path, in which FR Is may represent the earlier phase.

The situation was different for BL Lacs of galactic type, since they tend to lie in significantly richer environments than BZBs, being about 26% of all BZGs in groups/clusters of galaxies, a fraction richer than BL Lacs but not as rich as FR Is. This might explain the results obtained by Muriel (2016), he found a high rate of BL Lac objects in groups but his sample is dominated by BL Lacs of galactic type (96 out of 121 objects in their sample were BL Lacs of galactic type).

From the 7 BL Lacs found in a rich-galaxy large-scale environment, 6 of them were HBLs and 1 was a LBL, even though HBLs were only 33% of the BZBs in the total sample. It has been suggested that the lower luminosity in HBLs with respect to LBLs is due to a reduction of the jet power in the former class, because they live in denser environments that are more efficient in decelerating them (Donato et al., 2003). The results in this present work support their claim, but the sample is too small to reach strong conclusions.

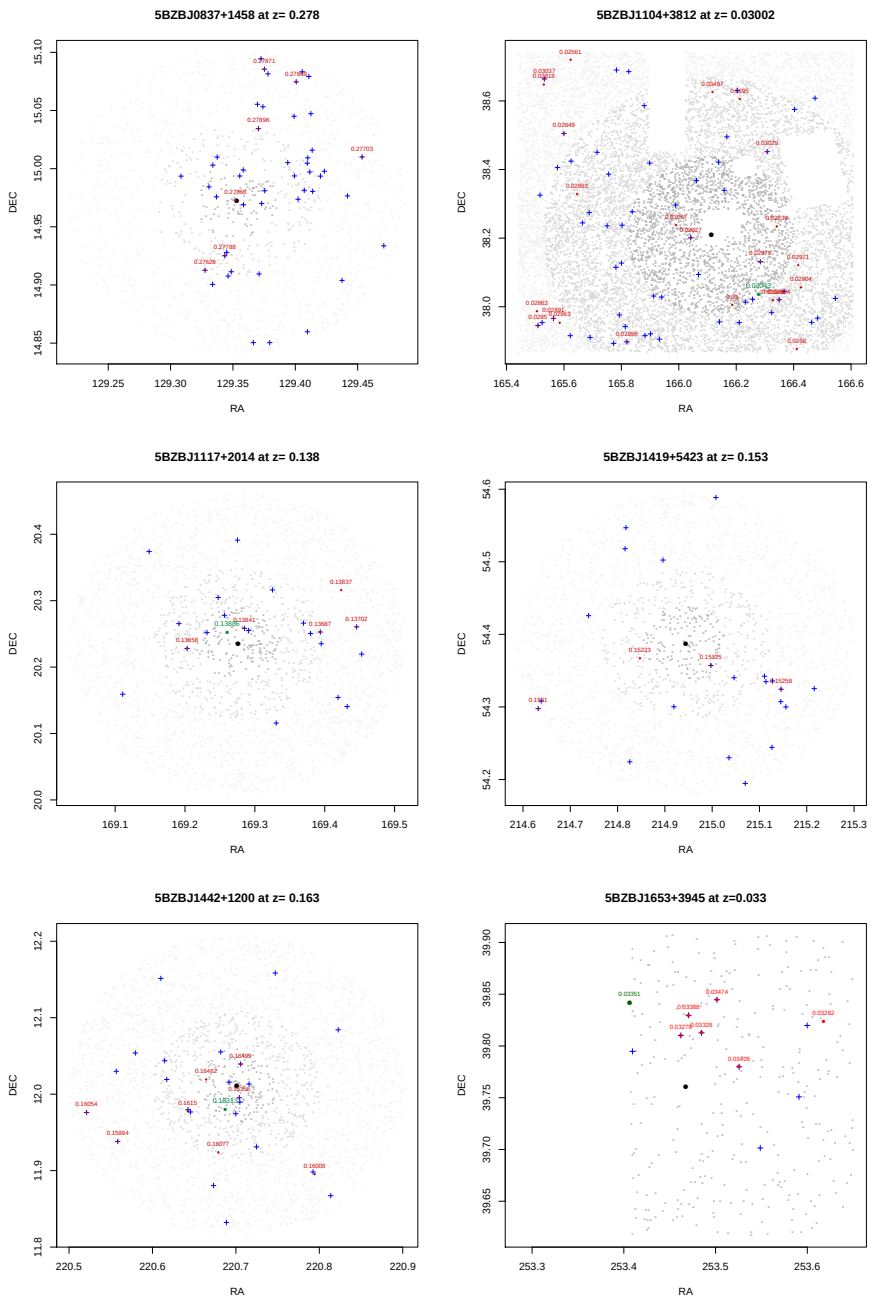

Figure 6.2: *Top left:* all the SDSS galaxies within a circular region of 2 Mpc from 5BZBJ0837+1458 are plotted in decreasing intensities of grey indicating those inside 500 kpc, 1 Mpc and 2 Mpc respectively. *"Cosmological neighbors"* are represented in red together with their redshifts and blue crosses mark *"candidate elliptical galaxies"*. *Top right:* Same as top left figure, but here for 5BZBJ1104+3812 a green point indicates the position of the group from the T12 catalog associated with this BZB. For this source there are parts of the sky that are not covered by the SDSS, shown as blank areas in the figure. *Middle left:* 5BZBJ1117+2014 is also associated with a cluster of galaxies using the T12 catalog, as indicated by the green point. *Middle right:* 5BZBJ1419+5423 has previously been studied in the literature. *Bottom left:* Same as top left figure for 5BZBJ1442+1200. *Bottom right:* Only a small part of the sky for 5BZBJ1653+3945 is covered by the SDSS, less than a physical distance of 500 kpc and not centered on the source. This sources was previously studied in the literature and it is also associated with a group of galaxies in the T12 catalog, indicated by a green point.

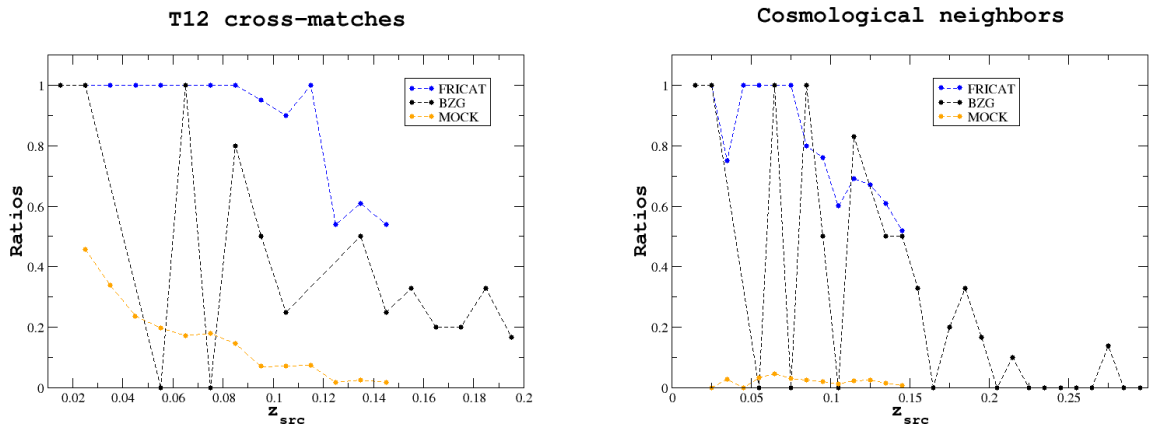

Figure 6.3: *Left:* Here it is shown in blue the fraction of FR Is associated with a group/cluster of galaxies from the T12 catalog, with respect to the total number of sources in the FRICAT in each redshift bin. The same ratio for BZGs is shown in black with respect to the total number of BZGs in each redshift bin, and the same for MOCK sources in orange. The number of BZGs at $z < 0.1$ is very low, that is the reason for the strong fluctuations in consecutive redshift bins, the number increases with redshift so the ratio stabilise. The fraction of sources increases with redshift because of the higher efficiency of the algorithm of T12 in finding clusters at lower redshift. *Right:* Here it is shown the fraction of sources found in richer environment than a MOCK population of quiescent elliptical galaxies randomly placed in the sky using the *"cosmological neighbors"* overdensities method. The color codes of the populations are the same as in left panel. The fraction decreases with redshift because at higher redshift there are less data of the spectroscopic redshift measured with the SDSS, so it is less likely to find *"cosmological neighbors"* overdensities at higher redshift.

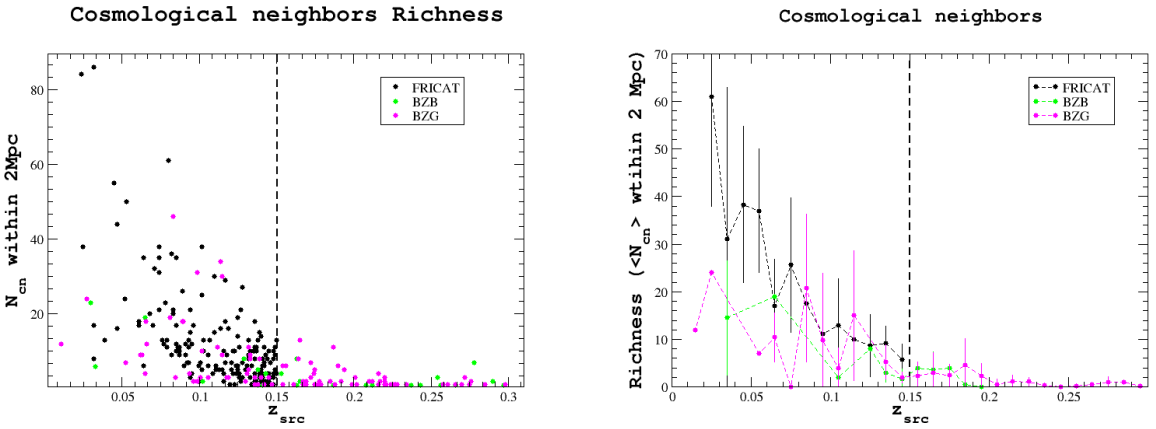

Figure 6.4: *Left:* Number of *"cosmological neighbors"* N_{cn} inside 2 Mpc vs source redshift z_{src}. Black circles represent FR Is, green points represent BZBs and magenta BZGs. The vertical dashed line marks $z = 0.15$, the limiting redshift for the FR I sample. *Right:* The average number of *"cosmological neighbors"* $< N_{cn} >$ computed within 2 Mpc from the central source for redshift bin z_{src}. The error is computed on the basis of the distribution of N_{cn} within the same redshift bin for each source class. Again, the vertical dashed line marks the limiting redshift for the FR I sample, and black points represent FR Is, green points represent BZBs and magenta points BZGs.

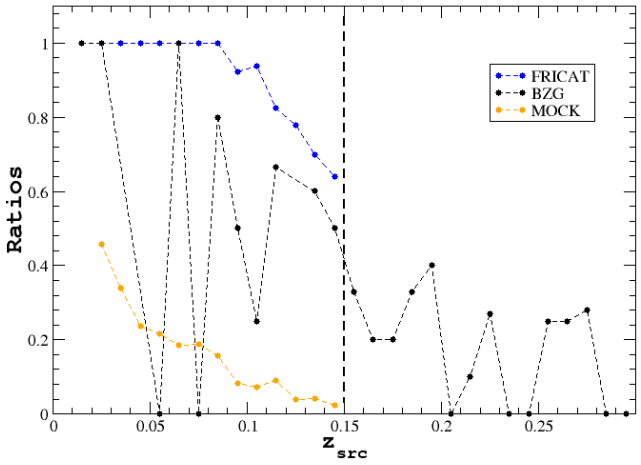

Figure 6.5: The ratio of FR Is residing in rich-galaxy environments according to the settled conditions combining all methods (T12 cross-matches, *"cosmological neighbors"* overdensities, DBSCAN + OPTICS, Voronoi Tesselation and MST) over the total number of galaxies for each redshift bin is represented in blue, the same ratio for BZGs is represented in magenta and for the MOCK catalog in orange. The fraction of sources found in clusters decreases with redshift because so it does the effectivity of two of the methods used in finding clusters, i.e., T12 positional cross-matches and *"cosmological neighbors"* overdensities.

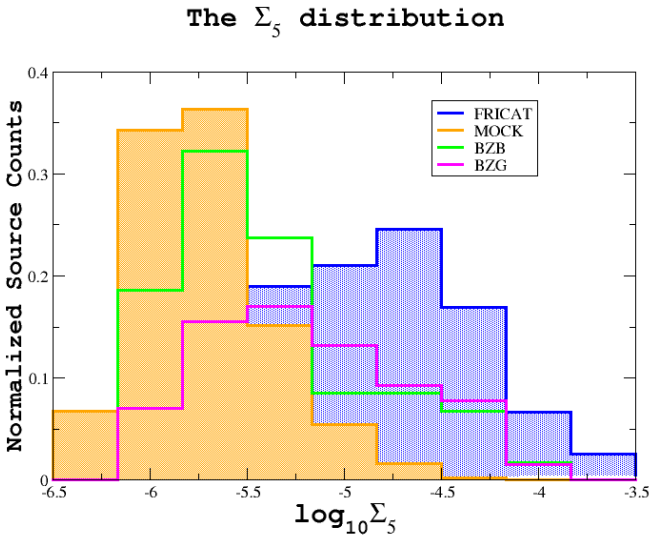

Figure 6.6: Normalized distribution of the fifth nearest neighbor density defined by the Σ_5 parameter for BZBs, BZGs and FR Is and MOCK taken from Chapter 5 for comparison. BZBs and FR Is showed a difference over a 94% of confidence ni KS-test, while no difference was found between BZGs and FR Is using the same test over a 90% interval.

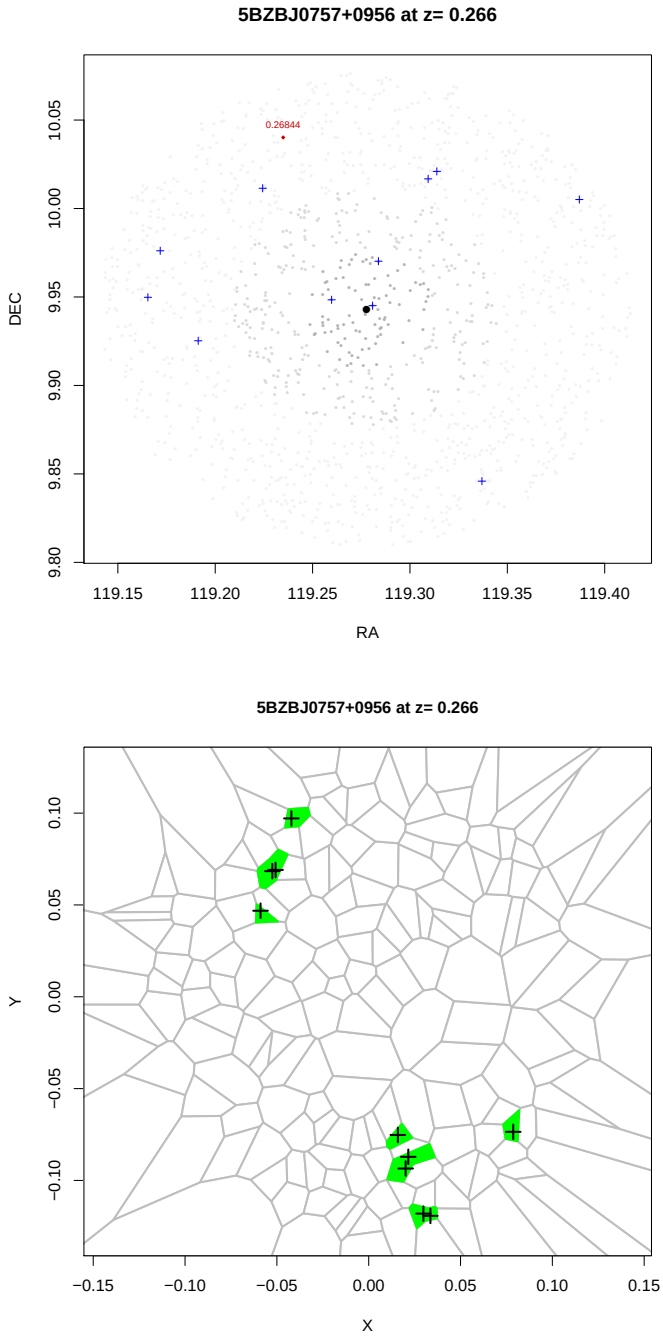

Figure 6.7: *Top:* all the SDSS sources within a circular region of 2 Mpc around 5BZB J0757+0956 having clean photometry and classified as galaxies are plotted in decreasing intensities of grey, indicating those inside 500 kpc, 1 Mpc and 2 Mpc respectively. Red points indicate *"cosmological neighbors"*, i.e., sources with a difference in their spectroscopic redshift with respect of the central source in the SDSS of $\Delta z < 0.005$. Blue crosses are for the *"candidate elliptical galaxies"*. *Bottom:* Voronoi Tesselation diagram for this BZB. High density regions are shown in green and sources inside them are marked by a black cross. None of this high density regions were found above the threshold chosen for the MOCK catalog, so they were not considered clusters. In addition, the source was not inside any of them, this BL Lac was not found in a galaxy rich large-scale environment.

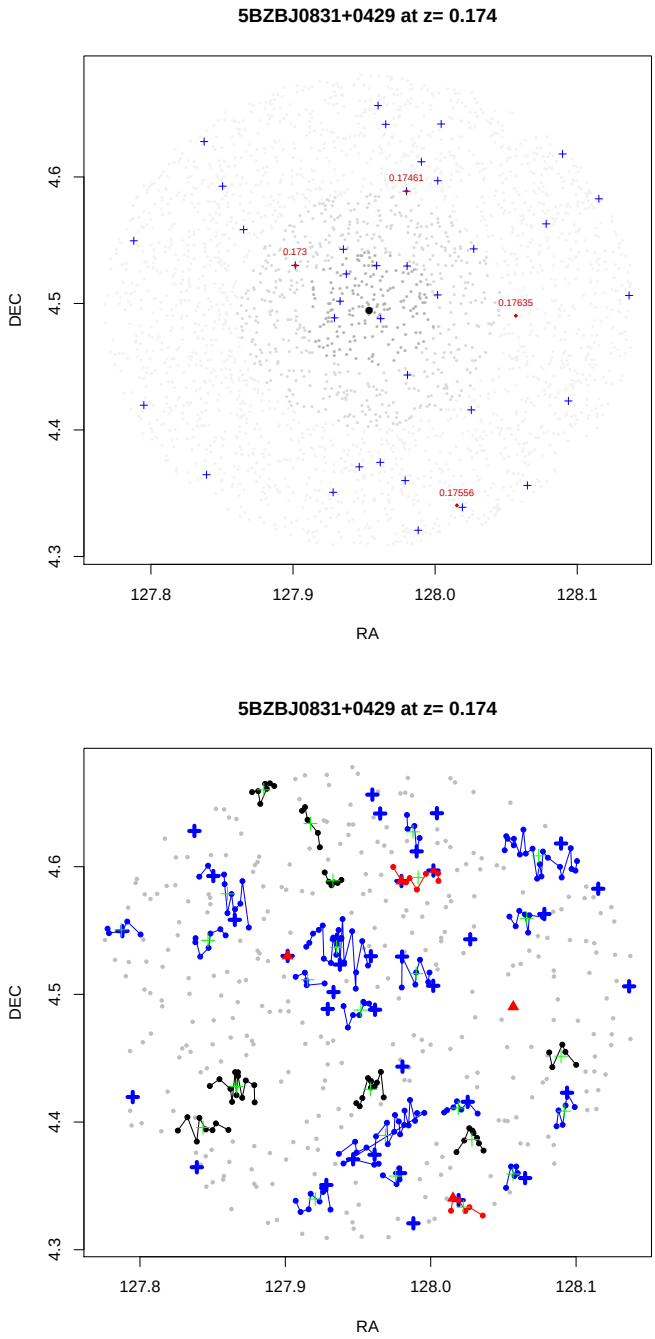

Figure 6.8: *Top:* same as left panel of Fig. 6.7. *Bottom:* DBSCAN + OPTICS algorithm for this BZB. All SDSS galaxies are represented by grey points, *"candidate elliptical galaxies"* by blue crosses and *"cosmological neighbors"* by blue triangles. Clusters detected using the algorithms are represented by connected points according to the following color coding: in black those composed by SDSS galaxies, in blue those hosting a *"candidate elliptical galaxy"* and in red those for which at least one of their components are a *"cosmological neighbor"*. DBSCAN + OPTICS is the only algorithm that finds this source in a group/cluster of galaxies, not enough to consider it in a galaxy rich large-scale environment according to the settled conditions.

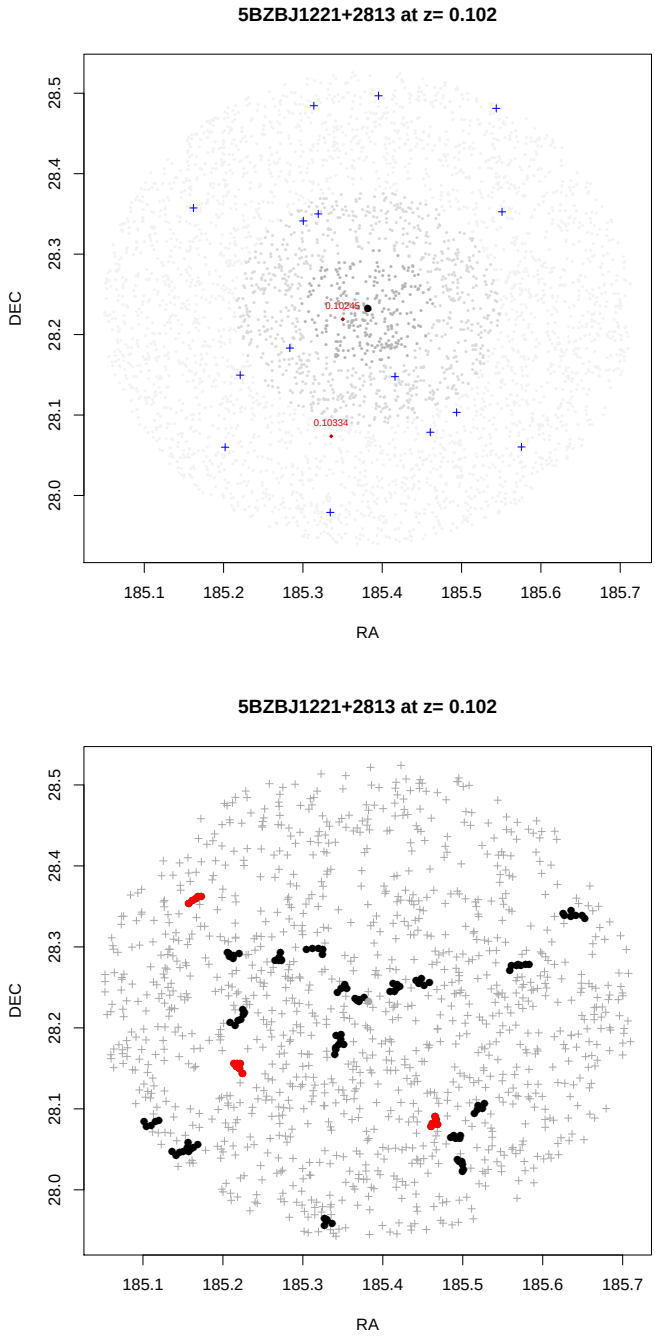

Figure 6.9: *Top:* same as Fig. 6.7 left panel. *Bottom:* example of the application of MST, where the central source was not found to reside in a cluster. Background SDSS sources are represented as red crosses, clusters found with MST among these sources are shown as black points, and clusters for which at least one of their members is a *"candidate elliptical galaxy"* are shown as red points.

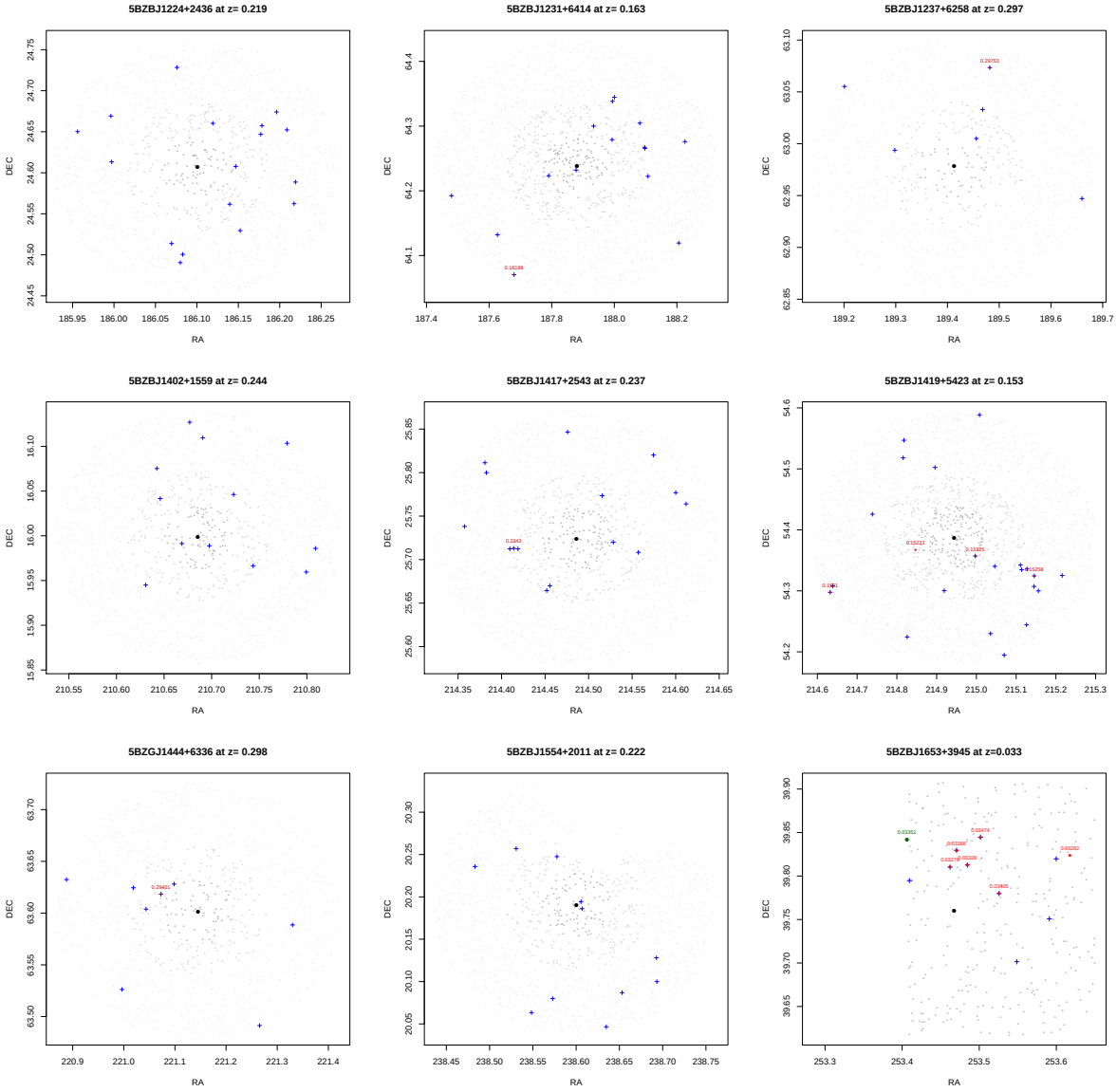

Figure 6.10: BL Lacs previously studied in the literature. Same as Fig. 6.7 left panel for: 5BZB J1224+2436 (*top left*), 5BZB J1231+6414 (*top middle*), 5BZB J1237+6258 (*top righ*), 5BZB J1402+1559 (*middle left*), 5BZB J1417+2543 (*middle middle*), 5BZB J1419+5423 (*middle right*), 5BZG J1444+6336 (*bottom left*), 5BZB J1554+2011 (*bottom middle*) and 5BZB J1653+3945 (*bottom right*).

CHAPTER 7

Implementing Roma-BZCAT

As previously stated, the number of sources in the Roma-BZCAT v.5 is 3,561, being only 1,059 of them confirmed BL Lacs and among these, for only 437 of them the value of their redshift is known. To improve statistics in their study, it is important to find methods to discover new BL Lacs and measure their redshifts. Increase the number of confirmed BL Lacs is not only important to improve the statistics in the clustering method presented in previous Chapters, but also to build the luminosity function of BL Lacs (see e.g. Ajello et al., 2014) and to obtain stringent limits on the dark matter annihilation in sub-halos (see e.g. Berlin & Hooper, 2014).

The most recent *Fermi* catalog is the 3FGL (Acero et al., 2015), a catalog of 3,033 sources detected in the γ-rays in the energy range 20 MeV - 300 GeV. From these sources, 1,010 ($\sim$ 30%) remain unassociated with a low energy counterpart and they are called Unassociated Gamma-ray Sources (UGSs). Associating them is a challenging task because the positional uncertainties of the *Fermi*-LAT are of the order of 0.1 deg, too large to identify sources strictly by positional coincidence in the sky, since hundreds of low energy sources can be identified inside a *Fermi*-LAT error ellipse, as shown in Fig. 7.1. Unveiling the UGS nature was set as one of the major scientific goals of the *Fermi* mission (Atwood et al., 2009).

UGSs have a uniform distribution in the sky showing some excess in the Galactic plane, indicating many of them are potentially extragalactic. Most of the associated sources are BL Lacs (660), they are the strongest extragalactic γ-ray emitters (Massaro et al., 2015b). Given their low spatial density (0.1 sources degree^{-2}) and since the extragalactic γ-ray sky is dominated by their emission, possibly many of the sources that are still unassociated in the 3FGL could be BL Lacs. Looking for BL Lacs among UGSs is a efficient way to discover new BL Lacs and in the future add them to an updated version of the Roma-BZCAT.

In addition, 28% of the sources associated with a low energy counterpart in the 3FGL, have been found using information from multifrequency catalogs, so most of them lack of a spectroscopic classification. They present multifrequency behaviour similar to blazars, but often no optical spectra

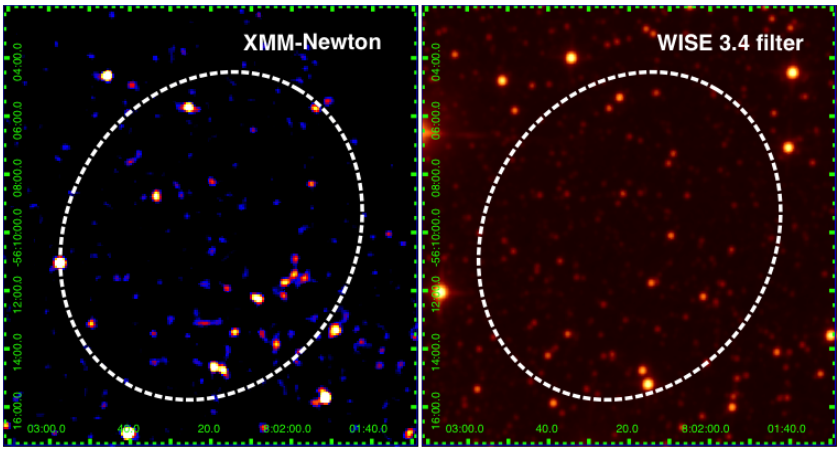

Figure 7.1: The *Fermi* positional uncertainty region at the 95% level of confidence is overlaid as a white dashed ellipse to the XMM-Newton X-ray (left) and to the WISE 4.6μm mid-IR (right) images of the γ-ray source 3FGL J0802.3-5610. There is a large number of low-energy counterparts inside the LAT uncertainty region.

are available to precisely determine its class, or their signal-to-noise (S/N) ratio could be too low to allow a precise determination of their nature. When such situation occurs, γ-ray objects are classified as blazar candidates of uncertain type (BCUs) in the 3FGL, previously labelled as active galaxies of uncertain type (AGUs) in the 1FGL and 2FGL. It is important to study their nature, since many of them could be BL Lacs, but that classification cannot be certain until an optical spectra becomes available.

In 2012 our group started an optical spectroscopic campaign to search for BL Lacs as optical counterparts of the UGSs selected having IR colors similar to those of the known γ-ray BL Lac population measured in the four bands of *WISE* (as seen in Fig. 7.2), and to observe the spectra of BCUs. Optical spectroscopy is crucial to determine the nature of these sources because multifrequency methods previously stated such peculiar IR colors are valuable to selected potential candidates, but optical spectroscopy is necessary to confirm the lack of emission/absorption features and therefore the BL Lac classification. The main goal of the campaign is to collect the spectra of sources reported in the WIBRALs catalog, having IR colors similar to those of the *Fermi* blazars but lying within the γ-ray positional uncertainty region of the UGSs, their potential counterparts. In addition, optical spectra of BCUs were observed to confirm which of those sources were blazars, and to determine their redshift. As a secondary aim, previously confirmed BL Lacs for which the redshift estimate was uncertain or unknown were reobserved, to see if due to variability some lines became visible so it was possible to measure their redshift. This optical spectroscopic campaign was carried out both observing with telescopes and searching for optical spectra in major optical databases and surveys. To minimize the impact on telescope schedules and maximize the scientific return, a small subsample of targets was proposed each time and the sample selection was mainly driven by source visibility during the nights obtained at each telescope. Here I present the summary of the results achieved during the last three years of the spectroscopic campaign.

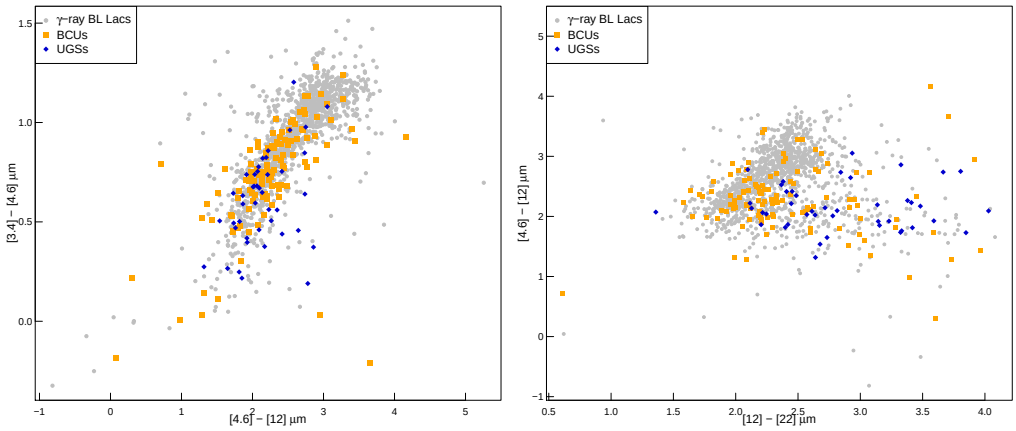

Figure 7.2: *Left:* [3.4]-[4.6]-[12] μm WISE color-color diagram. I report the γ-ray BL Lacs from the Roma-BZCAT v.5 associated with a WISE source within a region of radius 2.4" (grey), the BCUs and AGUs presented in the campaign (orange squares) and the UGSs observed in the campaign (blue squares). *Right:* [4.6]-[12]-[22] μm WISE color-color diagram for the γ-ray BL Lacs from the Roma-BZCAT v.5 associated with a WISE source within a region of radius 2.4" (grey), the BCUs and AGUs presented in the campaign (orange squares) and the UGSs observed in the campaign (blue squares).

7.1 Observations

Here I list the telescopes and their instrument configuration used in this last three years of the optical spectroscopic campaign, the number of sources observed in each one of them and the dates of the observing nights.

7.1.1 Telescopes sample

The spectra of 16 objects were obtained in remote observing mode at the Kitt Peak National Observatory (KPNO) Mayall 4 m telescope using the R-C spectrograph on the nights of 2014 February 5th and June 4th, and *in situ* between 2016 December 7th and December 11th. A slit width of 1.2" and low-resolution gratings were adopted, yielding a dispersion of 3 Å pixel^{-1}. Wavelength calibration was accomplished using the spectra of a helium-neon-argon lamp which guarantees smooth coverage over the entire range. Due to poor long-term stability during each night, flexures of the instruments and drift needed to be taken into account, and so an arc frame was taken before every target to maintain a good wavelength resolution for the scientific spectra, reaching an accuracy of $\sim$ 3 Å rms.

The spectra of 12 objects were obtained using the 3.58 m Telescopio Nazionale Galileo (TNG) located at La Palma, Canary Islands (Spain) between 2013 October and 2014 July. Its imaging spectrograph DOLoReS carried a 2048×2048 pixel E2V 4240 CCD; spectra were acquired with the LR-B grism and a 1.5" slit width which secured a nominal spectra coverage in the 3500 - 8200 Å range and a dispersion of 2.5 Å pixel^{-1}. Wavelength calibration was achieved using spectra of a helium-neon lamp acquired between two exposures of the same object. Again, an arc frame before every target was taken for a good wavelength solution, because of the flexures of the instruments and drift due to poor long-term stability.

A number of 16 objects were observed with the 2.1 m telescope of the Observatorio Astronómico

Nacional (OAN) in San Pedro Mártir (Mexico) between 2014 September and 2017 August. The telescope carries a Boller and Chivens spectrograph and a 1024 × 1024 pixel E2V 4240 CCD. The slit width was 2". The spectrograph was tuned to the 4000 - 8000 Å range with a resolution of 10 Å pixel^{-1}. Wavelength calibration was performed using a cooper-helium-neon-argon lamp. For each acquisition, bias subtraction, flat field correction and cosmic-ray rejection were performed. To remove cosmic rays, two or three individual exposures for each target were achieved and averaged according to their S/Ns.

Four spectra were observed with the 4.2 m William Herschel Telescope (WHT) in La Palma, Canary Islands (Spain), on three different nights between 2013 November and 2014 March. A slit of 2" was adopted and the low-resolution imaging spectrograph ACAM was used with a detector E2V EEV4482. The spectrograph was tuned in the 4000 - 8000 Å range and wavelength calibration was done using the spectra of a helium-neon-argon lamp.

The spectra of 96 objects were observed with the Southern Astrophysical Research Telescope (SOAR), a 4.1 m telescope situated in Cerro Pachón (Chile). The objects were observed on different nights between 2013 November and 2017 August in both *in situ* and remote observing modes, using the Goodman High Throughput spectrograph. I used the 400 line mm^{-1} grating centered at 5000 Å, which gave wavelength coverage between 3000 and 7000 Å and a resolution of $\sim$ 830, with a dispersion of 1 Å pixel^{-1}. Slit width was 1", and wavelength calibration was accomplished using the spectra of an iron-argon lamp.

Four additional observations were made in 2015 January with the 6.5 m Baade Magellan Telescope (Cerro Manqui, Chile) using the Inamori Magellan Areal Camera and Spectrograph. The f/2 camera was used in combination with the 300 line mm^{-1} grism and a 0.7" slit to yield spectra with dispersion of 1.34 Å pixel^{-1} and FWHM resolution of $\sim$ 4 Å.

7.1.2 Data reduction procedures

The whole set of spectroscopic data acquired at these telescopes was optimally extracted (Horne, 1986) and reduced following standard procedures using IRAF[1]. Calibration frames (flat fields and bias) were taken on the afternoon preceding each observing night. The wavelength calibration was performed using lamp data acquired soon after each spectroscopic acquisition, the uncertainty in this calibration was $\sim$ 0.5 Å in all cases according to checks made using the positions of background night sky lines. Flux calibration was obtained observing cataloged spectrophotometric standards. Multiple spectra were acquired from a given object and the data were stacked together to increase the S/N ratio and to achieve cosmic-ray rejection. Finally, spectra were dereddened for the galactic absorption assuming E_{B-V} values taken by the Schlegel et al. (1998) relation. I also presented normalized spectra, obtained dividing the normal spectra to a fit of the continuum, to better show faint spectral features.

[1]IRAF is the Image Reduction and Analysis Facility made available to the astronomical community by the National Optical Astronomy Observatories, which are operated by AURA, Inc., under contract with the U.S. National Science Foundation. It is available at http://iraf.noao.edu/

7.1.3 Results for the telescopes sample

All sources for which spectroscopic observations were acquired, selected having IR colors similar to those of the known γ-ray BL Lac population inside the uncertainty region of UGSs are reported in Table 7.1, while the spectroscopic observations taken to unveil the blazar nature of BCUs and AGUs are described in Table 7.2. In such Tables the following information is provided: (i) their *Fermi* names in the corresponding catalog; (ii) the IR/radio (i.e., WISE, 2MASS or NVSS in this order of preference) name of the counterpart observed; (iii) the telescope used to achieve the observations; (iv) the value of redshift when possible; (v) optical classification using the Roma-BZCAT v.5 nomenclature: BZB for BL Lac objects, BZQ for flat spectrum radio quasars, BZG for BL Lacs of galaxy type and QSO for sources having no radio counterpart and/or not a flat radio spectrum but a quasar-like (i.e., broad emission lines) optical behaviour, respectively. It is worth noting that QSOs, having no blazar-like radio emission could be contaminants situated in the same region as *Fermi* blazars in the WISE color-color diagram. Then I also show (vii) the reference among the campaign papers, corresponding to: Álvarez-Crespo+16a for Álvarez Crespo et al. (2016a), Álvarez-Crespo+16c for Álvarez Crespo et al. (2016c), Peña-Herazo+17 for Peña-Herazo et al. (2017) and Marchesini+18 for Marchesini et al. in press. In Table 7.3 I report the sources already reported as BL Lacs in the literature without a reliable value for the redshift reobserved in the campaign, to see if due to the intrinsic variability of these sources, there were new lines that could be observed. The information given in the table is the same than in the previous two, but substituting in column (ii) the Roma-BZCAT name.

The UGS subsample consists on 43 sources, 27 of which were found to be BL Lacs and small features were present to allow us determine the redshift for only four of them. Seven more objects were found to be BZGs, and no BZQ were found among the observations. The rest of the objects were 9 QSOs for which there was no radio information, possibly contaminants of the selection procedure.

A total of 91 BCUs/AGUs were observed finding that most of them (i.e., 68, $\sim$ 75%) were BZBs and it was possible to measure the redshift for 17 of them. A number of 16 more sources were classified as BZQs because of their quasar-like optical and flat radio spectra ($\alpha < 0.5$), while more 6 BZGs were found. One contaminant was found among the BCUs, a Seyfert galaxy. The redshift could be calculated for four out of 14 BL Lacs reobserved, sources that were classified as BL Lacs in the literature but without an available value of the redshift.

I report in the top left panel of Fig. 7.3 the spectra of WISE J001540.13+555144.7, potential counterpart of the UGS 3FGL J0015.7+5552, found to be a BZB at unknown redshift in Álvarez Crespo et al. (2016a). In the top right panel of that same figure I show the spectra of WISE J061822.65-242637.7, a BCU in the 3FGL associated with the γ-ray source 3FGL J0618.2-2429 reported in Álvarez Crespo et al. (2016c). I found a quasar-like optical and radio flat ($\alpha < 0.5$) spectra for this source, so I classified it as a BZQ at $z = 0.2995$. The source shown in the bottom panel of the same figure is WISE J154824.38+145702.8, an UGS associated with the *Fermi* source 3FGL J1548.4+1455 found to be a BZG at $z = 0.23$.

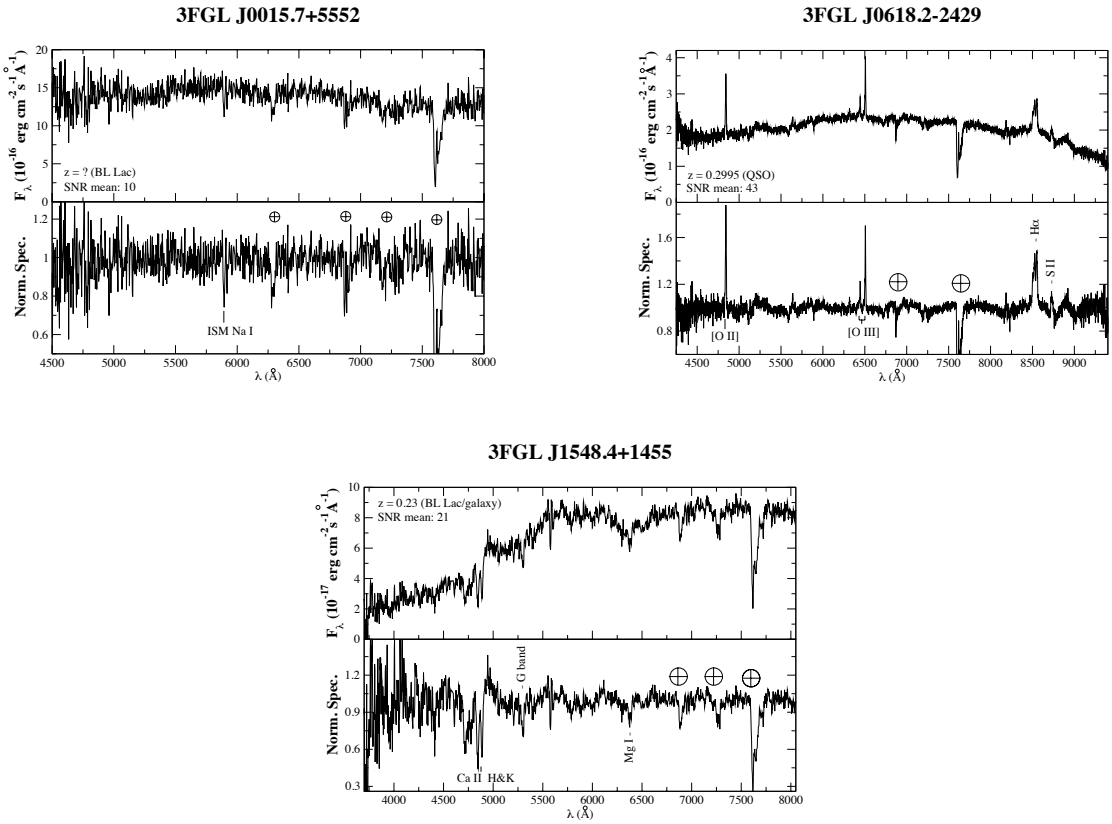

Figure 7.3: *Top left:* optical spectra of WISE J001540.13+555144.7, potential counterpart of the UGS 3FGL J0015.7+5552. It was classified as a BZB on the basis of its featureless continuum, it was not possible to determine its redshift. The average S/N is also indicated in the figure and in the lower panel it is shown the same spectra normalized to better distinguish weak features. *Top right:* The optical spectrum of WISE J061822.65-242637.7, a BCU associated with 3FGL J0618.2-2429. Emission features [O II] (λ_{obs} = 4842 Å), the doublet [O III] (λ_{obs} = 6445 - 6507 Å), H (λ_{obs} = 8534 Å) and [S II] (λ_{obs} = 8731 Å). Classified as a BZQ at redshift $z = 0.2995$. The average S/N is also indicated in the figure and in the lower panel it is shown the same spectra normalized to better distinguish weak features. *Bottom:* The optical spectrum of WISE J154824.38+145702.8, potential counterpart of the UGS 3FGL J1548.4+1455. The spectrum is dominated by the emission of the host elliptical galaxy and shows doublet Ca H+K (λ_{obs} = 4845 - 4887 Å), G band and Mg I (λ_{obs} = 6376 Å). These features made possible a redshift measurement of $z = 0.23$. The average S/N is also indicated in the figure and in the lower panel it is shown the same spectra normalized to better distinguish weak features.

Table 7.1: Summary of the new blazars inside the uncertainty region of UGSs selected using IR colors observed during the last three years of the optical spectroscopic campaign.

Fermi name	WISE counterpart name	Telescope	z	class	Reference
1FHL J0030.1-1647	WISE J003020.44-164713.1	SOAR	0.237	BZB	Álvarez-Crespo+16c
1FHL J0044.0-1111	WISE J004348.66-111607.2	SOAR	0.264	BZB	Álvarez-Crespo+16c
3FGL J0121.8-3917	WISE J012152.69-391544.2	SOAR	0.39	BZB	Peña-Herazo+17
3FGL J0156.5-2423	WISE J015624.54-242003.7	SOAR	?	BZB	Peña-Herazo+17
3FGL J0200.3-4108	WISE J020020.94-410935.7	SOAR	?	BZB	Peña-Herazo+17
3FGL J0307.3+4916	WISE J030727.21+491510.6	TNG	?	BZB	Álvarez-Crespo+16c
3FGL J0312.7-2222	WISE J031235.70-222117.2	SOAR	?	BZB	Peña-Herazo+17
3FGL J0340.4-2423	WISE J034050.11-242254.6	SOAR	0.683	QSO	Peña-Herazo+17
3FGL J0351.0-2816	WISE J035051.32-281632.8	SOAR	?	BZB	Peña-Herazo+17
1FGL J0411.6+5459	WISE J041203.78+545747.2	OAN	?	BZB	Álvarez-Crespo+16c
3FGL J0414.9-0840	WISE J041433.10-084206.8	SOAR	?	BZB	Peña-Herazo+17
3FGL J0420.4-6013	WISE J042011.02-601505.5	SOAR	?	BZB	Peña-Herazo+17
3FGL J0437.7-7330	WISE J043837.07-732921.6	SOAR	0.15	BZG	Peña-Herazo+17
3FGL J0704.3-4828	WISE J070421.81-482647.5	SOAR	?	BZB	Peña-Herazo+17
3FGL J0721.5-0221	WISE J072113.90-022055.0	SOAR	?	BZB	Álvarez-Crespo+16c & Peña-Herazo+17
3FGL J0747.5-4927	WISE J074724.74-492633.1	SOAR	?	BZB	Peña-Herazo+17
3FGL J0826.3-6400	WISE J082627.86-640415.4	SOAR	?	BZB	Peña-Herazo+17
3FGL J0952.8+0711	WISE J095249.57+071330.1	KPNO	?	BZB	Marchesini+18
3FGL J1013.4-4008	WISE J101319.30-400550.4	SOAR	?	BZB	Peña-Herazo+17
3FGL J1033.0-5945	WISE J103332.15-503528.8	SOAR	?	BZB	Peña-Herazo+17
3FGL J1100.2-2044	WISE J110028.22-205000.7	SOAR	0.239	BZG	Peña-Herazo+17
1FGL J1129.2-0528	WISE J112914.05-052856.3	SOAR	0.920	QSO	Peña-Herazo+17
3FGL J1132.0-4736	WISE J113209.26-473853.3	SOAR	0.210	BZG	Peña-Herazo+17
3FGL J1221.5-0632	WISE J122127.20-062847.8	SOAR	0.44	QSO	Álvarez-Crespo+16c
3FGL J1325.2-5411	WISE J132457.35-541503.2	SOAR	0.218	BZG	Peña-Herazo+17
3FGL J1548.4+1455	WISE J154824.38+145702.8	TNG	0.23	BZG	Álvarez-Crespo+16c
3FGL J1704.1+1234	WISE J170409.58+123421.7	TNG	0.45	BZB	Álvarez-Crespo+16c
3FGL J1946.4-5403	WISE J194633.62-540236.4	SOAR	0.460	QSO	Peña-Herazo+17
3FGL J2009.2-1458	WISE J200838.59-150453.2	SOAR	0.99	QSO	Peña-Herazo+17
3FGL J2015.3-1431	WISE J201525.02-143203.9	SOAR	?	BZB	Álvarez-Crespo+16c
3FGL J2030.5-1439	WISE J203027.91-143917.1	SOAR	0.234	QSO	Peña-Herazo+17
3FGL J2112.5-3044	WISE J211217.41-304655.3	SOAR	0.216	BZG	Peña-Herazo+17
3FGL J2134.5-2131	WISE J213430.18-213032.8	SOAR	?	BZB	Álvarez-Crespo+16c
3FGL J2144.6-5640	WISE J214429.57-563849.0	SOAR	?	BZB	Peña-Herazo+17
3FGL J2150.5-1754	WISE J215046.60-174954.1	SOAR	0.186	BZG	Peña-Herazo+17
3FGL J2209.8-0450	WISE J220941.69-045110.3	SOAR	?	BZB	Peña-Herazo+17
3FGL J2237.5-8326	WISE J224201.61-832744.4	SOAR	0.202	QSO	Peña-Herazo+17
3FGL J2244.6+2503	WISE J224436.66+250343.1	SOAR	?	BZB	Peña-Herazo+17
3FGL J2300.1-3547	WISE J230053.29-355051.0	SOAR	0.753	QSO	Peña-Herazo+17
3FGL J2321.6-1619	WISE J232136.98-161928.3	SOAR	0.753	QSO	Peña-Herazo+17
3FGL J2337.2-8425	WISE J233627.96-842652.1	SOAR	?	BZB	Peña-Herazo+17
3FGL J2351.9-7601	WISE J235116.13-760015.5	SOAR	?	BZB	Peña-Herazo+17
3FGL J2358.6-1809	WISE J235836.83-180717.4	SOAR	?	BZB	Peña-Herazo+17

Columns description. (1): *Fermi* name; (2): WISE counterpart name; (3): telescope; (4): redshift; (5): classification; (6): spectrum reference.

Table 7.2: Summary of the BCUs/AGUs observed during the last three years of the optical spectroscopic campaign.

Fermi name	WISE/NVSS/2MASS counterpart name	Telescope	z	class	Reference
3FGL J0015.7+5552	WISE J001540.13+555144.7	KPNO	?	BZB	Álvarez-Crespo+16a
3FGL J0021.6-6835	WISE J002406.72-682054.5	SOAR	0.354	BZQ	Marchesini+18
3FGL J0040.5-2339	WISE J004024.90-234000.7	SOAR	0.213	BZG	Marchesini+18
3FGL J0050.0-4458	WISE J004916.62-445711.2	SOAR	0.121	QSO/Sy	Marchesini+18
3FGL J0059.1-5701	WISE J005846.59-565911.4	SOAR	0.677	BZQ	Marchesini+18
3FGL J0103.7+1323	WISE J010345.74+132345.3	TNG	0.45	BZB	Álvarez-Crespo+16c
3FGL J0127.2+0325	WISE J012713.94+032300.6	SOAR	?	BZB	Peña-Herazo+17
3FGL J0133.2-5159	WISE J013305.75-520003.9	SOAR	0.925	BZQ	Marchesini+18
3FGL J0148.3+5200	WISE J014820.33+520204.9	OAN	?	BZB	Álvarez-Crespo+16a
3FGL J0145.6+8600	WISE J014935.28+860115.4	TNG	0.15	BZG	Álvarez-Crespo+16a
3FGL J0219.0+2440	WISE J021900.40+244520.6	OAN	?	BZB	Álvarez-Crespo+16a
3FGL J0211.2-0649	WISE J021116.95-064419.9	SOAR	0.193	BZB	Marchesini+18
3FGL J0301.4-1652	WISE J030116.62-165245.0	SOAR	0.278	BZG	Marchesini+18
3FGL J0310.4-5015	WISE J031034.72-501631.1	SOAR	?	BZB	Peña-Herazo+17
2FGL J0332.5-1118	WISE J033223.25-111950.6	SOAR	0.2074	BZQ	Álvarez-Crespo+16c
3FGL J0352.9+5655	WISE J035309.54+565430.7	WHT	?	BZB	Álvarez-Crespo+16c
3FGL J0433.1+3228	WISE J043307.54+322840.7	KPNO	?	BZB	Álvarez-Crespo+16a
3FGL J0439.9-1859	WISE J043949.72-190101.5	SOAR	?	BZB	Peña-Herazo+17
3FGL J0508.2-1936	WISE J050818.99-193555.7	SOAR	1.88	BZQ	Álvarez-Crespo+16c
3FGL J0618.2-2429	WISE J061822.65-242637.7	Magellan	0.2995	BZQ	Álvarez-Crespo+16c
3FGL J0623.3+3043	WISE J062316.03+304457.7	KPNO	?	BZB	Marchesini+18
3FGL J0626.6-4259	WISE J062636.71-425805.9	SOAR	?	BZB	Peña-Herazo+17
3FGL J0649.6-3138	WISE J064933.60-313920.3	SOAR	≥ 0.563	BZB	Peña-Herazo+17
3FGL J0653.6+2817	WISE J065344.26+281547.5	KPNO	?	BZB	Marchesini+18
3FGL J0700.0+1709	WISE J070001.49+170921.9	OAN	1.08	BZQ	Álvarez-Crespo+16c
3FGL J0700.2+1304	WISE J070014.31+130424.4	KPNO	?	BZB	Álvarez-Crespo+16a
3FGL J0703.4-3914	WISE J070312.65-391418.8	SOAR	?	BZB	Peña-Herazo+17
3FGL J0720.0-4010	WISE J071939.18-401147.4	Magellan	?	BZB	Álvarez-Crespo+16c
3FGL J0728.0+4828	WISE J072759.84+482720.3	TNG	?	BZB	Álvarez-Crespo+16a
3FGL J0748.8+4929	WISE J074837.76+493041.0	KPNO	?	BZB	Marchesini+18
3FGL J0803.3-0339	WISE J080311.45-033554.5	SOAR	0.365	BZQ	Peña-Herazo+17
3FGL J0827.2-0711	WISE J082706.16-070845.9	SOAR	?	BZB	Peña-Herazo+17
3FGL J0828.8-2420	WISE J082841.74-241851.1	Magellan	?	BZB	Álvarez-Crespo+16c
3FGL J0858.1-3130	WISE J085802.90-313038.3	SOAR	?	BZB	Peña-Herazo+17
3FGL J0917.3-0344	WISE J091714.61-034314.2	OAN	0.308	BZG	Álvarez-Crespo+16c
3FGL J0922.8-3959	WISE J092246.42-395935.0	SOAR	0.595	BZQ	Marchesini+18
3FGL J0947.1-2542	WISE J094709.52-254059.9	SOAR	?	BZB	Peña-Herazo+17
3FGL J1009.0-3137	WISE J100850.54-313905.5	SOAR	0.534	BZB	Peña-Herazo+17
3FGL J1038.9-5311	WISE J103840.66-531142.9	SOAR	1.45	BZQ	Álvarez-Crespo+16c
3FGL J1040.9-1205	WISE J104108.57-120331.0	SOAR	?	BZB	Marchesini+18
3FGL J1042.0-0557	WISE J104204.30-055816.5	OAN	0.39	BZG	Álvarez-Crespo+16c
3FGL J1052.8-3741	WISE J105258.09-374318.6	SOAR	?	BZB	Marchesini+18
3FGL J1106.4-3643	WISE J110624.04-364658.9	SOAR	1.084	BZB	Peña-Herazo+17
3FGL J1125.0-2101	WISE J112508.62-210105.9	SOAR	?	BZB	Peña-Herazo+17
3FGL J1141.6-1406	WISE J114141.80-140754.6	WHT	?	BZB	Álvarez-Crespo+16c
3FGL J1154.0-3243	WISE J115406.16-324243.0	SOAR	?	BZB	Marchesini+18
3FGL J1203.5-3925	WISE J120317.88-392620.9	SOAR	0.227	BZB	Peña-Herazo+17
3FGL J1218.8-4827	WISE J121902.26-482627.9	SOAR	?	BZB	Peña-Herazo+17
3FGL J1307.6-4300	WISE J130737.98-425938.9	SOAR	?	BZB	Peña-Herazo+17
3FGL J1312.7-2349	WISE J131248.76-235047.3	SOAR	≥ 0.462	BZB	Peña-Herazo+17
3FGL J1322.3+0839	WISE J132210.17+084232.9	KPNO	?	BZB	Álvarez-Crespo+16a
3FGL J1331.1-1328	WISE J133120.35-132605.7	WHT	0.25	BZQ	Álvarez-Crespo+16c
3FGL J1434.6+6640	WISE J143441.46+664026.5	TNG	?	BZB	Álvarez-Crespo+16a
3FGL J1440.0-3955	WISE J143950.86-395518.8	SOAR	0.300	BZB	Marchesini+18
3FGL J1511.8-0513	WISE J151148.56-051346.9	TNG	?	BZB	Álvarez-Crespo+16a
3FGL J1512.2-2255	WISE J151212.75-225508.4	SOAR	?	BZB	Peña-Herazo+17
3FGL J1518.0-2732	WISE J151803.59-273131.1	SOAR	?	BZB	Peña-Herazo+17
3FGL J1539.8-1128	WISE J153941.19-112835.3	SOAR	?	BZB	Peña-Herazo+17
3FGL J1547.1-2801	WISE J154712.13-280221.5	SOAR	?	BZB	Peña-Herazo+17
3FGL J1559.8-2525	WISE J160005.35-252439.7	SOAR	0.416	BZB	Marchesini+18
3FGL J1617.4-5846	WISE J161717.91-584808.0	SOAR	1.414	BZQ	Peña-Herazo+17
2FGL J1624.4+1123	WISE J162444.79+110959.3	WHT	2.1	BZQ	Álvarez-Crespo+16c

3FGL J1637.6-3449	NVSS J163750-344915	SOAR	?	BZB	Peña-Herazo+17
3FGL J1647.4+4950	WISE J164734.91+495000.5	KPNO	0.049	BZQ	Álvarez-Crespo+16a
3FGL J1656.8-2010	WISE J165655.14-201056.2	SOAR	?	BZB	Peña-Herazo+17
3FGL J1736.0+2033	WISE J173605.25+203301.1	TNG	?	BZB	Álvarez-Crespo+16a
2FGL J1803.6+2523c	2MASS J18031240+2521185	OAN	0.77	BZQ	Álvarez-Crespo+16c
3FGL J1816.9-4944	WISE J181655.99-494344.7	SOAR	1.70	BZQ	Marchesini+18
3FGL J1819.1+2134	WISE J181905.22+213233.8	OAN	?	BZB	Álvarez-Crespo+16c
3FGL J1842.3-5841	WISE J184229.83-584157.5	SOAR	?	BZB	Marchesini+18
3FGL J1844.3+1547	WISE J184425.36+154645.8	OAN	?	BZB	Álvarez-Crespo+16c
3FGL J1911.4-1908	WISE J191129.74-190824.8	SOAR	0.138	BZG	Marchesini+18
3FGL J1913.9+4441	WISE J191401.88+443832.2	OAN	?	BZB	Álvarez-Crespo+16a
2FGL J1922.6-7454	WISE J192243.02-745349.5	SOAR	?	BZB	Peña-Herazo+17
3FGL J1933.4+0727	WISEJ193320.3+072616.6	OAN	?	BZB	Marchesini+18
3FGL J1954.9-5640	WISE J195502.86-564028.8	SOAR	0.221	BZB	Marchesini+18
3FGL J1955.0-1605	WISE J195500.65-160338.4	SOAR	≥ 0.360	BZB	Peña-Herazo+17
3FGL J2024.4-0848	WISE J202429.37-084804.6	SOAR	?	BZB	Peña-Herazo+17
3FGL J2036.6-3325	WISE J203649.49-332830.7	SOAR	0.23	BZB	Álvarez-Crespo+16c
3FGL J2046.7-1011	WISE J204654.33-101040.2	SOAR	?	BZB	Marchesini+18
3FGL J2103.9-6233	WISE J210338.38-623225.8	SOAR	?	BZB	Marchesini+18
3FGL J2107.7-4822	WISE J210744.48-482802.9	SOAR	0.079	BZB	Marchesini+18
3FGL J2126.5-3926	WISE J212625.19-392122.2	SOAR	?	BZB	Marchesini+18
3FGL J2144.2+3132	WISE J214415.22+313339.2	OAN	?	BZB	Marchesini+18
3FGL J2156.0+1818	WISE J215601.64+181837.1	OAN	?	BZB	Álvarez-Crespo+16a
3FGL J2159.2-2841	WISE J215910.92-284116.4	SOAR	0.270	BZB	Marchesini+18
3FGL J2212.6+2801	WISE J221239.11+275938.4	OAN	?	BZB	Marchesini+18
3FGL J2305.3-4219	WISE J230512.44-421857.2	SOAR	?	BZB	Marchesini+18
3FGL J2213.6-4755	WISE J221330.35-475425.2	SOAR	≥ 0.797	BZB	Marchesini+18
3FGL J2316.8-5209	WISE J231701.72-521001.4	SOAR	0.7	BZB	Marchesini+18
3FGL J2348.4-5100	WISE J234853.10-510314.0	SOAR	0.392	BZB	Marchesini+18

Columns description. (1): *Fermi* name; (2): WISE/NVSS/2MASS counterpart name; (3): telescope; (4): redshift; (5): classification; (6): spectrum reference.

Table 7.3: Summary of the blazars reobserved during the last three years of the optical spectroscopic campaign.

Fermi name	Roma-BZCAT name	Telescope	z	class	Reference
3FGL J0103.4+5336		KPNO	?	BZB	Álvarez-Crespo+16a
3FGL J0105.3+3928	5BZB J0105+3928	TNG	0.44	BZB	Álvarez-Crespo+16c
3FGL J0333.6+2916	5BZB J0333+2916	TNG	?	BZB	Álvarez-Crespo+16a
3FGL J0708.9+2239	5BZB J0708+2241	OAN	?	BZB	Marchesini+18
	5BZB J0724+2621	KPNO	1.17	BZQ	Álvarez-Crespo+16a
3FGL J0814.1-1012	5BZB J0814-1012	KPNO	?	BZB	Álvarez-Crespo+16a
3FGL J0814.1-1012	5BZB J0814-1012	SOAR	?	BZB	Peña-Herazo+17
2FGL J0819.6-0803		Magellan	?	BZB	Álvarez-Crespo+16c
3FGL J0942.1-0756	5BZB J0942-0759	KPNO	?	BZB	Álvarez-Crespo+16a
3FGL J1013.5+3440	5BZQ J1013+3445	TNG	0.208	BZQ	Álvarez-Crespo+16a
	5BZG J1414+3430	KPNO	?	BZB	Álvarez-Crespo+16a
3FGL J2021.9+0630		KPNO	?	BZB	Álvarez-Crespo+16a
3FGL J2036.4+6551	5BZB J2036+6553	KPNO	?	BZB	Álvarez-Crespo+16a
3FGL J2323.9+4211	5BZB J2323+4210	OAN	?	BZB	Álvarez-Crespo+16a

Columns description. (1): *Fermi* name; (2): Roma-BZCAT v.5 counterpart name; (3): telescope; (4): redshift; (5): classification; (6): spectrum reference.

7.2 Databases

During the campaign I also searched for BCUs in the optical databases SDSS DR12 (Alam et al., 2015) and in the Six-degree-Field Galaxy Survey (6dFGS, Jones et al., 2009) looking for optical spectra that became recently available, to exclude them from the telescope targets. To perform this search, I cross-matched the radio position in the FIRST catalog of the BCUs reported in the 3FGL, with both optical surveys within a 2" radius. I found 124 unique matches in the SDSS DR12 and 73 in the 6dFGS for the BCUs selected within that radius, however out of these cross-matches only 15 in SDSS and 22 on 6dFGS had an optical spectrum available. Additionally, four sources already classified in the Roma-BZCAT but without reported optical spectra were found in the footprint of both surveys. I report three more sources outside the footprint of both surveys considered for which optical spectra became available after the 3FGL publication.

7.2.1 Data reduction procedures

All the optical spectra were visually inspected to avoid misclassifications due to artefacts from the automated spectral analysis and line identifications. The SDSS and 6dFGS classification performed by their automatic procedures sometimes give a value for the redshift for BZBs, even when there is no clear evidence of emission/absorption lines. Again, sources previously classified as BL Lacs in the literature without a known redshift are searched for. In the 6dFGS, redshift measurements are obtained semi-automatically, and spectra are assigned a quality value Q based on visual inspection on a scale of 1 to 6 through assessment of every redshift. Q = 1 is assigned to unusable measurements, Q = 2 to possible but unlikely redshifts, Q = 3 for reliable redshifts and Q = 4 for high-quality redshifts. The quality of the spectra in the 6dFGS does not stand for the quality in terms of S/N, but for the reliability of the redshift value due to a visual evaluations. Since by definition most BL Lacs lack of emission/absorption features, their redshifts cannot be measured, so it is expected that the quality given by 6dFGS is Q= 1, 2.

7.2.2 Results for the databases sample

All BCUs for which optical spectra were found in the surveys are reported in Table 7.4, summarizing the information: (i) their *Fermi* names in the corresponding catalog; (ii) the survey name, SDSS or 6dFGS in which they were found (iii) the value of redshift when possible; (iv) the optical classification given in Álvarez Crespo et al. (2016b).

In Table 7.5 are reported those sources found in the surveys, already reported as BL Lacs in the literature but with no value for the redshift. The information given in the table is: (i) their *Fermi* names in the corresponding catalog; (ii) the survey name, SDSS or 6dFGS in which they were found (iii) the value of redshift when possible; (iv) the optical classification given in Álvarez Crespo et al. (2016b), (v) the Roma-BZCAT name and (vi) the literature for sources outside the SDSS/6dFGS footprint.

For the BCUs found in the optical databases, 26 sources out of 33 were BZBs, and it was possible to estimate the redshift for four of them. Five sources were classified as BZQs, while the remaining two were BZGs. From the seven BL Lacs found in the databases and in the literature, a value of the redshift was found for four of them.

Table 7.4: Summary of the BCUs observed in the optical surveys.

Fermi name	WISE name	Survey name	z	class
3FGL J0009.6-3211	WISE J000935.55-321636.8	6dFGS	0.02	BZQ
3FGL J0028.8+1951	WISE J002829.81+200026.7	SDSS	1.55	BZQ
3FGL J0030.2-1646	WISE J003019.40-164711.7	6dFGS	?	BZB
3FGL J0043.5-0444	WISE J004334.12-044300.6	6dFGS	1.63	BZB
3FGL J0156.9-4742	WISE J015646.03-474417.3	6dFGS	?	BZB
3FGL J0255.8+0532	WISE J025549.51+053355.0	SDSS	?	BZB
3FGL J0339.2-1738	WISE J033913.70-173600.8	6dFGS	0.06	BZQ
3FGL J0439.9-1859	WISE J043949.72-190101.5	6dFGS	?	BZB
3FGL J0521.7+0103	WISE J052140.82+010255.5	SDSS	?	BZB
3FGL J0730.5-6606	WISE J073049.51-660218.9	6dFGS	?	BZB
3FGL J0827.2-0711	WISE J082706.16-070845.9	6dFGS	?	BZB
3FGL J0904.3+4240	WISE J090415.62+423804.5	SDSS	1.34	BZQ
3FGL J0921.0-2258	WISE J092057.47-225721.5	6dFGS	?	BZB
3FGL J1003.6+2608	WISE J100342.22+260512.8	SDSS	0.93	BZB
3FGL J1040.4+0615	WISE J104031.62+061721.7	SDSS	?	BZB
3FGL J1040.8+1342	WISE J104057.69+134211.7	SDSS	?	BZB
3FGL J1125.0-2101	WISE J112508.62-210105.9	6dFGS	?	BZB
3FGL J1129.4-4215	WISE J113007.04-421440.9	6dFGS 3	?	BZB
3FGL J1200.8+1228	WISE J120040.03+123103.2	SDSS	?	BZB
3FGL J1315.4+1130	WISE J131532.62+113331.7	SDSS	0.73	BZB
3FGL J1322.3+0839	WISE J132210.17+084232.9	SDSS	0.32	BZQ
3FGL J1340.6-0408	WISE J134042.02-041006.8	6dFGS	?	BZB
3FGL J1342.7+0945	WISE J134240.02+094752.4	SDSS	0.28	BZG
3FGL J1412.0+5249	WISE J141149.44+524900.2	SDSS	0.08	BZG
3FGL J1549.5+1709	WISE J154929.28+170828.1	SDSS	?	BZB
3FGL J1636.7+2624	WISE J163651.46+262656.7	SDSS	?	BZB
3FGL J1656.8-2010	WISE J165655.14-201056.2	6dFGS	?	BZB
3FGL J1955.0-1605	WISE J195500.65-160338.4	6dFGS	?	BZB
3FGL J2104.2-0211	WISE J210421.92-021239.0	6dFGS	?	BZB
3FGL J2118.0-3241	WISE J211754.91-324328.2	6dFGS	?	BZB
3FGL J2232.9-2021	WISE J223248.80-202226.2	6dFGS	?	BZB
3FGL J2317.3-4534	WISE J231731.98-453359.6	6dFG 1	?	BZB
3FGL J2346.7+0705	WISE J234639.93+070506.8	SDSS	0.17	BZB

Columns description. (1): *Fermi* name; (2): WISE counterpart name; (3): optical survey; (4): redshift; (5): classification.

Table 7.5: Summary of the sources already classified as BL Lacs without redshift found in the optical surveys and in the literature.

Fermi name	Survey name	z	class	Roma-BZCAT name	Reference
3FGL J0003.8-1151	6dFGS	?	BZB	5BZB J0004-1148	
3FGL J0147.0-5204	6dFGS	0.09	BZG	5BZG J0146-5202	
3FGL J0301.8-7157		0.82	BZQ	5BZQ J0301-7156	Titov et al. (2011)
3FGL J0343.3+3622		1.48	BZQ	5BZQ J0343+3622	Vermeulen & Taylor (1995)
3FGL J0434.4-2341		?	BZB	5BZB J0434-2342	Shaw et al. (2013)
3FGL J1256.3-1146	6dFGS	0.06	BZG	5BZG J1256-1146	
3FGL J2109.1-6638	6dFGS	?	BZB	5BZB J2108-6637	

Columns description. (1): *Fermi* name; (2): optical survey; (3): redshift; (4): Roma-BZCAT name; (5): spectrum reference.

7.2.3 Particular sources

Within the UGSs sample, 7 blazar candidates selected using the IR colors had a quasar-like spectra, but none of them had a radio counterpart in NVSS, SUMSS or FIRST and were not observed in the radio follow up performed by Petrov et al. (2013) and Schinzel et al. (2015). The lack of radio detections did not allow a BZQ classification, but rather they are classified as QSOs, they could be contaminants of the IR selection method.
Among the BCUs, the source associated with 3FGL J0353.6+2817 was GB6 J0653+2816. In Álvarez Crespo et al. (2016a) a different target classified as a BZG was pointed: WISE J065340.46+281848.5 at uncertain $z \geq 0.45$. In Marchesini et al. 2018 in press. the right target was observed, WISE J065344.26+281547.5 resulting in a BZB at uncertain redshift.

It was found that WISE J110624.04-364658.9 associated with 3FGL J1106.4-3643 is a high redshift BZB at $z = 1.084$, being the second most distant BZB observed to date (Peña-Herazo et al., 2017).

The BCU NVSS J132210+084231, associated with 3FGL J1322.3+0839, showed two different states. When it was observed in Álvarez Crespo et al. (2016a) showed a BZB non-thermal dominated spectrum, while in the SDSS showed a quasar-like spectrum and it was classified as a a BZQ at $z = 0.32549$. Thus this source is considered as a transition object.
The spectra of the source 5BZB J0724+2621 observed by White et al. (2000) showed a featureless continuum corresponding to the classification as a BL Lac (see top panel Fig. 7.4), but in the observations in Álvarez Crespo et al. (2016a) a broad emission line was detected (see bottom panel Fig. 7.4). This strongly indicates that the source was previously observed during a state dominated by non-thermal radiation that did not allow the detection of emission lines. During my observation, I saw this previously classified BL Lac showed a broad emission line that led to a BZQ classification at a redshift $z = 1.17$. It is a "changing look" blazar (Giommi et al., 2012). It is thought that this blazars are FSRQs whose emission lines are swamped by the relativistically boosted jet flux.

The spectra of the BL Lac 5BZB J0105+3928 when observed by Shaw et al. (2013) showed emission dominated by the host galaxy rather than by non-thermal emission (see top panel in Fig. 7.5). In the observations in Álvarez Crespo et al. (2016c) the spectrum was dominated by continuum emission arising from the jet (see bottom panel in Fig. 7.5). Again this is a "changing look" blazar.

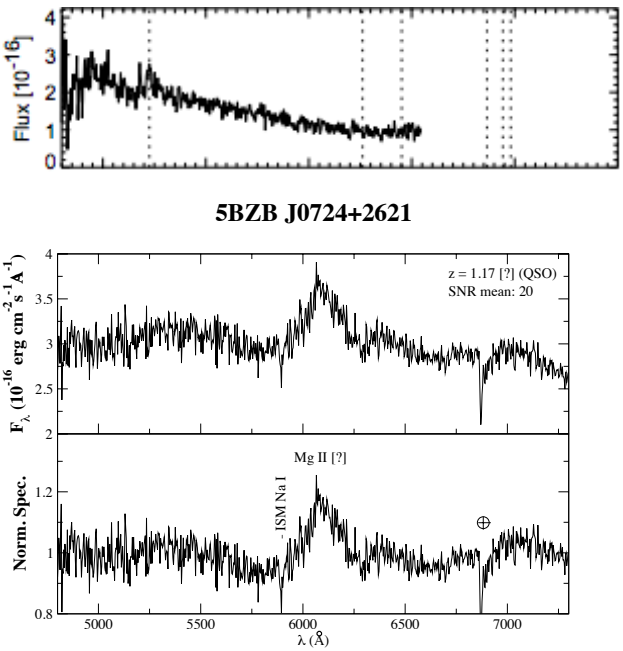

Figure 7.4: *Top:* optical spectra of the source 5BZB J0724+2621 observed by White et al. (2000). Here it showed a featureless continuum corresponding to the classification as a BL Lac. *Bottom:* optical spectra of the same source. In Álvarez Crespo et al. (2016a) it is classified as a BZQ at z = 1.17 due to the broad emission line Mg (λ_{obs} = 6099 Å). The average S/N is also indicated in the figure, and in the lower panel it is shown the same spectra normalized to better distinguish weak features.

7.3 Summary

During this campaign 188 spectra were collected and/or analyzed, the major results achieved are summarized as follows:

- Most of the targets were BL Lacs (132, $\sim$ 70%), strongly suggesting that γ-ray emission is an extremely useful band to discover new BL Lacs, the most elusive class of active galaxies and increase their number in future releases of the Roma-BZCAT.
- Redshifts were obtain for 26 BZBs thanks to the presence of weak emission/absorption features.
- Three transitional or "changing look" objects were discovered.
- One of the BZBs lies at z = 1.17, a rare phenomenon since only 14 BL Lacs are known to lie at redshift higher than 1 in the Roma-BZCAT v.5.

The optical campaign is still ongoing, having 10 more nights scheduled in the telescopes SOAR and Blanco, that under optimal conditions could lead to the observation of $\sim$ 90 new spectra.

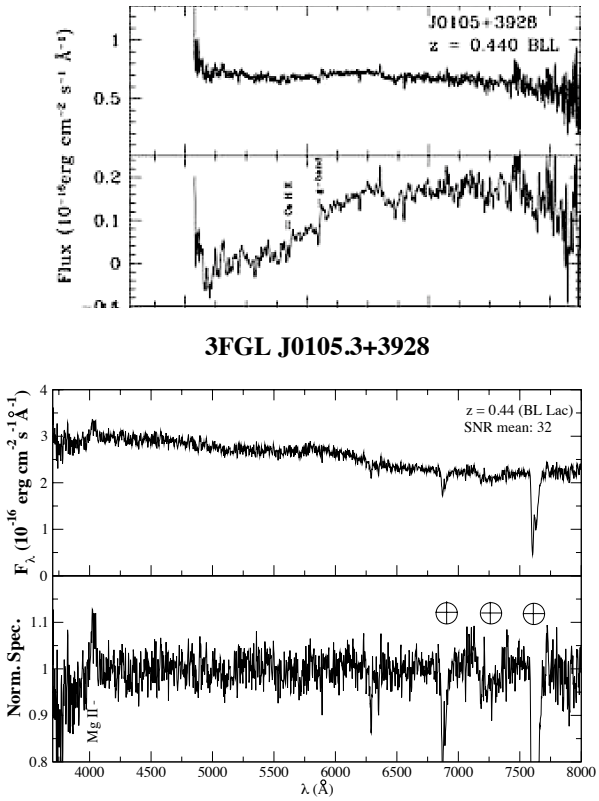

Figure 7.5: *Top:* optical spectra of the BL Lac 5BZB J0105+3928 at $z = 0.44$ associated with the γ-ray source 3FGL J0105.3+3928 observed by Shaw et al. (2013), showing emission dominated by the host galaxy rather than by non-thermal emission. In the lower panel they shown the same spectra normalized. *Bottom:* optical spectra of the same source. In Álvarez Crespo et al. (2016c) it is classified as a BL Lac, and I was able to confirm the redshift at $z = 0.44$ because of the line of Mg II ($\lambda_{obs} = 4031$ Å). The average S/N is also indicated in the figure, and in the lower panel it is shown the same spectra normalized to better distinguish weak features.

Conclusions

According to the Unification Model for radio loud AGNs, radio galaxies are the parent population of blazars, and in particular FR Is seen through their jets should appear as BL Lacs. Considering that the only difference between these two classes is their angle with respect to our line of sight, both flavours should reside in similar environments. Several authors have studied the large-scale environment of FR Is for more than forty years, and it is widely accepted that these objects reside in moderately rich clusters. However to date there has been no systematic study of the large-scale environments in which BL Lacs reside. Studies about this topic have been limited to few a objects, often showing contradictory results. In Chapter 2 I report a summary of the BL Lac environments literature in chronological order and a list of all BL Lacs studied up to date. If FR Is and BL Lacs reside in the same environments, i.e., galaxy clusters, that would represent a solution to the problem of the BL Lac redshift determination due to their characteristic lack of emission/absorption features. If BL Lacs were confirmed to lie in clusters, that would make possible to calculate the redshift of a galaxy in that same cluster, and hence to the BL Lac. On the other hand, if BL Lacs were found in more isolated environments than those of FR Is, that would be in contradiction to the Unification Model and FR Is would no longer be the parent population of BL Lacs, the difference between both classes would not be solely the angle with the observer's line of sight. There is a third potential scenario, if BL Lacs were located in rich environments but different from those of FR Is, that would contradict the Unification Model since BL Lacs would not reside in the same environment as FR Is, but at the same time it would solve the problem of the BL Lac redshift determination.

Here I presented a study of the large-scale environment for a sample of FR Is (FRICAT), that thanks to the author's selection criteria were not contaminated by other radio objects as steep spectrum sources or FR 0s, and it was compared to that of the most comprehensive list of BL Lacs known to date (Roma-BZCAT) with available redshift. For both samples I selected those FR Is and BL Lacs inside the footprint of the SDSS, a large imaging and spectroscopic survey of the Northern sky, and studied the clustering of sources selected as galaxies by the SDSS DR9 pipeline, inside a radius of 2 Mpc around the central FR I/BL Lac. These large-scale environments were analized using the following methods:

- Positional cross-matches of the FR I/BL Lac with a large catalog of groups/clusters of galaxies in the SDSS footprint, having spectroscopic redshifts up to $z = 0.2$. To consider a FR I/BL Lac belonging to a group/cluster of galaxies presented in the catalog, their projected distances must be smaller than 2 Mpc and the difference between their redshifts $\Delta z < 0.005$.

- Positional cross-matches of the FR I/BL Lac with a catalog of clusters of galaxies constructed by combining the identification of the red sequence and the BCG, to see how many of the FR Is and BL Lacs were compatible with being the central BCG of the cluster. A source was considered a BCG when the redshift difference between the source (FR I/BL Lac) and the cluster was less than 0.005 and their projected distance was smaller than 1 kpc.

- The number of sources with an available spectroscopic redshift showing a redshift difference from that of the central FR I/BL Lac $\Delta z < 0.005$ and inside a 2 Mpc radius (so-called *"cosmological neighbors"*), was higher than the number found for a random mock population of elliptical galaxies.

- Combination of different clustering algorithms, such DBSCAN + OPTICS, Voronoi Tesselation and MST. The first two algorithms were selected because of their good behaviour with noise and their efficiency in selecting clusters having irregular shape. MST was selected because the version presently used was implemented to optimize the edge length selection and to avoid selecting satellite clusters. Since statistics for each algorithm is different, so it is their performances therefore several algorithms were applied to the same data for consistency. I applied the gnomonic projection transformation to the angular distances, that converts them into Euclidean distances as an input for the algorithms.

- Number surface density to the 5-th nearest neighbor, a value related to the dark matter halo density in a cluster of galaxies.

FR Is were found in richer environments than quiescent elliptical galaxies, and about 70% of the FR Is lied in environments richer than a MOCK population of galaxies on random positions in the sky. However, only $\sim$ 12% of BL Lacs lied in a group/cluster of galaxies with respect to that same MOCK population. Additionally, $\sim$ 10% of FR Is were found consistent with being the central BCG of a cluster of galaxies, while none of the BL Lac were found compatible. These results contradict what expected by the Unification Model, because if the only difference between both populations was purely their angle respect to our line of sight, there should be no difference among the environments in which they reside. It has been previously suggested that BL Lacs might be associated with FR IIs instead of FR Is, since FR IIs are typically found in regions of low galaxy density. Additionally, this result may be consistent with evolution scenarios such as being in two different stages on the same evolutionary track. This theory has been recently presented by other authors to explain the differences shown in the clustering environments of obscured and unobscured AGN populations, where obscured AGNs tend to reside in denser environments than unobscured AGNs. Analogously, FR I and BL Lacs may represent two different phases of an evolutionary path. BL Lacs exhibiting a typical elliptical galaxy spectrum and with a low Ca H&K break contrast (BL Lacs of galactic type) were studied separately, finding $\sim$ 26% of them lying in high density environments, a fraction significantly higher than BL Lacs. In addition, from the 7 BL Lacs found in galaxy rich large-scale environments, 6 of them were HBLs (peak of the synchrotron emission is in the soft X-rays) while only one of them was a LBL (peak of the synchrotron component is typically at IR/optical wavelengths), supporting the theory that less powerful HBLs reside in denser environments than LBLs, and their mediums are more efficient in decelerating their jet power.

Future studies could point towards an improvement in BL Lac redshift measurements, and to the discovery of new BL Lacs for stronger statistics. Upcoming optical multi-slit spectroscopy on fields of BL Lacs are a good approach to study the environments of BL Lacs and verify the conclusions here presented. Furthermore, it is important to point out that this analysis is only based on optical information, and dedicated X-ray observations are necessary for a more complete understanding of

the clustering environment.

Additionally I presented the results for the last three years of an optical spectroscopic campaign, aiming to increase the number of known BL Lacs. The discovery of new BL Lacs is crucial not only to enlarge the statistical sample used in the clustering analysis; but also to resolve the γ-ray sky, one of the biggest challenges in high energy astrophysics today, and also to build the luminosity function of BL Lacs and to obtain stringent limits on the dark matter annihilation in sub-halos. Since BL Lacs represent about 1/3 of the high energy extragalactic emitters detected with *Fermi*, the strategy was designed to discover these objects in the γ-ray sky. Given the large position uncertainty of *Fermi* sources (of the order of 0.1°) compared to the density of potential optical counterparts, there is no simple procedure to assign them a potential counterpart and a multifrequency approach is thus necessary. BL Lac-like sources were selected based on their peculiar IR colors, similar to those of the *Fermi* BL Lacs (reported in the WIBRALs catalog) and lying within the γ-ray positional uncertainty region of the UGSs. In addition, optical spectra of BCUs, i.e., sources with multifrequency behaviour similar to blazars, were observed because confirmation of their BL Lac nature comes from optical spectroscopy. Using spectroscopic data taken with 6 different telescopes and new spectra recently released in optical surveys (SDSS and 6dFGS) and in the literature, 167 new spectra were obtained and 21 sources already classified as BL Lacs but without a known value for their redshift were reobserved, to see if due to the intrinsic variability of these sources it was possible to observe any lines that permitted a redshift calculation. A number of 121 new BL Lacs were discovered and redshift was obtained for 25 of them, while the rest of the sources were BL Lacs of galactic type (15), FSRQs (21) and QSOs (10) contaminants to the selection method. From the reobserved sources, 4 were found to be FSRQs and 2 were BZGs, the redshift was determined for all these 6 sources and for an additional BL Lac. The optical campaign is still ongoing, having 10 more nights scheduled in both telescopes SOAR and Blanco, that under optimal conditions could lead to the observation of ~ 90 new spectra.

Appendices

Appendix 1

Relativistic beaming

Starting with the Lorentz transformations for special relativity, a "stationary" observer in the laboratory frame F defines events with coordinates t, x, y, z. The comoving frame F' moves with velocity v relative to F, and an observer in this "moving" frame F' defines events using the coordinates t', x', y', z'.

$$\begin{aligned} t' &= \gamma\left(t - \frac{\beta x}{c}\right) \\ x' &= \gamma(x - vt) \\ y' &= y \\ z' &= z \end{aligned} \tag{1}$$

These are the Lorentz transformations, where v is the relative velocity between frames in the x-direction, c is the speed of light, γ the Lorentz factor and β the ration between the velocity and the speed of light:

$$\begin{aligned} \gamma &= \frac{1}{\sqrt{1-\beta^2}} \\ \beta &= \frac{v}{c} \end{aligned} \tag{2}$$

Now let's consider an emitting source in A moving with an angle θ with respect to the line of sight towards B.

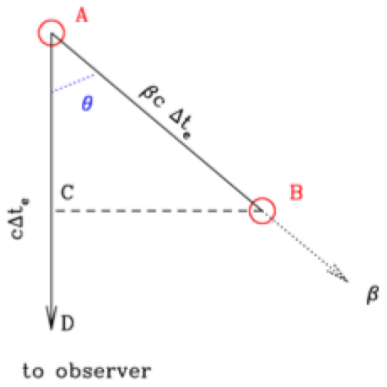

Figure 6: The source moves from A to B, but the apparent move to the observer located in D is from C to B.

The object moves from A to B, but from the observer's perspective it looks like it is moving from C to B. I want to find the relation between Δt_e, the emission time from A to D in the laboratory frame, and Δt_A, the arrival time from C to D in the laboratory frame:

$$\begin{aligned} \overline{CD} &= c\Delta t_A, \ \overline{AD} = c\Delta t_e \\ \overline{CD} &= c\Delta t_e - c\beta\Delta t_e cos\theta \end{aligned} \tag{3}$$

Combining these equations:

$$\Delta t_A = \Delta t_e \left(1 - \beta cos\theta\right) \tag{4}$$

Applying Lorentz transformations to get the relation with the comoving frame:

$$\Delta t_A = \Delta t'_e \gamma \left(1 - \beta cos\theta\right) \tag{5}$$

So the relation between velocities of the source in the laboratory frame and the comoving frame is:

$$v = \frac{v'}{\gamma \left(1 - \beta cos\theta\right)} = \delta v' \tag{6}$$

Being δ the Relativistic Doppler factor of a moving source:

$$\delta = \frac{1}{\gamma \left(1 - \beta cos\theta\right)} \tag{7}$$

The relativistic Doppler factor strongly depends on the angle to the line of sight, for instance:

$$\begin{cases} \theta = 0\,\mathrm{deg} & \rightarrow \delta \simeq 2\gamma \\ \theta = \frac{1}{\gamma} & \rightarrow \delta \simeq \gamma \\ \theta = 90\,\mathrm{deg} & \rightarrow \delta = \frac{1}{\gamma} \end{cases} \tag{8}$$

In Fig. 7 it is shown the Doppler factor vs the angle to the line of sight for different values of the Lorentz factor γ.

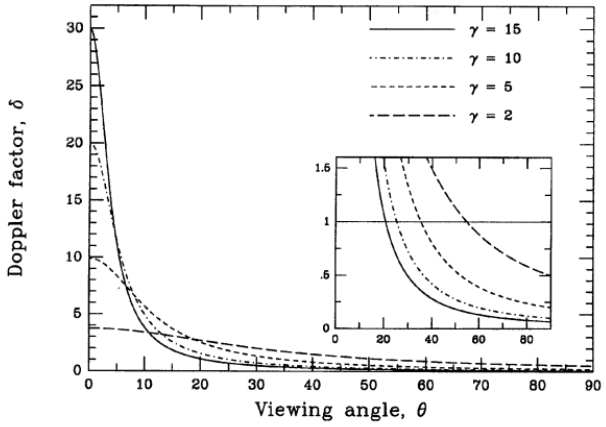

Figure 7: The dependence of the Doppler factor on the angle to the line of sight. Different curves correspond to different Lorentz factors: from the top down γ= 15, 10, 5, 2. The expanded scale on the inset shows the angles for which $\delta < 1$ (Urry & Padovani, 1995).

Superluminal motions

Back to Fig. 6, the apparent velocity for an observer in the laboratory frame is the time the emitting source takes in moving from C to B:

$$v_{ap} = \frac{\overline{CB}}{\Delta t_A} \tag{9}$$

Using trigonometry:

$$sen\theta = \frac{\overline{CB}}{\beta_{source} \Delta t_e} \tag{10}$$

Combining this two equations it is obtained the relation between the apparent speed and the source speed of the source:

$$\beta_{ap} = \frac{\beta_{source} sen\theta}{1 - \beta_{source} cos\theta} \tag{11}$$

The apparent speed can also be expressed in terms of γ and δ:

$$\beta_{ap} = \sqrt{2\gamma\delta - \delta^2 - 1} \tag{12}$$

See Fig. 8 to see the values for θ for which the apparent speed is superluminal.

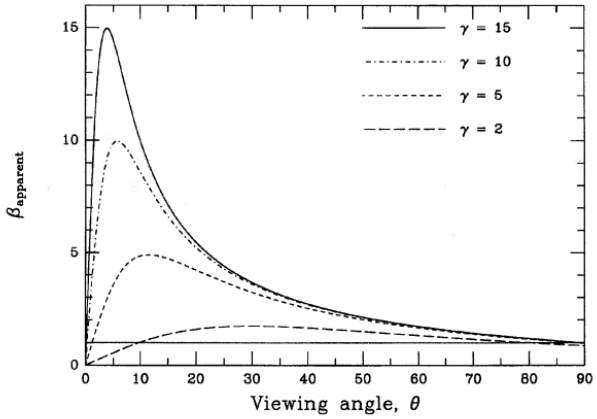

Figure 8: The apparent velocity relative to the speed of light vs angle to the line of sight for an emitter approaching at relativistic speed. Different curves correspond to different Lorentz factors: from the top down,γ=15, 10, 5, 2. The dotted line corresponds to β_{ap}=1. Note that β_{ap} is essentially independent of γ at large angles (Urry & Padovani, 1995).

Differentiating with respect to θ it is possible to obtain the critical angle θ_c for which is maximum the value of the apparent speed:

$$\frac{\partial\beta_{ap}}{\partial\theta} = \frac{(1 - \beta_{source} cos\theta)(\beta_{source} cos\theta) - (\beta_{source} sen\theta)(\beta_{source} sen\theta)}{(1 - \beta_{source} cos\theta)^2} = 0 \rightarrow$$
$$\beta_{source} cos\theta(1 - \beta_{source} cos\theta) = \beta^2_{source} sen\theta^2 \rightarrow cos\theta_c = \beta_{source} \rightarrow \theta_c = cos^{-1}\beta_{source} \tag{13}$$

This value is now introduce in eq. 11 and using trigonometry, $sen(cos^{-1}\beta) = (1 - \beta^2)^{1/2}$:

$$\beta_{ap,max} = \gamma\beta_{source} = \delta\beta_{source} \tag{14}$$

In Fig. 9 are shown the values of the apparent velocities of the jets fo a sample of blazars, showing superluminal values.

Doppler beaming

Considering an emitting spherical source of radius R, its radiation field can be described by the specific intensity:

$$I_\nu = \frac{dE}{dAdtd\nu d\Omega} \tag{15}$$

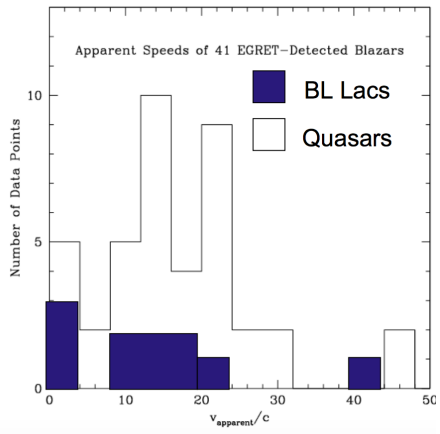

Figure 9: Jet velocities determined in 41 blazars by Jorstad et al. (2001, 2005), Kellermann et al. (2004), Piner et al. (2006), Gabuzda & Cawthorne (1996) and MOJAVE website.

Which is the energy radiated dE per unit of area dA, time interval dt, unit of frequency $d\nu$ and unit of solid angle $d\Omega$. The energy is related to the photon frequency: $E = h\nu$, and the total intensity is obtained by integrating the specific intensity over ν:

$$I = \int I_\nu d\nu \tag{16}$$

The integral of the specific intensity over the solid angle along the line of sight is the specific flux:

$$F_\nu = \int_0^{4\pi} I_\nu cos\theta d\Omega \rightarrow F_\nu = \frac{dE}{dAdtd\nu} \tag{17}$$

Analogously, integrating over the frequency the total flux:

$$F = \int F_\nu d\nu \tag{18}$$

The aberration of light shows how the direction of light propagation changes in the two frames F and F':

$$\begin{aligned} sin\theta &= \frac{sin\theta'}{\gamma(1+\beta cos\theta')} \\ cos\theta &= \frac{cos\theta' + \beta}{(1+\beta cos\theta')} \end{aligned} \tag{19}$$

This leads to a transformation of both the infinitesimal solid angle and the infinitesimal area:

$$d\Omega = \frac{d\Omega'}{\delta^2} \qquad dA = \frac{dA'}{\delta^2} \tag{20}$$

The specific flux is related to the number of photons:

$$F_\nu = \frac{dE}{dtd\nu dA} = h\nu \frac{dN_{ph}}{dtd\nu dA} \tag{21}$$

And the number of photons is a relativistic invariant:

$$dN_{ph} = \frac{1}{h\nu} F_\nu dtd\nu dA = \frac{1}{\delta^3 h\nu} F'_{nu} dt' d\nu' dA' \tag{22}$$

So the beamed specific flux and the specific intensity:

$$F_\nu = \delta^3 F'_\nu \qquad I_\nu = \delta^3 I'_\nu \tag{23}$$

Integrating over the frequency, the total flux and total intensity corrected form the beaming effect:

$$F = \delta^4 F' \qquad I = \delta^4 I' \tag{24}$$

In the observer's frame the total flux and intensity of the source are enhanced by a factor δ^4.

Strong variability

The degree of variability in a source is measured by the change in flux over a given period of time, given by:

$$\frac{\Delta F}{\Delta t} = \delta^5 \frac{\Delta F'}{\Delta t'} \tag{25}$$

From the observer's point of view, the variability of a source is a factor δ^5 stronger than the variability intrinsic to the source.

Appendix 2

Synchrotron emission from one electron

Synchrotron emission is the radiation emitted by an ultrarelativistic electron spinning in a magnetic field. The particle moves in a spiral path around the magnetic field lines with a constant pitch angle θ (see Fig. 10) because of the Lorentz force :

$$F_L = \frac{d}{dt}(\gamma m \overrightarrow{v}) = \frac{e}{c}\overrightarrow{v} \times \overrightarrow{B} \tag{26}$$

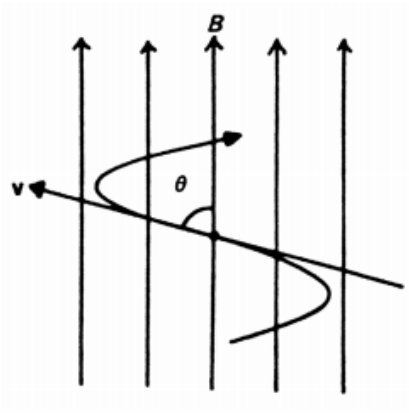

Figure 10: Electron with a velocity v spiralling in a magnetic field B with a pitch angle θ.

The radius r of the circular orbit described by the particle is known as the gyroradius. Because the orbit exhibits perfect circular motion in the $v_\parallel$ frame, the radiation is emitted at a frequency known as the angular cyclotron frequency or angular gyrofrequency and is given by:

$$\omega_g = \frac{v_\perp}{r} = \frac{zeB}{\gamma m_0} \tag{27}$$

The corresponding gyrofrequency ν_g is the number of times per second that the electron rotates around the direction of the magnetic field:

$$\nu_g = \frac{\omega_g}{2\pi} = \frac{zeB}{2\pi\gamma m_0} \tag{28}$$

The total radiation loss rate of the electron in its comoving frame:

$$P' = \frac{E'}{t'} = \frac{2e^2}{3c^3}a'^2 = \frac{2e^2}{3c^3}({a'_\perp}^2 + {a'_\parallel}^2) \tag{29}$$

$a'_\parallel = 0$ because the acceleration is always perpendicular to the velocity vector of the particle and to B. The previous expression is a Lorentz invariant as seen in the Appendix 1:

$$a'_\perp = \gamma^2 a_\perp \tag{30}$$

Substituting:

$$P' = P = \frac{E'}{t'} = \frac{2e^2}{3c^3}\gamma^4 a_\perp^2 \tag{31}$$

The value for the acceleration is given by the Lorentz force, eq. 26:

$$F_L = \frac{d}{dt}(\gamma m \overrightarrow{v}) = \frac{evBsin\theta}{c} \rightarrow a_\perp = \frac{evBsin}{\gamma mc} \tag{32}$$

Substituting this value in eq. 31:

$$P(\theta) = 2\sigma_T c U_B \gamma^2 \beta^2 sin^2\theta \tag{33}$$

Being the density of the magnetic field and the Thompson cross section respectively:

$$\begin{aligned} U_B =& \frac{B^2}{2\mu_0} \\ \sigma_T =& \frac{8\pi r^3}{3} \end{aligned} \tag{34}$$

This result applies for electrons at a specific pith angle θ, for an isotropic distribution of pitch angles $p(\theta) = \frac{1}{2} sin\theta d\theta$:

$$< P >= 2\sigma_T c U_B^2 \gamma^2 \beta^2 \frac{1}{2} \int_0^\pi sin^3\theta d\theta = \frac{4}{3}\sigma_T c U_B \gamma^2 \beta^2 \tag{35}$$

Beaming

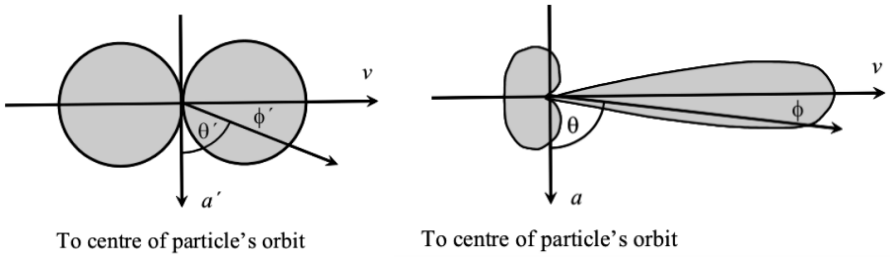

Figure 11: *Left:* angular distribution of the emitted radiation by a moving particle in the non-relativistic approximation ($v << c$). *Right:* angular distribution of the emitted radiation by a relativistic moving particle ($v >> c$). Most of the emitted radiation is beamed into a cone of angle $\sim \frac{1}{\gamma}$ about $\overrightarrow{v}$.

The angular distribution of radiation with respect to the velocity vector in the electron's comoving frame F' is:

$$I'_\nu \propto sin^2\left(\frac{\pi}{2} - \phi'\right) = cos^2\phi' \tag{36}$$

According to the aberration of light formulae given in Appendix 1 (eq. 19):

$$sin\phi = \frac{1}{\gamma}\frac{sin\phi'}{1 + \beta cos\phi'} \tag{37}$$

Consider $\phi \pm \frac{\pi}{4}$, the angles at which the intensity of radiation falls to half its maximum value in the instantaneous rest frame. The corresponding angles ϕ in the laboratory frame are:

$$sin\phi \approx \phi \approx \frac{1}{\gamma} \tag{38}$$

Much of the emitted radiation by a relativistic electron is beamed into a cone of angle $\sim \frac{1}{\gamma}$ about $\overrightarrow{v}$, so a large "spike" of radiation is observed every time the electron's velocity vector lies within an angle of about $\frac{1}{\gamma}$ to the line of sight to the observer. According to Fig. 12, consider the observer located at a distance R from the emitted point A. The radiation from A reaches the observer at s time R/c, and the radiation from B is emitted at a time L/v later, then travels a distance $(R-L)$ at the speed of light to the observer, arriving at a time $L/v + (R-L)/c$.

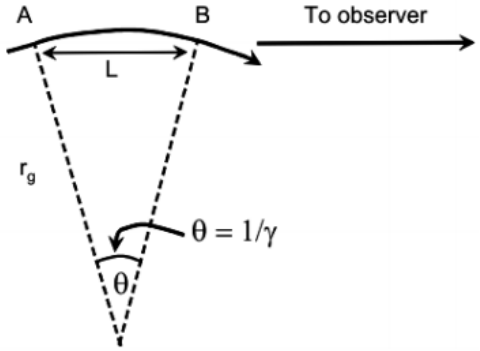

Figure 12: An electron is moving in circular orbit with radius r_g from A to B. The observer is located at a distance R from the emitting point A.

The duration of that "spike" of radiation seen by the observer is:

$$\Delta t = \left(\frac{L}{v} + \frac{R-L}{c}\right) - \frac{R}{c} = \frac{R}{v}(1-\beta) \tag{39}$$

$(1-\beta)$ can be approximated by $\approx \frac{1}{2\gamma^2}$ when $\gamma >> 1$:

$$\frac{L}{v} = \frac{r_g\theta}{v} \approx \frac{1}{\omega_r} = \frac{1}{\omega_g} \tag{40}$$

Being ω_g the non-relativistic angular gyrofrequency and $\omega_r = \frac{\omega_g}{r}$, the observed duration of the pulse is:

$$\Delta t = \frac{1}{2\gamma^2\omega_g} \tag{41}$$

The observed pulse of radiation corresponds to a frequency $\nu \sim \Delta t^{-1}$:

$$\nu = \gamma^2\nu_g = \gamma^3\nu_r = \frac{\gamma^3 v}{2\pi r_g} \tag{42}$$

Being r_g the radius of the circular obit of the particle. This leads to many frequency components necessary to describe the energy distribution shape as shown in Fig. 13.

Emitted spectrum

The emissivity of the single electron is shown in Fig. 14 and it is described by:

$$P(\omega)d\nu = \frac{\sqrt{3}}{mc^2}\frac{e^3 B sin\theta \nu d\nu}{\nu_c}\int_{\nu/\nu_c}^{\infty} K_{5/3}(\eta)d\eta \tag{43}$$

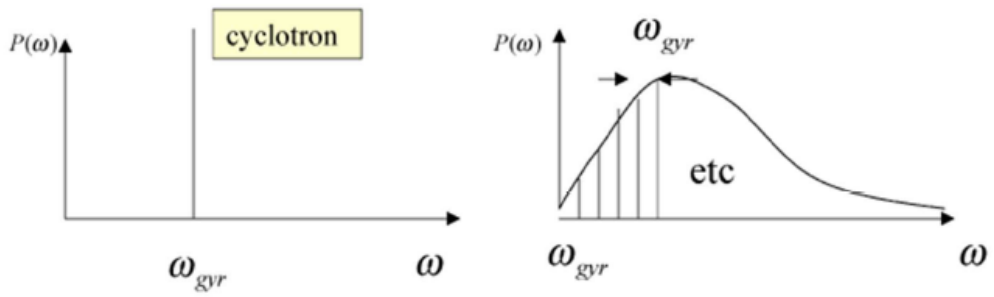

Figure 13: *Left*: the peak of the pulse of radiation seen by the observer. *Right:* energy distribution shape.

Where:

$$\int_{\nu/\nu_c}^{\infty} K_{5/3}(\eta)d\eta \tag{44}$$

is the Bessel function, and the critical frequency:

$$\nu_c = \frac{3}{2}\gamma^2 \nu_g sin\theta \tag{45}$$

Being ν_g given in eq. 28 and θ the pitch angle. The maximum frequency:

$$\nu_{max} = 0.29\nu_c \tag{46}$$

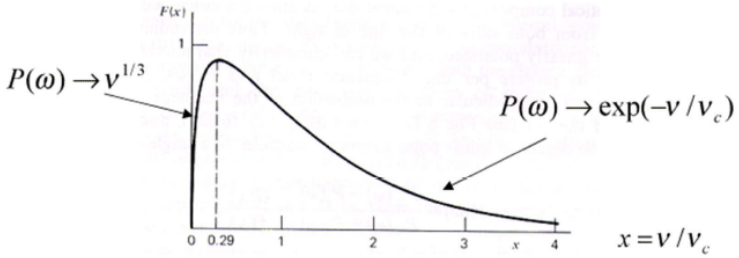

Figure 14: Spectrum emitted by a single electron, peaking on the maximum frequency.

Synchrotron emission from an electron distribution

The emitted energy spectrum of an electron peaks near the critical frequency ν_c as seen in eq. 45, so to a good approximation, it can be assumed that all the energy radiated in the frequency range ν to $\nu + d\nu$ can be attributed to electrons with energies in the range E to $E + dE$ which are assumed to have power law form, see Fig. 15:

$$N(\gamma) = k\gamma^{-p} \tag{47}$$

Therefore the emissivity from many particles:

$$\varepsilon(\nu)d\nu = \frac{1}{4\pi}N(\gamma) < P > d\gamma \tag{48}$$

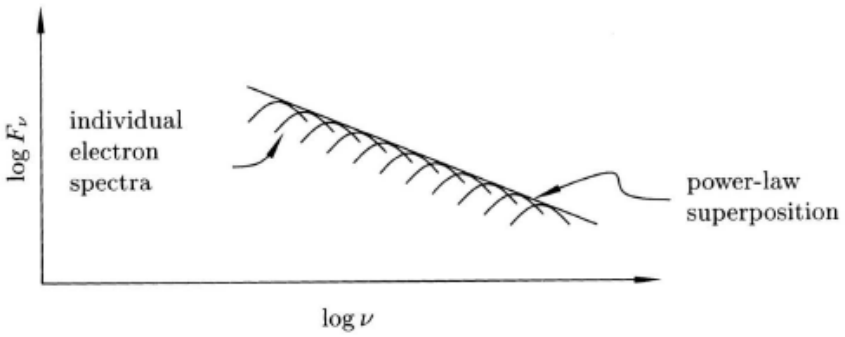

Figure 15: Power law distribution of non-thermal electrons.

$< P >$ was previously derived in eq. 35 and it is the spectral energy distribution of an electron. Substituting:

$$\varepsilon(\nu) = \frac{1}{4\pi} k\omega^{-p} B^2 \gamma^2 \frac{d\gamma}{d\nu} \rightarrow \varepsilon(\nu) = \frac{1}{4\pi} k B^{\frac{1+p}{2}} \nu^{\frac{1-p}{2}} \rightarrow \varepsilon(\nu) = \frac{1}{4\pi} k B^{\alpha+1} \nu^{-\alpha} \tag{49}$$

Being:

$$\alpha = \frac{p+1}{2} \tag{50}$$

The spectrum of an electron power law distribution is a power law.

Synchrotron Self-Absorption

For every emission process there is an associated absorption process. The emitting particles in a source in local thermodynamical equilibrium (LTE) have a Maxwellian energy distribution. Electrons have a characteristic temperature $T \sim E/3k$ and synchrotron self-absorption prevents the brightness temperature from exceeding that T. Synchrotron sources are called non-thermal sources because the energy distribution of the relativistic electrons is a power law. However, self-absorption occurs regardless of the energy distribution.

A bright synchrotron source is optically thick and the brightness temperature at any frequency cannot exceed the effective temperature of those electrons emitting at that frequency. In an ultra-relativistic gas, the relation between energy and temperature is:

$$E = 3kT_e \tag{51}$$

Thus the effective temperature of a relativistic electron:

$$T_e = \frac{E}{3k} = \frac{\gamma m_e c^2}{3k} = \left(\frac{2\pi m_e c \nu}{eB} \right)^{1/2} \frac{m_e c^2}{3k} \tag{52}$$

At a sufficiently low frequency ν, the brightness temperature of any synchrotron source will approach the effective electron temperature T_e at that same frequency, and the source will become opaque. Starting with the definition of brightness temperature:

$$I_\nu = \frac{2kT_b \nu^2}{c^2} \tag{53}$$

$$T_b \approx T_e \rightarrow I_\nu = \frac{2kT_e \nu^2}{c^2} \propto \nu^{1/2} \nu^2 B^{-1/2} \tag{54}$$

The flux density is proportional to I_ν for a source subtending a given solid angle Ω. The spectrum of a synchrotron self-absorbed spatially homogeneous source is for low frequencies a power law spectra of slope 5/2:

$$S(\nu) \propto \nu^{5/2} \tag{55}$$

And for high frequencies, see Fig. 16:

$$S(\nu) \propto \nu^{-\frac{p-1}{2}} \tag{56}$$

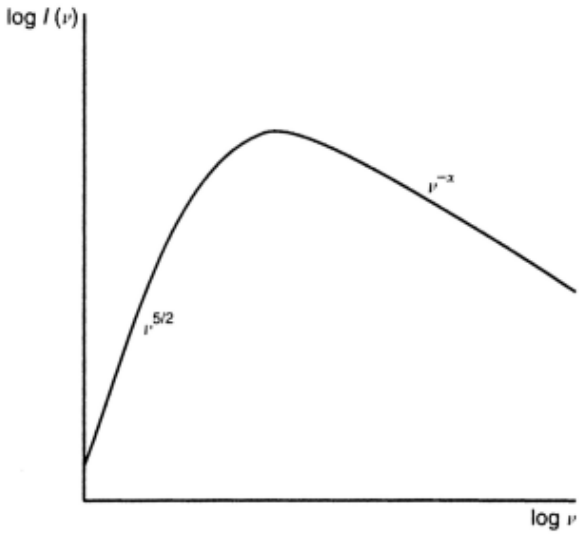

Figure 16: Synchrotron self-absorbed spectra. At high frequencies the spectra is a power law of slope $-\frac{p-1}{2}$ as previously derived, while for low frequencies the spectra is a power law with slope 5/2.

Inverse Compton

Inverse Compton is the scattering of low energy photons to high energies by ultrarelativistic electrons so that the photons gain energy from the electrons. The process is called inverse because the electrons lose energy rather than the photons, the opposite of the standard Compton effect. Here it is considered the energy of the photon much less that $m_e c^2$, and then the Thomson scattering cross-section σ_T given by the eq. 34 can be used to describe the probability of scattering.

To derive the equation describing inverse Compton scattering we begin with the non-relativistic Thompson scattering on the electron's rest frame. The Poynting flux of a plane wave incident on the electron is:

$$\overrightarrow{S} = \frac{c}{4\pi}\overrightarrow{E} \times \overrightarrow{H} = \frac{c}{4\pi}|\overrightarrow{E}|^2 \tag{57}$$

The electron extracts from the incident radiation the amount of power flowing through σ_T and reradiate it over a doughnut shaped pattern. The scattered power is:

$$P = |\overrightarrow{S}|\sigma_T = \sigma_T c U_{rad} \tag{58}$$

Where U_{rad} is the energy density of the incident radiation:

$$U_{rad} = \frac{|\overrightarrow{S}|}{c} = N h\nu \tag{59}$$

Consider an electron moving with speed v in the observer's rest frame. Suppose this electron is hit by two low-energy photons arriving with an angle θ in the observer's frame from the x axis, as represented in Fig. 17.

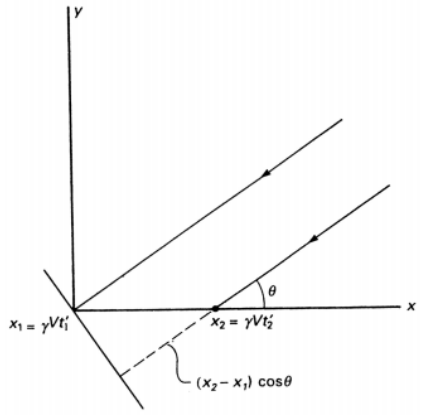

Figure 17: Schematic representation of the Inverse Compton scattering. An electron is moving with speed v in the observer's rest frame and is hit by two low-energy photons arriving with an angle θ in the observer's frame from the x axis.

The coordinates corresponding to the arrival of the 1^{st} and 2^{nd} photons in the observer's frame:

$$(x_1, 0, 0, t_1) \quad (x_2, 0, 0, t_2) \tag{60}$$

Applying the Lorentz transformations (eq. 26):

$$(\gamma v t_1', 0, 0, \gamma t_1') \quad (\gamma v t_2', 0, 0, \gamma t_2') \tag{61}$$

The time Δt elapsed in the observer's frame between the arrival of these two photons:

$$\Delta t = t_2 + \frac{(x_2 - x_1)}{c} cos\theta - t_1 = \gamma t_2' + \frac{(\gamma v t_2' - \gamma v t{-}_1)}{c} cos\theta - \gamma t_1' \rightarrow \Delta t = \Delta t'[\gamma(1 + \beta cos\theta)] \tag{62}$$

The relativistic Doppler equation:

$$\nu' = \nu[\gamma(1 + \beta cos\theta)] \tag{63}$$

In the ultrarelativistic limit $\beta \rightarrow 1$ the maximum frequency of the upscattered radiation in the observer's frame is:

$$\frac{\nu}{\nu_0} \approx 4\gamma^2 \tag{64}$$

The rate at which successive photons arrive is multiplied by the same factor. If N is the photon number density in the observers frame then:

$$N' = N[\gamma(1 + \beta cos\theta)] \tag{65}$$

Thus:

$$U_{rad}' = N' h' \nu' = N h \nu [\gamma(1 + \beta cos\theta)]^2 = U_{rad}[\gamma(1 + \beta cos\theta)]^2 \tag{66}$$

The total energy density in the electron frame of an isotropic radiation field in the observers frame is obtained by integrating over all directions:

$$U_{rad}' = \frac{U_{rad}}{\pi} \int_{\phi=0}^{2\pi} \int_{\theta=0}^{\pi} [\gamma(1 + \beta cos\theta)]^2 sin\theta d\theta d\phi \rightarrow U_{rad}' = U_{rad} \frac{4(\gamma^2 - 1/4)}{3} \tag{67}$$

The total power in the radiation field after inverse Compton:

$$P' = P = \sigma_T c U'_{rad} = \frac{4}{3}\sigma_T c U_{rad}\left(\gamma^2 - \frac{1}{4}\right) \tag{68}$$

Since the initial power of the photons was $\sigma_T c U_{rad}$, the net power added to the radiation field is:

$$P_{IC} = \frac{4}{3}\sigma_T c U_{rad}\left(\gamma^2 - \frac{1}{4}\right) - \sigma_T c U_{rad} \rightarrow P_{IC} = \frac{4}{3}\sigma_T c \beta^2 \gamma^2 U_{rad} \tag{69}$$

This is the net inverse Compton power lost by the electron and gained by the radiation field.

For an isotropic radiation field in the observer's frame, the average energy of scattered photons:

$$< E >= \frac{P_{IC}}{\rho} \tag{70}$$

Being $\rho = \frac{\sigma_T c U_{rad}}{h\nu_0}$ the rate of photon scattering, the number oh photons scattered per second by an electron. Substituting:

$$< E >= \frac{4}{3}\sigma_T c \beta^2 \gamma^2 U_{rad}\left(\frac{h\nu_0}{\sigma_T c U_{rad}}\right) \tag{71}$$

Thus the average frequency of scattered photons:

$$\frac{< \nu >}{\nu_0} = \frac{4}{3}\gamma^2 \tag{72}$$

The IC spectrum is sharply peaked near the average frequency, see Fig. 18.

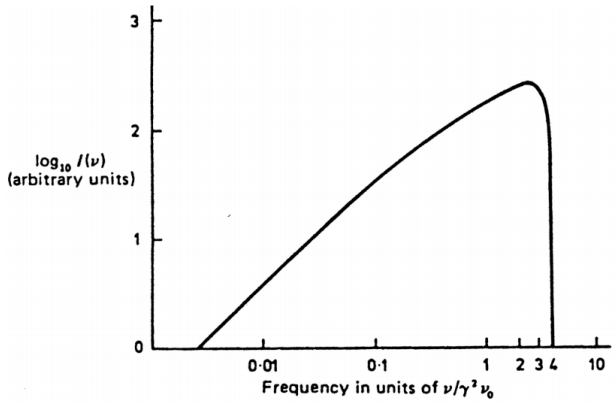

Figure 18: Spectrum of Inverse Compton Radiation.

Synchrotron Self-Compton

It is the result from the IC scattering of the synchrotron radiation emitted by the same population of electrons. Comparing the power of the radiation losses given by synchrotron and by IC:

$$\frac{P_{IC}}{P_{syn}} = \frac{U_{rad}}{U_B} \tag{73}$$

So multiplying the density of relativistic electrons by a factor K multiplies both the synchrotron power and its contribution to U_{rad} by K, synchrotron self-Compton power scales as K^2, see Fig. 19.

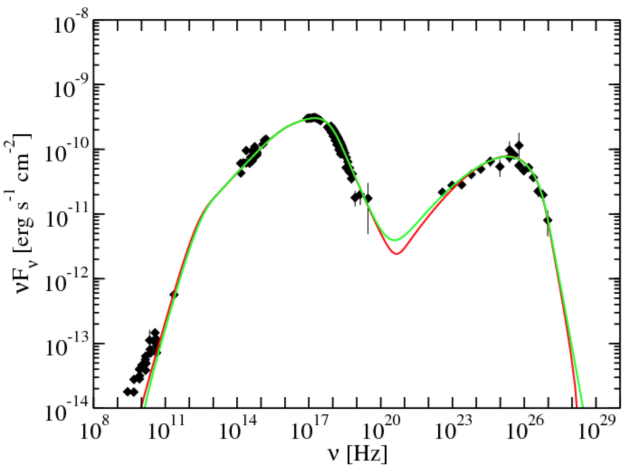

Figure 19: The SED of Mrk 421 measured in multiwavelength campaigns shows two bumps, corresponding to Synchrotron Self-Compton emission (Abdo et al., 2011).

Bibliography

Abdo, A. A., Ackermann, M., Ajello, M., Allafort, A., Antolini, E., Atwood, W. B., Axelsson, M., Baldini, L., Ballet, J., Barbiellini, G., & et al. 2010, ApJS, 188, 405

Abdo, A. A., Ackermann, M., Ajello, M., Baldini, L., Ballet, J., Barbiellini, G., Bastieri, D., Bechtol, K., Bellazzini, R., Berenji, B., & et al. 2011, ApJ, 736, 131

Abell, G. O. 1958, ApJS, 3, 211

Acero, F., Ackermann, M., Ajello, M., Albert, A., Atwood, W. B., Axelsson, M., Baldini, L., Ballet, J., Barbiellini, G., Bastieri, D., Belfiore, A., Bellazzini, R., Bissaldi, E., Blandford, R. D., Bloom, E. D., Bogart, J. R., Bonino, R., Bottacini, E., Bregeon, J., Britto, R. J., Bruel, P., Buehler, R., Burnett, T. H., Buson, S., Caliandro, G. A., Cameron, R. A., Caputo, R., Caragiulo, M., Caraveo, P. A., Casandjian, J. M., Cavazzuti, E., Charles, E., Chaves, R. C. G., Chekhtman, A., Cheung, C. C., Chiang, J., Chiaro, G., Ciprini, S., Claus, R., Cohen-Tanugi, J., Cominsky, L. R., Conrad, J., Cutini, S., D'Ammando, F., de Angelis, A., DeKlotz, M., de Palma, F., Desiante, R., Digel, S. W., Di Venere, L., Drell, P. S., Dubois, R., Dumora, D., Favuzzi, C., Fegan, S. J., Ferrara, E. C., Finke, J., Franckowiak, A., Fukazawa, Y., Funk, S., Fusco, P., Gargano, F., Gasparrini, D., Giebels, B., Giglietto, N., Giommi, P., Giordano, F., Giroletti, M., Glanzman, T., Godfrey, G., Grenier, I. A., Grondin, M.-H., Grove, J. E., Guillemot, L., Guiriec, S., Hadasch, D., Harding, A. K., Hays, E., Hewitt, J. W., Hill, A. B., Horan, D., Iafrate, G., Jogler, T., Jóhannesson, G., Johnson, R. P., Johnson, A. S., Johnson, T. J., Johnson, W. N., Kamae, T., Kataoka, J., Katsuta, J., Kuss, M., La Mura, G., Landriu, D., Larsson, S., Latronico, L., Lemoine-Goumard, M., Li, J., Li, L., Longo, F., Loparco, F., Lott, B., Lovellette, M. N., Lubrano, P., Madejski, G. M., Massaro, F., Mayer, M., Mazziotta, M. N., McEnery, J. E., Michelson, P. F., Mirabal, N., Mizuno, T., Moiseev, A. A., Mongelli, M., Monzani, M. E., Morselli, A., Moskalenko, I. V., Murgia, S., Nuss, E., Ohno, M., Ohsugi, T., Omodei, N., Orienti, M., Orlando, E., Ormes, J. F., Paneque, D., Panetta, J. H., Perkins, J. S., Pesce-Rollins, M., Piron, F., Pivato, G., Porter, T. A., Racusin, J. L., Rando, R., Razzano, M., Razzaque, S., Reimer, A., Reimer, O., Reposeur, T., Rochester, L. S., Romani, R. W., Salvetti, D., Sánchez-Conde, M., Saz Parkinson, P. M., Schulz, A., Siskind, E. J., Smith, D. A., Spada, F., Spandre, G., Spinelli, P., Stephens, T. E., Strong, A. W., Suson, D. J., Takahashi, H., Takahashi, T., Tanaka, Y., Thayer, J. G., Thayer, J. B., Thompson, D. J.,

Tibaldo, L., Tibolla, O., Torres, D. F., Torresi, E., Tosti, G., Troja, E., Van Klaveren, B., Vianello, G., Winer, B. L., Wood, K. S., Wood, M., Zimmer, S., & Fermi-LAT Collaboration. 2015, ApJS, 218, 23

Aharonian, F., Akhperjanian, A. G., Anton, G., Barres de Almeida, U., Bazer-Bachi, A. R., Becherini, Y., Behera, B., Benbow, W., Bernlöhr, K., Boisson, C., Bochow, A., Borrel, V., Brion, E., Brucker, J., Brun, P., Bühler, R., Bulik, T., Büsching, I., Boutelier, T., Chadwick, P. M., Charbonnier, A., Chaves, R. C. G., Cheesebrough, A., Chounet, L.-M., Clapson, A. C., Coignet, G., Costamante, L., Dalton, M., Daniel, M. K., Davids, I. D., Degrange, B., Deil, C., Dickinson, H. J., Djannati-Ataï, A., Domainko, W., O'C. Drury, L., Dubois, F., Dubus, G., Dyks, J., Dyrda, M., Egberts, K., Emmanoulopoulos, D., Espigat, P., Farnier, C., Feinstein, F., Fiasson, A., Förster, A., Fontaine, G., Füßling, M., Gabici, S., Gallant, Y. A., Gérard, L., Giebels, B., Glicenstein, J. F., Glück, B., Goret, P., Göhring, D., Hauser, D., Hauser, M., Heinz, S., Heinzelmann, G., Henri, G., Hermann, G., Hinton, J. A., Hoffmann, A., Hofmann, W., Holleran, M., Hoppe, S., Horns, D., Jacholkowska, A., de Jager, O. C., Jahn, C., Jung, I., Katarzyński, K., Katz, U., Kaufmann, S., Kendziorra, E., Kerschhaggl, M., Khangulyan, D., Khélifi, B., Keogh, D., Kluźniak, W., Kneiske, T., Komin, N., Kosack, K., Lamanna, G., Lenain, J.-P., Lohse, T., Marandon, V., Martin, J. M., Martineau-Huynh, O., Marcowith, A., Maurin, D., McComb, T. J. L., Medina, M. C., Moderski, R., Monard, L. A. G., Moulin, E., Naumann-Godo, M., de Naurois, M., Nedbal, D., Nekrassov, D., Niemiec, J., Nolan, S. J., Ohm, S., Olive, J.-F., de Oña Wilhelmi, E., Orford, K. J., Ostrowski, M., Panter, M., Paz Arribas, M., Pedaletti, G., Pelletier, G., Petrucci, P.-O., Pita, S., Pühlhofer, G., Punch, M., Quirrenbach, A., Raubenheimer, B. C., Raue, M., Rayner, S. M., Renaud, M., Rieger, F., Ripken, J., Rob, L., Rosier-Lees, S., Rowell, G., Rudak, B., Rulten, C. B., Ruppel, J., Sahakian, V., Santangelo, A., Schlickeiser, R., Schöck, F. M., Schröder, R., Schwanke, U., Schwarzburg, S., Schwemmer, S., Shalchi, A., Sikora, M., Skilton, J. L., Sol, H., Spangler, D., Stawarz, Ł., Steenkamp, R., Stegmann, C., Superina, G., Szostek, A., Tam, P. H., Tavernet, J.-P., Terrier, R., Tibolla, O., Tluczykont, M., van Eldik, C., Vasileiadis, G., Venter, C., Venter, L., Vialle, J. P., Vincent, P., Vivier, M., Völk, H. J., Volpe, F., Wagner, S. J., Ward, M., Zdziarski, A. A., & Zech, A. 2009, A&A, 502, 749

Ahn, C. P., Alexandroff, R., Allende Prieto, C., Anderson, S. F., Anderton, T., Andrews, B. H., Aubourg, É., Bailey, S., Balbinot, E., Barnes, R., & et al. 2012, ApJS, 203, 21

Ajello, M., Romani, R. W., Gasparrini, D., Shaw, M. S., Bolmer, J., Cotter, G., Finke, J., Greiner, J., Healey, S. E., King, O., Max-Moerbeck, W., Michelson, P. F., Potter, W. J., Rau, A., Readhead, A. C. S., Richards, J. L., & Schady, P. 2014, ApJ, 780, 73

Alam, S., Albareti, F. D., Allende Prieto, C., Anders, F., Anderson, S. F., Anderton, T., Andrews, B. H., Armengaud, E., Aubourg, É., Bailey, S., & et al. 2015, ApJS, 219, 12

Álvarez Crespo, N., Masetti, N., Ricci, F., Landoni, M., Patiño-Álvarez, V., Massaro, F., D'Abrusco, R., Paggi, A., Chavushyan, V., Jiménez-Bailón, E., Torrealba, J., Latronico, L., La Franca, F., Smith, H. A., & Tosti, G. 2016a, AJ, 151, 32

Álvarez Crespo, N., Massaro, F., D'Abrusco, R., Landoni, M., Masetti, N., Chavushyan, V., Jiménez-Bailón, E., La Franca, F., Milisavljevic, D., Paggi, A., Patiño-Álvarez, V., Ricci, F., & Smith, H. A. 2016b, Ap&SS, 361, 316

Álvarez Crespo, N., Massaro, F., Milisavljevic, D., Landoni, M., Chavushyan, V., Patiño-Álvarez, V., Masetti, N., Jiménez-Bailón, E., Strader, J., Chomiuk, L., Katagiri, H., Kagaya, M., Cheung,

C. C., Paggi, A., D'Abrusco, R., Ricci, F., La Franca, F., Smith, H. A., & Tosti, G. 2016c, AJ, 151, 95

Anderson, L., Aubourg, E., Bailey, S., Bizyaev, D., Blanton, M., Bolton, A. S., Brinkmann, J., Brownstein, J. R., Burden, A., Cuesta, A. J., da Costa, L. A. N., Dawson, K. S., de Putter, R., Eisenstein, D. J., Gunn, J. E., Guo, H., Hamilton, J.-C., Harding, P., Ho, S., Honscheid, K., Kazin, E., Kirkby, D., Kneib, J.-P., Labatie, A., Loomis, C., Lupton, R. H., Malanushenko, E., Malanushenko, V., Mandelbaum, R., Manera, M., Maraston, C., McBride, C. K., Mehta, K. T., Mena, O., Montesano, F., Muna, D., Nichol, R. C., Nuza, S. E., Olmstead, M. D., Oravetz, D., Padmanabhan, N., Palanque-Delabrouille, N., Pan, K., Parejko, J., Pâris, I., Percival, W. J., Petitjean, P., Prada, F., Reid, B., Roe, N. A., Ross, A. J., Ross, N. P., Samushia, L., Sánchez, A. G., Schlegel, D. J., Schneider, D. P., Scóccola, C. G., Seo, H.-J., Sheldon, E. S., Simmons, A., Skibba, R. A., Strauss, M. A., Swanson, M. E. C., Thomas, D., Tinker, J. L., Tojeiro, R., Magaña, M. V., Verde, L., Wagner, C., Wake, D. A., Weaver, B. A., Weinberg, D. H., White, M., Xu, X., Yèche, C., Zehavi, I., & Zhao, G.-B. 2012, MNRAS, 427, 3435

Angel, J. R. P. & Stockman, H. S. 1980, ARA&A, 18, 321

Ankerst, M., Breunig, M. M., peter Kriegel, H., & Sander, J. 1999, in (ACM Press), 49–60

Antonucci, R. R. J. & Ulvestad, J. S. 1985, ApJ, 294, 158

Arbeiter, C., Pohl, M., & Schlickeiser, R. 2002, A&A, 386, 415

Atwood, W. B., Abdo, A. A., Ackermann, M., Althouse, W., Anderson, B., Axelsson, M., Baldini, L., Ballet, J., Band, D. L., Barbiellini, G., & et al. 2009, ApJ, 697, 1071

Baade, W. & Minkowski, R. 1954, ApJ, 119, 206

Bade, N., Beckmann, V., Douglas, N. G., Barthel, P. D., Engels, D., Cordis, L., Nass, P., & Voges, W. 1998, A&A, 334, 459

Bahcall, N. A. in , Formation of Structure in the Universe, ed. A. DekelJ. P. Ostriker, 135

Bahcall, N. A. & Oh, S. P. 1996, ApJ, 462, L49

Baldi, R. D. & Capetti, A. 2008, A&A, 489, 989

Baldi, R. D., Capetti, A., & Giovannini, G. 2015, A&A, 576, A38

Baldi, R. D., Capetti, A., & Massaro, F. 2018, A&A, 609, A1

Begelman, M. C., Rees, M. J., & Blandford, R. D. 1979, Nature, 279, 770

Belsole, E., Worrall, D. M., Hardcastle, M. J., & Croston, J. H. 2007, MNRAS, 381, 1109

Bender, R., Surma, P., Doebereiner, S., Moellenhoff, C., & Madejsky, R. 1989, A&A, 217, 35

Bennett, A. S. 1962, MNRAS, 125, 75

Berlin, A. & Hooper, D. 2014, Phys. Rev. D, 89, 016014

Berlind, A. A., Frieman, J., Weinberg, D. H., Blanton, M. R., Warren, M. S., Abazajian, K., Scranton, R., Hogg, D. W., Scoccimarro, R., Bahcall, N. A., Brinkmann, J., Gott, III, J. R., Kleinman, S. J., Krzesinski, J., Lee, B. C., Miller, C. J., Nitta, A., Schneider, D. P., Tucker, D. L., Zehavi, I., & SDSS Collaboration. 2006, ApJS, 167, 1

Best, P. N. & Heckman, T. M. 2012, MNRAS, 421, 1569

Biretta, J. A., Sparks, W. B., & Macchetto, F. 1999, ApJ, 520, 621

Blandford, R. D. & Rees, M. J. 1978, in BL Lac Objects, ed. A. M. Wolfe, 328–341

Bower, R. G., Lucey, J. R., & Ellis, R. S. 1992, MNRAS, 254, 589

Bregman, J. N., Glassgold, A. E., Huggins, P. J., Kinney, A. L., McHardy, I., Webb, J. R., Pollock, J. T., Leacock, R. J., Smith, A. G., Pica, A. J., Aller, H. D., Aller, M. F., Hodge, P. E., Miller, J. S., Stephens, S. A., Dent, W. A., Balonek, T. J., Barvainis, R., Neugebauer, G., Impey, C. D., Soifer, B. T., Matthews, K., Elias, J. H., & Wisniewski, W. Z. 1988, ApJ, 331, 746

Browne, I. W. A. 1983, MNRAS, 204, 23P

Burg, R., Giacconi, R., Forman, W., & Jones, C. 1994, ApJ, 422, 37

Buttiglione, S., Capetti, A., Celotti, A., Axon, D. J., Chiaberge, M., Macchetto, F. D., & Sparks, W. B. 2009, A&A, 495, 1033

—. 2010, A&A, 509, A6

Byram, E. T., Chubb, T. A., & Friedman, H. 1966, Science, 152, 66

Campana, R., Massaro, E., Gasparrini, D., Cutini, S., & Tramacere, A. 2008, MNRAS, 383, 1166

Capetti, A., Massaro, F., & Baldi, R. D. 2017, A&A, 598, A49

Carangelo, N., Falomo, R., Kotilainen, J., Treves, A., & Ulrich, M.-H. 2003, A&A, 412, 651

Cavaliere, A. G., Gursky, H., & Tucker, W. H. 1971, Nature, 231, 437

Chiaberge, M. in , Multiwavelength AGN Surveys, ed. R. MújicaR. Maiolino, 217–226

Chiaberge, M., Capetti, A., & Celotti, A. 2001, MNRAS, 324, L33

Chiaberge, M., Gilli, R., Capetti, A., & Macchetto, F. D. 2003, ApJ, 597, 166

Ching, J. H. Y., Croom, S. M., Sadler, E. M., Robotham, A. S. G., Brough, S., Baldry, I. K., Bland-Hawthorn, J., Colless, M., Driver, S. P., Holwerda, B. W., Hopkins, A. M., Jarvis, M. J., Johnston, H. M., Kelvin, L. S., Liske, J., Loveday, J., Norberg, P., Pracy, M. B., Steele, O., Thomas, D., & Wang, L. 2017, MNRAS, 469, 4584

Condon, J. J., Cotton, W. D., Greisen, E. W., Yin, Q. F., Perley, R. A., Taylor, G. B., & Broderick, J. J. 1998, AJ, 115, 1693

Cusumano, G., La Parola, V., Segreto, A., Ferrigno, C., Maselli, A., Sbarufatti, B., Romano, P., Chincarini, G., Giommi, P., Masetti, N., Moretti, A., Parisi, P., & Tagliaferri, G. 2010, A&A, 524, A64

D'Abrusco, R., Massaro, F., Paggi, A., Masetti, N., Tosti, G., Giroletti, M., & Smith, H. A. 2013, ApJS, 206, 12

D'Abrusco, R., Massaro, F., Paggi, A., Smith, H. A., Masetti, N., Landoni, M., & Tosti, G. 2014, ApJS, 215, 14

de Vaucouleurs, G. 1971, Publ. Astron. Soc. Pacific, 83, 113

Dermer, C. D. & Schlickeiser, R. 1993, ApJ, 416, 458

Donato, D., Gliozzi, M., Sambruna, R. M., & Pesce, J. E. 2003, A&A, 407, 503

Dvorkin, I. & Rephaeli, Y. 2015, MNRAS, 450, 896

Ebeling, H., Edge, A. C., Fabian, A. C., Allen, S. W., Crawford, C. S., & Böhringer, H. 1997, ApJ, 479, L101

Edge, D. O., Shakeshaft, J. R., McAdam, W. B., Baldwin, J. E., & Archer, S. 1959, Mem. R. Astron. Soc., 68, 37

Eisenhardt, P. R. M., Brodwin, M., Gonzalez, A. H., Stanford, S. A., Stern, D., Barmby, P., Brown, M. J. I., Dawson, K., Dey, A., Doi, M., Galametz, A., Jannuzi, B. T., Kochanek, C. S., Meyers, J., Morokuma, T., & Moustakas, L. A. 2008, ApJ, 684, 905

Eisenstein, D. J., Weinberg, D. H., Agol, E., Aihara, H., Allende Prieto, C., Anderson, S. F., Arns, J. A., Aubourg, É., Bailey, S., Balbinot, E., & et al. 2011, AJ, 142, 72

Eke, V. R., Baugh, C. M., Cole, S., Frenk, C. S., Norberg, P., Peacock, J. A., Baldry, I. K., Bland-Hawthorn, J., Bridges, T., Cannon, R., Colless, M., Collins, C., Couch, W., Dalton, G., de Propris, R., Driver, S. P., Efstathiou, G., Ellis, R. S., Glazebrook, K., Jackson, C., Lahav, O., Lewis, I., Lumsden, S., Maddox, S., Madgwick, D., Peterson, B. A., Sutherland, W., & Taylor, K. 2004, MNRAS, 348, 866

Ester, M., Kriegel, H.-P., Sander, J., & Xu, X. 1996, in (AAAI Press), 226–231

Evans, P. A., Osborne, J. P., Beardmore, A. P., Page, K. L., Willingale, R., Mountford, C. J., Pagani, C., Burrows, D. N., Kennea, J. A., Perri, M., Tagliaferri, G., & Gehrels, N. 2014, ApJS, 210, 8

Faber, S. M., Tremaine, S., Ajhar, E. A., Byun, Y.-I., Dressler, A., Gebhardt, K., Grillmair, C., Kormendy, J., Lauer, T. R., & Richstone, D. 1997, AJ, 114, 1771

Falomo, R., Pesce, J. E., & Treves, A. 1993a, AJ, 105, 2031

—. 1993b, ApJ, 411, L63

—. 1995, ApJ, 438, L9

Falomo, R., Pian, E., & Treves, A. 2014, A&ARv, 22, 73

Fanaroff, B. L. & Riley, J. M. 1974, Monthly Notices of the Royal Astronomical Society, 167, 31P

Farina, E. P., Fumagalli, M., Decarli, R., & Fanidakis, N. 2016, MNRAS, 455, 618

Fossati, G., Maraschi, L., Celotti, A., Comastri, A., & Ghisellini, G. 1998, MNRAS, 299, 433

Fried, J. W., Stickel, M., & Kuehr, H. 1993, A&A, 268, 53

Gabuzda, D. C. & Cawthorne, T. V. 1996, MNRAS, 283, 759

Gendre, M. A., Best, P. N., Wall, J. V., & Ker, L. M. 2013, MNRAS, 430, 3086

Ghisellini, G., Celotti, A., Fossati, G., Maraschi, L., & Comastri, A. 1998, MNRAS, 301, 451

Ghisellini, G. & Maraschi, L. 1989, ApJ, 340, 181

Ghisellini, G., Padovani, P., Celotti, A., & Maraschi, L. 1993, ApJ, 407, 65

Giacconi, R., Murray, S., Gursky, H., Kellogg, E., Schreier, E., & Tananbaum, H. 1972, ApJ, 178, 281

Giles, P. A., Maughan, B. J., Birkinshaw, M., Worrall, D. M., & Lancaster, K. 2012, MNRAS, 419, 503

Giommi, P., Padovani, P., Polenta, G., Turriziani, S., D'Elia, V., & Piranomonte, S. 2012, MNRAS, 420, 2899

Giommi, P., Piranomonte, S., Perri, M., & Padovani, P. 2005, A&A, 434, 385

Giovannini, G., Cotton, W. D., Feretti, L., Lara, L., & Venturi, T. 2001, ApJ, 552, 508

Gladders, M. D., Abraham, R. G., McHardy, I. M., Crawford, C. S., Merrifield, M. R., & Jones, L. R. 1997, MNRAS, 284, 27

Gladders, M. D., López-Cruz, O., Yee, H. K. C., & Kodama, T. 1998, ApJ, 501, 571

Gonzalez-Serrano, J. I., Carballo, R., & Perez-Fournon, I. 1993, AJ, 105, 1710

Gott, III, J. R. & Turner, E. L. 1977, ApJ, 213, 309

Graham, A. W. Elliptical and Disk Galaxy Structure and Modern Scaling Laws, ed. , T. D. OswaltW. C. Keel, 91

Gregory, P. C., Scott, W. K., Douglas, K., & Condon, J. J. 1996, ApJS, 103, 427

Haas, M. R., Schaye, J., & Jeeson-Daniel, A. 2012, MNRAS, 419, 2133

Hahsler, M. & Piekenbrock, M. 2017, dbscan: Density Based Clustering of Applications with Noise (DBSCAN) and Related Algorithms, r package version 1.1-1

Hao, C. N., Mao, S., Deng, Z. G., Xia, X. Y., & Wu, H. 2006, MNRAS, 370, 1339

Hao, J., McKay, T. A., Koester, B. P., Rykoff, E. S., Rozo, E., Annis, J., Wechsler, R. H., Evrard, A., Siegel, S. R., Becker, M., Busha, M., Gerdes, D., Johnston, D. E., & Sheldon, E. 2010, ApJS, 191, 254

Hardcastle, M. J. & Worrall, D. M. 1999, MNRAS, 309, 969

Hardcastle, M. J., Worrall, D. M., & Birkinshaw, M. 1999, MNRAS, 305, 246

Healey, S. E., Romani, R. W., Taylor, G. B., Sadler, E. M., Ricci, R., Murphy, T., Ulvestad, J. S., & Winn, J. N. 2007, ApJS, 171, 61

Hes, R., Barthel, P. D., & Fosbury, R. A. E. 1993, Nature, 362, 326

Hickox, R. C., Jones, C., Forman, W. R., Murray, S. S., Kochanek, C. S., Eisenstein, D., Jannuzi, B. T., Dey, A., Brown, M. J. I., Stern, D., Eisenhardt, P. R., Gorjian, V., Brodwin, M., Narayan, R., Cool, R. J., Kenter, A., Caldwell, N., & Anderson, M. E. 2009, , 696, 891

Hill, G. J. & Lilly, S. J. 1991, The Astrophysical Journal, 367, 1

Hoffmeister, C. 1929, Astronomische Nachrichten, 236, 233

Hopkins, P. F., Hernquist, L., Cox, T. J., & Kereš, D. 2008, , 175, 356

Horne, K. 1986, PASP, 98, 609

Ineson, J., Croston, J. H., Hardcastle, M. J., Kraft, R. P., Evans, D. A., & Jarvis, M. 2015, MNRAS, 453, 2682

Jannuzi, B. T., Smith, P. S., & Elston, R. 1994, ApJ, 428, 130

Jin, S.-W., Gu, Q., Huang, S., Shi, Y., & Feng, L.-L. 2014, ApJ, 787, 63

Jones, D. H., Read, M. A., Saunders, W., Colless, M., Jarrett, T., Parker, Q. A., Fairall, A. P., Mauch, T., Sadler, E. M., Watson, F. G., Burton, D., Campbell, L. A., Cass, P., Croom, S. M., Dawe, J., Fiegert, K., Frankcombe, L., Hartley, M., Huchra, J., James, D., Kirby, E., Lahav, O., Lucey, J., Mamon, G. A., Moore, L., Peterson, B. A., Prior, S., Proust, D., Russell, K., Safouris, V., Wakamatsu, K.-I., Westra, E., & Williams, M. 2009, MNRAS, 399, 683

Jorstad, S. G., Marscher, A. P., Lister, M. L., Stirling, A. M., Cawthorne, T. V., Gear, W. K., Gómez, J. L., Stevens, J. A., Smith, P. S., Forster, J. R., & Robson, E. I. 2005, AJ, 130, 1418

Jorstad, S. G., Marscher, A. P., Mattox, J. R., Wehrle, A. E., Bloom, S. D., & Yurchenko, A. V. 2001, ApJS, 134, 181

Keeler, J. E. 1900, MNRAS, 60, 424

Kellermann, K. I., Lister, M. L., Homan, D. C., Vermeulen, R. C., Cohen, M. H., Ros, E., Kadler, M., Zensus, J. A., & Kovalev, Y. Y. 2004, ApJ, 609, 539

Kellermann, K. I., Sramek, R., Schmidt, M., Shaffer, D. B., & Green, R. 1989, AJ, 98, 1195

Kharb, P., Shastri, P., & Gabuzda, D. C. 2005, ApJ, 632, L69

Krolik, J. H. 2000, Physics Today, 53, 55

Laing, R. A. & Bridle, A. H. in , Astronomical Society of the Pacific Conference Series, Vol. 386, Extragalactic Jets: Theory and Observation from Radio to Gamma Ray, ed. T. A. RectorD. S. De Young, 70

Laing, R. A., Jenkins, C. R., Wall, J. V., & Unger, S. W. Astronomical Society of the Pacific Conference Series, Vol. 54, , The Physics of Active Galaxies, ed. G. V. BicknellM. A. Dopita & P. J. Quinn, 201

Laing, R. A., Parma, P., de Ruiter, H. R., & Fanti, R. 1999, MNRAS, 306, 513

Lauer, T. R., Postman, M., Strauss, M. A., Graves, G. J., & Chisari, N. E. 2014, ApJ, 797, 82

Ledlow, M. J. & Owen, F. N. 1996, AJ, 112, 9

Lejeune Dirichlet, G. 1850, Journal für die reine und angewandte Mathematik, 40, 209

Leon, S., Cortes, P. C., Guerard, M., Villard, E., Hidayat, T., Ocaña Flaquer, B., & Vila-Vilaro, B. 2016, A&A, 586, A70

Lietzen, H., Nilsson, K., Takalo, L. O., Heinämäki, P., Nurmi, P., Keinänen, P., & Wagner, S. 2008, A&A, 482, 771

Lintott, C. J., Schawinski, K., Slosar, A., Land, K., Bamford, S., Thomas, D., Raddick, M. J., Nichol, R. C., Szalay, A., Andreescu, D., Murray, P., & Vandenberg, J. 2008, MNRAS, 389, 1179

Liodakis, I., Marchili, N., Angelakis, E., Fuhrmann, L., Nestoras, I., Myserlis, I., Karamanavis, V., Krichbaum, T. P., Sievers, A., Ungerechts, H., & Zensus, J. A. 2017, MNRAS, 466, 4625

Lister, M. L. & Homan, D. C. 2005, AJ, 130, 1389

Longair, M. S. & Seldner, M. 1979, MNRAS, 189, 433

Mantz, A. B., Abdulla, Z., Carlstrom, J. E., Greer, C. H., Leitch, E. M., Marrone, D. P., Muchovej, S., Adami, C., Birkinshaw, M., Bremer, M., Clerc, N., Giles, P., Horellou, C., Maughan, B., Pacaud, F., Pierre, M., & Willis, J. 2014, ApJ, 794, 157

Maselli, A., Massaro, E., Nesci, R., Sclavi, S., Rossi, C., & Giommi, P. 2010, A&A, 512, A74

Massaro, E., Giommi, P., Leto, C., Marchegiani, P., Maselli, A., Perri, M., Piranomonte, S., & Sclavi, S. 2009, A&A, 495, 691

Massaro, E., Maselli, A., Leto, C., Marchegiani, P., Perri, M., Giommi, P., & Piranomonte, S. 2015a, Ap&SS, 357, 75

Massaro, E., Nesci, R., & Piranomonte, S. 2012, MNRAS, 422, 2322

Massaro, F., D'Abrusco, R., Ajello, M., Grindlay, J. E., & Smith, H. A. 2011, ApJ, 740, L48

Massaro, F., Thompson, D. J., & Ferrara, E. C. 2015b, A&ARv, 24, 2

Mauch, T., Murphy, T., Buttery, H. J., Curran, J., Hunstead, R. W., Piestrzynski, B., Robertson, J. G., & Sadler, E. M. 2003, MNRAS, 342, 1117

Maughan, B. J., Giles, P. A., Randall, S. W., Jones, C., & Forman, W. R. 2012, MNRAS, 421, 1583

McCarthy, P. J., Kapahi, V. K., van Breugel, W., Persson, S. E., Athreya, R., & Subrahmanya, C. R. 1996, ApJS, 107, 19

McLure, R. J. & Dunlop, J. S. 2001, MNRAS, 321, 515

Messier, C. 1781, Catalogue des Nébuleuses et des Amas d'Étoiles (Catalog of Nebulae and Star Clusters), Tech. rep.

Miller, H. R., Carini, M. T., & Goodrich, B. D. 1989, Nature, 337, 627

Miller, N. A., Ledlow, M. J., Owen, F. N., & Hill, J. M. 2002, AJ, 123, 3018

Minkowski, R. 1960, ApJ, 132, 908

Muriel, H. 2016, A&A, 591, L4

Muriel, H., Donzelli, C., Rovero, A. C., & Pichel, A. 2015, A&A, 574, A101

Nolan, P. L., Abdo, A. A., Ackermann, M., Ajello, M., Allafort, A., Antolini, E., Atwood, W. B., Axelsson, M., Baldini, L., Ballet, J., & et al. 2012, ApJS, 199, 31

O'Dea, C. P. & Owen, F. N. 1986, ApJ, 301, 841

Oke, J. B. & Gunn, J. E. 1974, ApJ, 189, L5

Olguín-Iglesias, A., León-Tavares, J., Kotilainen, J. K., Chavushyan, V., Tornikoski, M., Valtaoja, E., Añorve, C., Valdés, J., & Carrasco, L. 2016, in Active Galactic Nuclei: What's in a Name?, 44

Owen, F. N. & Ledlow, M. J. Astronomical Society of the Pacific Conference Series, Vol. 54, , The Physics of Active Galaxies, ed. G. V. BicknellM. A. Dopita & P. J. Quinn, 319

Owen, F. N., Ledlow, M. J., & Keel, W. C. 1996, AJ, 111, 53

Padmanabhan, N., Schlegel, D. J., Finkbeiner, D. P., Barentine, J. C., Blanton, M. R., Brewington, H. J., Gunn, J. E., Harvanek, M., Hogg, D. W., Ivezić, Ž., Johnston, D., Kent, S. M., Kleinman, S. J., Knapp, G. R., Krzesinski, J., Long, D., Neilsen, Jr., E. H., Nitta, A., Loomis, C., Lupton, R. H., Roweis, S., Snedden, S. A., Strauss, M. A., & Tucker, D. L. 2008, ApJ, 674, 1217

Padovani, P. & Giommi, P. 1995, ApJ, 444, 567

Padovani, P. & Urry, C. M. 1992, ApJ, 387, 449

Paiano, S., Landoni, M., Falomo, R., Treves, A., & Scarpa, R. 2017, ApJ, 844, 120

Peña-Herazo, H. A., Marchesini, E. J., Álvarez Crespo, N., Ricci, F., Massaro, F., Chavushyan, V., Landoni, M., Strader, J., Chomiuk, L., Cheung, C. C., Masetti, N., Jiménez-Bailón, E., D'Abrusco, R., Paggi, A., Milisavljevic, D., La Franca, F., Smith, H. A., & Tosti, G. 2017, Ap&SS, 362, 228

Perlman, E. S. & Stocke, J. T. 1993, ApJ, 406, 430

Pesce, J. E., Falomo, R., & Treves, A. 1994, AJ, 107, 494

—. 1995, AJ, 110, 1554

Pesce, J. E., Urry, C. M., O'Dowd, M., Scarpa, R., Falomo, R., & Treves, A. 2002, New Astronomy Reviews, 46, 159

Petrov, L., Mahony, E. K., Edwards, P. G., Sadler, E. M., Schinzel, F. K., & McConnell, D. 2013, MNRAS, 432, 1294

Pierre, M., Adami, C., Birkinshaw, M., Chiappetti, L., Ettori, S., Evrard, A., Faccioli, L., Gastaldello, F., Giles, P., Horellou, C., Iovino, A., Koulouridis, E., Lidman, C., Le Brun, A., Maughan, B., Maurogordato, S., McCarthy, I., Miyazaki, S., Pacaud, F., Paltani, S., Plionis, M., Reiprich, T., Sadibekova, T., Smolcic, V., Snowden, S., Surdej, J., Tsirou, M., Vignali, C., Willis, J., Alis, S., Altieri, B., Baran, N., Benoist, C., Bongiorno, A., Bremer, M., Butler, A., Cappi, A., Caretta, C., Ciliegi, P., Clerc, N., Corasaniti, P. S., Coupon, J., Delhaize, J., Delvecchio, I., Democles, J., Desai, S., Devriendt, J., Dubois, Y., Eckert, D., Elyiv, A., Farahi, A., Ferraril, C., Fotopoulou, S., Forman, W., Georgantopoulos, I., Guglielmo, V., Huynh, M., Jerlin, N., Jones, C., Lavoie, S., Le Fevre, J.-P., Lieu, M., Kilbinger, M., MaruIli, F., Mantz, A., McGee, S., Melin, J.-B., Melnyk, O., Moscardini, L., Novak, M., Piconcelli, E., Poggianti, B., Pomarede, D., Pompei, E., Ponman, T., Ramos Ceja, M. E., Rana, P., Rapetti, D., Raychaudhury, S., Ricci, M., Rottgering, H., Sahlen, M., Sauvageot, J.-L., Schimd, C., Sereno, M., Smith, G. P., Umetsu, K.,

Valageas, P., Valotti, A., Valtchanov, I., Veropalumbo, A., Ascaso, B., Barnes, D., De Petris, M., Durret, F., Donahue, M., Ithana, M., Jarvis, M., Johnston-Hollitt, M., Kalfountzou, E., Kay, S., La Franca, F., Okabe, N., Muzzin, A., Rettura, A., Ricci, F., Ridl, J., Risaliti, G., Takizawa, M., Thomas, P., & Truong, N. 2017, Astronomische Nachrichten, 338, 334

Piner, B. G., Bhattarai, D., Edwards, P. G., & Jones, D. L. Blazar Variability Workshop II: Entering the GLAST Era, ed. , H. R. MillerK. MarshallJ. R. Webb & M. F. Aller, 163

Planck Collaboration, Ade, P. A. R., Aghanim, N., Argüeso, F., Armitage-Caplan, C., Arnaud, M., Ashdown, M., Atrio-Barandela, F., Aumont, J., Baccigalupi, C., & et al. 2014, A&A, 571, A28

Planck Collaboration, Ade, P. A. R., Aghanim, N., Arnaud, M., Ashdown, M., Aumont, J., Baccigalupi, C., Banday, A. J., Barreiro, R. B., Barrena, R., & et al. 2016, A&A, 594, A27

Postman, M. & Geller, M. J. 1984, ApJ, 281, 95

Press, W. H. & Davis, M. 1982, ApJ, 259, 449

Prestage, R. M. & Peacock, J. A. 1988, MNRAS, 230, 131

—. 1989, MNRAS, 236, 959

Quillen, A. C., Bower, G. A., & Stritzinger, M. 2000, ApJS, 128, 85

Ramos Almeida, C., Bessiere, P. S., Tadhunter, C. N., Inskip, K. J., Morganti, R., Dicken, D., González-Serrano, J. I., & Holt, J. 2013, MNRAS, 436, 997

Roettgering, H. J. A., Miley, G. K., Chambers, K. C., & Macchetto, F. 1995, A&AS, 114, 51

Romanishin, W. 1992, ApJ, 401, L65

Rosse, F. E. o. & Parsons, L. 1880, Scientific Transactions of the Royal Dublin Society, Volume 2, p. 1 (Dublin: Royal Dublin Society 1880), 2, 1

Rovero, A. C., Muriel, H., Donzelli, C., & Pichel, A. 2016, A&A, 589, A92

Sabater, J., Best, P. N., & Argudo-Fernández, M. 2013, MNRAS, 430, 638

Sander, J., Qin, X., Lu, Z., Niu, N., & Kovarsky, A. K.-Y. Whang, J. JeonK. Shim & J. Srivastava (Berlin, Heidelberg: Springer Berlin Heidelberg), 75–87

Scarpa, R., Urry, C. M., Falomo, R., Pesce, J. E., & Treves, A. 2000, ApJ, 532, 740

Schinzel, F. K., Petrov, L., Taylor, G. B., Mahony, E. K., Edwards, P. G., & Kovalev, Y. Y. 2015, ApJS, 217, 4

Schlegel, D. J., Finkbeiner, D. P., & Davis, M. 1998, ApJ, 500, 525

Schmitt, J. L. 1968, Nature, 218, 663

Scoville, N. A. J. Baker, J. GlennA. I. HarrisJ. G. Mangum & M. S. Yun, 166

Shaw, M. S., Romani, R. W., Cotter, G., Healey, S. E., Michelson, P. F., Readhead, A. C. S., Richards, J. L., Max-Moerbeck, W., King, O. G., & Potter, W. J. 2013, ApJ, 764, 135

Sikora, M., Begelman, M. C., & Rees, M. J. 1994, ApJ, 421, 153

Smith, E. P., O'Dea, C. P., & Baum, S. A. 1995, ApJ, 441, 113

Spinrad, H. 1976, PASP, 88, 565

Spinrad, H., Westphal, J., Kristian, J., & Sandage, A. 1977, ApJ, 216, L87

Stickel, M., Fried, J. W., & Kuehr, H. 1993, A&AS, 98, 393

Stickel, M., Padovani, P., Urry, C. M., Fried, J. W., & Kuehr, H. 1991, ApJ, 374, 431

Stott, J. P., Pimbblet, K. A., Edge, A. C., Smith, G. P., & Wardlow, J. L. 2009, MNRAS, 394, 2098

Strauss, M. A., Weinberg, D. H., Lupton, R. H., Narayanan, V. K., Annis, J., Bernardi, M., Blanton, M., Burles, S., Connolly, A. J., Dalcanton, J., Doi, M., Eisenstein, D., Frieman, J. A., Fukugita, M., Gunn, J. E., Ivezić, Ž., Kent, S., Kim, R. S. J., Knapp, G. R., Kron, R. G., Munn, J. A., Newberg, H. J., Nichol, R. C., Okamura, S., Quinn, T. R., Richmond, M. W., Schlegel, D. J., Shimasaku, K., SubbaRao, M., Szalay, A. S., Vanden Berk, D., Vogeley, M. S., Yanny, B., Yasuda, N., York, D. G., & Zehavi, I. 2002, AJ, 124, 1810

Strittmatter, P. A., Serkowski, K., Carswell, R., Stein, W. A., Merrill, K. M., & Burbidge, E. M. 1972, ApJ, 175, L7

Tago, E., Einasto, J., Saar, E., Einasto, M., Suhhonenko, I., Jõeveer, M., Vennik, J., Heinämäki, P., & Tucker, D. L. 2006, Astronomische Nachrichten, 327, 365

Tempel, E., Tago, E., & Liivamägi, L. J. 2012, A&A, 540, A106

Titov, O., Jauncey, D. L., Johnston, H. M., Hunstead, R. W., & Christensen, L. 2011, AJ, 142, 165

Tremblay, G. R., Chiaberge, M., Donzelli, C. J., Quillen, A. C., Capetti, A., Sparks, W. B., & Macchetto, F. D. 2007, ApJ, 666, 109

Turner, E. L. & Gott, III, J. R. 1976, ApJS, 32, 409

Turner, R. 2016, deldir: Delaunay Triangulation and Dirichlet (Voronoi) Tessellation, r package version 0.1-12

Ulrich, M. H. Lecture Notes in Physics, Berlin Springer Verlag, Vol. 334, , BL Lac Objects, ed. L. MaraschiT. Maccacaro & M.-H. Ulrich, 45

Urry, C. M. & Padovani, P. 1995, PASP, 107, 803

Urry, C. M., Padovani, P., & Stickel, M. 1991, ApJ, 382, 501

Vermeulen, R. C. & Taylor, G. B. 1995, AJ, 109, 1983

Véron-Cetty, M.-P. & Véron, P. 2006, A&A, 455, 773

Voges, W., Aschenbach, B., Boller, T., Bräuninger, H., Briel, U., Burkert, W., Dennerl, K., Englhauser, J., Gruber, R., Haberl, F., Hartner, G., Hasinger, G., Kürster, M., Pfeffermann, E., Pietsch, W., Predehl, P., Rosso, C., Schmitt, J. H. M. M., Trümper, J., & Zimmermann, H. U. 1999, A&A, 349, 389

Voronoi. 1908, Journal für die reine und angewandte Mathematik, 134, 198

White, R. L., Becker, R. H., Gregg, M. D., Laurent-Muehleisen, S. A., Brotherton, M. S., Impey, C. D., Petry, C. E., Foltz, C. B., Chaffee, F. H., Richards, G. T., Oegerle, W. R., Helfand, D. J., McMahon, R. G., & Cabanela, J. E. 2000, ApJS, 126, 133

White, R. L., Becker, R. H., Helfand, D. J., & Gregg, M. D. 1997, ApJ, 475, 479

Willott, C. J., Rawlings, S., Blundell, K. M., Lacy, M., & Eales, S. A. 2001, MNRAS, 322, 536

Wright, A. E., Griffith, M. R., Burke, B. F., & Ekers, R. D. 1994, ApJS, 91, 111

Wright, E. L., Eisenhardt, P. R. M., Mainzer, A. K., Ressler, M. E., Cutri, R. M., Jarrett, T., Kirkpatrick, J. D., Padgett, D., McMillan, R. S., Skrutskie, M., Stanford, S. A., Cohen, M., Walker, R. G., Mather, J. C., Leisawitz, D., Gautier, III, T. N., McLean, I., Benford, D., Lonsdale, C. J., Blain, A., Mendez, B., Irace, W. R., Duval, V., Liu, F., Royer, D., Heinrichsen, I., Howard, J., Shannon, M., Kendall, M., Walsh, A. L., Larsen, M., Cardon, J. G., Schick, S., Schwalm, M., Abid, M., Fabinsky, B., Naes, L., & Tsai, C.-W. 2010, AJ, 140, 1868

Wurtz, R., Ellingson, E., Stocke, J. T., & Yee, H. K. C. 1993, AJ, 106, 869

Wurtz, R., Stocke, J. T., Ellingson, E., & Yee, H. K. C. 1997, ApJ, 480, 547

York, D. G., Adelman, J., Anderson, Jr., J. E., Anderson, S. F., Annis, J., Bahcall, N. A., Bakken, J. A., Barkhouser, R., Bastian, S., Berman, E., Boroski, W. N., Bracker, S., Briegel, C., Briggs, J. W., Brinkmann, J., Brunner, R., Burles, S., Carey, L., Carr, M. A., Castander, F. J., Chen, B., Colestock, P. L., Connolly, A. J., Crocker, J. H., Csabai, I., Czarapata, P. C., Davis, J. E., Doi, M., Dombeck, T., Eisenstein, D., Ellman, N., Elms, B. R., Evans, M. L., Fan, X., Federwitz, G. R., Fiscelli, L., Friedman, S., Frieman, J. A., Fukugita, M., Gillespie, B., Gunn, J. E., Gurbani, V. K., de Haas, E., Haldeman, M., Harris, F. H., Hayes, J., Heckman, T. M., Hennessy, G. S., Hindsley, R. B., Holm, S., Holmgren, D. J., Huang, C.-h., Hull, C., Husby, D., Ichikawa, S.-I., Ichikawa, T., Ivezić, Ž., Kent, S., Kim, R. S. J., Kinney, E., Klaene, M., Kleinman, A. N., Kleinman, S., Knapp, G. R., Korienek, J., Kron, R. G., Kunszt, P. Z., Lamb, D. Q., Lee, B., Leger, R. F., Limmongkol, S., Lindenmeyer, C., Long, D. C., Loomis, C., Loveday, J., Lucinio, R., Lupton, R. H., MacKinnon, B., Mannery, E. J., Mantsch, P. M., Margon, B., McGehee, P., McKay, T. A., Meiksin, A., Merelli, A., Monet, D. G., Munn, J. A., Narayanan, V. K., Nash, T., Neilsen, E., Neswold, R., Newberg, H. J., Nichol, R. C., Nicinski, T., Nonino, M., Okada, N., Okamura, S., Ostriker, J. P., Owen, R., Pauls, A. G., Peoples, J., Peterson, R. L., Petravick, D., Pier, J. R., Pope, A., Pordes, R., Prosapio, A., Rechenmacher, R., Quinn, T. R., Richards, G. T., Richmond, M. W., Rivetta, C. H., Rockosi, C. M., Ruthmansdorfer, K., Sandford, D., Schlegel, D. J., Schneider, D. P., Sekiguchi, M., Sergey, G., Shimasaku, K., Siegmund, W. A., Smee, S., Smith, J. A., Snedden, S., Stone, R., Stoughton, C., Strauss, M. A., Stubbs, C., SubbaRao, M., Szalay, A. S., Szapudi, I., Szokoly, G. P., Thakar, A. R., Tremonti, C., Tucker, D. L., Uomoto, A., Vanden Berk, D., Vogeley, M. S., Waddell, P., Wang, S.-i., Watanabe, M., Weinberg, D. H., Yanny, B., Yasuda, N., & SDSS Collaboration. 2000, AJ, 120, 1579

Zirbel, E. L. 1996, The Astrophysical Journal, 473, 713

Zirbel, E. L. 1997, ApJ, 476, 489

Zwicky, F. 1933, Helvetica Physica Acta, 6, 110